

# Addressing Thermodynamic Inefficiencies of Hydrogen Storage in Transition Metal Hydrides

Thesis by  
Nicholas J. Weadock

In Partial Fulfillment of the Requirements for the  
Degree of  
Doctor of Philosophy

The logo for the California Institute of Technology (Caltech), featuring the word "Caltech" in a bold, orange, sans-serif font.

CALIFORNIA INSTITUTE OF TECHNOLOGY  
Pasadena, California

2019  
Defended January 22, 2019

© 2019

Nicholas J. Weadock  
ORCID: 0000-0002-1178-7641

All rights reserved

## ACKNOWLEDGEMENTS

“...meddle first, understand later. You had to meddle a *bit* before you had anything to try to understand.”

Sir Terry Pratchett, *Interesting Times*

First and foremost I would like to thank my advisor, Professor Brent Fultz, for giving me the opportunity to explore the topics and experiments I found interesting. His guidance and expertise helped me to think critically and develop my fundamental understanding of materials science. My goal in coming to Caltech was to do just that, so I am eternally grateful to Professor Fultz for helping me achieve this.

I must thank Michelle Shearer and Sheryl Ehrman for challenging me early on to be a better and more clever scientist. Ichiro Takeuchi and Raymond Phaneuf, your teaching and mentoring are what drove me to desire to understand the fundamentals of materials science. Lourdes Salamanca-Riba and Liangbing Hu, thank you for giving me the opportunity to discover my passion for experimental work.

I have learned a great amount from current and former members of the Fultz group. Ratnakumar Bugga, Heng Yang, and Hongjin Tan taught me all they know about metal hydrides and electrochemistry, and from Maxwell Murialdo and Nicholas Stadie I learned about gas adsorption and absorption. Hillary Smith taught me about neutron scattering but also provided sound advice on my research in general. Channing Ahn gave great advice on experimental design and always had an amusing anecdote to share. Thank you also to Lisa, Dennis, Fred, Jane, Yang, Peter, Cullen, Bryce, Claire, Camille, Stefan, and Olle for your support. Aadith, thank you for all your assistance in the lab.

Finally I must thank my friends and family for keeping me sane. The Steuben house was a great four years, and the friendships started there will last for many more years to come. Jon, thank you for always being up for a skiing or biking trip. Dee Dee, thank you for being a wonderful and supportive partner. I will always appreciate you showing me around LA and having a real interest in learning about my research. Mom, Dad, and Zack, I can never thank you enough for your support over the years.

## ABSTRACT

Transition metal hydrides (MH) are an attractive class of materials for several energy technologies. Primary benefits include their large volumetric storage capacity (often exceeding that of liquid hydrogen) and capability to absorb and desorb hydrogen for hundreds of cycles. In this thesis, we set out to understand two of the thermodynamic inefficiencies of MH: the pressure hysteresis associated with hydrogen absorption and desorption and the corrosion and dissolution of high capacity MH alloys in high pH electrolyte environments.

The volume change associated with hydriding transitions can exceed 10%, and a macroscopic nucleation barrier resulting from coherency strains has been proposed as the origin of the pressure hysteresis. We investigated this hypothesis for the palladium-hydrogen system. The hysteresis and phase transformation characteristics of bulk and nanocrystalline PdH were characterized with coupled *in situ* X-ray diffraction and pressure composition isotherm measurements. Size effects are observed in the total hydrogen uptake and hydrogen solubility in the hydride phases. Experimentally determined hysteresis energies were found to be comparable to the misfit strain between the Pd and PdH phases and much larger than the energy for dislocation formation. Theoretical predictions of pressure hysteresis overestimate the experimentally measured hysteresis, and we suggest methods of accommodation which could explain the discrepancy. Finally, we propose that an effect of the nucleation barrier is to split the coherent spinodal phase diagram and introduce directionally dependent phase boundaries.

We report a successful development of  $\text{Ti}_{29}\text{V}_{62-x}\text{Ni}_9\text{Cr}_x$  ( $x = 0, 6, 12$ ) body-centered cubic (BCC) MH electrodes for MH batteries by addressing vanadium corrosion and dissolution in potassium hydroxide electrolytes. The effectiveness of a limited oxygen environment and vanadate ion addition against corrosion are compared to the effects of Cr substitution. By identifying oxygen as the primary source of corrosion and eliminating oxygen with an Ar-purged cell, the Cr-free alloy electrode achieved a maximum capacity of 594 mAh/g, double the capacity of commercial  $\text{AB}_5$  MH electrodes. With modified coin cells suppressing oxygen evolution, the cycle stability of the  $\text{Ti}_{29}\text{V}_{62}\text{Ni}_9$  alloy electrode was greatly improved with either vanadate ion additions to the electrolyte or Cr-substitution in the alloy. Both approaches lead to reversible capacity of 500 mAh/g for 200 cycles.

## PUBLISHED CONTENT AND CONTRIBUTIONS

- N. J. Weadock, and B. Fultz. Elastic energy and the hysteresis of phase transformations in palladium hydride. *In Preparation*.  
N.J.W. conceived of the project, performed the experiments, analyzed the data, and wrote the manuscript.
- H. L. Smith, N. J. Weadock, F. C. Yang, N. Butch, T. J. Udovic, C. W. Li, and B. Fultz. Hydrogen Dynamics in Laves-phase hydride  $\text{YFe}_2\text{H}_{2.6}$  under pressure. *In Preparation*.  
N.J.W. assisted with sample preparation, beamtime experiments, and data analysis.
- M. Murialdo, N. J. Weadock, Y. Liu, C. Ahn, S. Baker, K. Landskron, B. Fultz. High-pressure hydrogen adsorption on porous electron-rich covalent organonitridic frameworks. *ACS Omega*, 4:444-448, December 2018. doi : [10.1021/acsomega.8b03206](https://doi.org/10.1021/acsomega.8b03206)  
N.J.W. performed surface area and skeletal density measurements, and participated in data analysis and preparation of the manuscript.
- H. Yang<sup>†</sup>, N. J. Weadock<sup>†</sup>, H. Tan, and B. Fultz. High capacity V-based metal hydride electrodes for rechargeable batteries. *Journal of Materials Chemistry A*, 5:21785-21794, September 2017. doi : [10.1039/C7TA07396H](https://doi.org/10.1039/C7TA07396H).  
N.J.W. participated in the conception of the project, performed characterization and electrochemical experiments, prepared and analyzed the data, and co-authored the manuscript.  
<sup>†</sup>These authors contributed equally to the manuscript.

## PATENT APPLICATIONS

H. Yang, N. J. Weadock, B. Fultz, B. Edwards. High capacity corrosion resistant V-based metal hydride electrodes for rechargeable metal hydride batteries. U.S. Application No. 15/996,390. Filed June 2018. *Application Pending*.

N. J. Weadock, H. Tan, B. Fultz, H. Yang. Metal hydride alloys with improved rate performance. U.S. Application No. 15/046,104. Filed February 2016. *Application Pending*.

## TABLE OF CONTENTS

|  |     |
|--|-----|
| Acknowledgements . . . . .   | iii |
| Abstract . . . . .   | iv  |
| Published Content and Contributions . . . . .  | v   |
| Patent Applications . . . . .  | vi  |
| Table of Contents . . . . .  | vii |
| List of Illustrations . . . . .  | ix  |
| List of Tables . . . . .   | xv  |
| Chapter I: Introduction . . . . .  | 1   |
| 1.1 Metal Hydrides as Energy Materials . . . . .   | 1   |
| 1.2 Chemisorption of Hydrogen by Metal Hydrides . . . . .  | 2   |
| 1.3 Hysteresis in Metal Hydrides . . . . .   | 6   |
| 1.4 Nickel-Metal Hydride Batteries . . . . .   | 17  |
| Chapter II: Elastic Energy and the Hysteresis of Phase Transformations in<br>Palladium Hydride . . . . .                                 | 19  |
| 2.1 Chapter Overview . . . . .   | 19  |
| 2.2 Experimental Details . . . . .   | 19  |
| 2.3 Results . . . . .  | 20  |
| 2.4 Discussion . . . . .   | 29  |
| 2.5 Conclusions . . . . .  | 38  |
| Chapter III: High Capacity V-based Metal Hydride Electrodes for Recharge-<br>able Batteries . . . . .                                    | 39  |
| 3.1 Chapter Overview . . . . .   | 39  |
| 3.2 Corrosion of Vanadium in Aqueous Environments . . . . .  | 39  |
| 3.3 Experimental Methods . . . . .   | 41  |
| 3.4 Results . . . . .  | 43  |
| 3.5 Discussion . . . . .   | 55  |
| 3.6 Conclusions . . . . .  | 60  |
| Chapter IV: Summary and future work . . . . .  | 61  |
| 4.1 Principles of Metal Hydride Hysteresis . . . . .   | 61  |
| 4.2 New Models for Hysteresis . . . . .  | 62  |
| 4.3 Metal Hydride Electrodes . . . . .   | 63  |
| 4.4 Outlook . . . . .  | 64  |
| Appendix A: Supplementary Information for Elastic Energy and the Hystere-<br>sis of Phase Transformations in Palladium Hydride . . . . . | 65  |
| A.1 Pressure composition isotherm measurements in Sievert's apparatus<br>and <i>in situ</i> hydrogen environment chamber . . . . .       | 66  |
| A.2 Two-Dimensional finite Eshelby model for an eccentric circular in-<br>clusion in a circular domain . . . . .                         | 66  |

|  |    |
|--|----|
| Appendix B: Supplementary Information for High capacity V-based metal<br>hydride electrodes for rechargeable batteries . . . . . | 72 |
| B.1 Alloy and Electrode Characterization . . . . .   | 72 |
| B.2 Energy density calculations of a MH-Air battery cell . . . . .   | 78 |
| Appendix C: Shoulder Removal from X-ray Diffraction Data . . . . .   | 84 |
| C.1 Inel CPS120 Detector . . . . .   | 84 |
| C.2 Anomalous Peak Shoulders . . . . .   | 85 |
| C.3 Shoulder Removal with Deconvolution . . . . .  | 86 |
| Bibliography . . . . .   | 97 |

## LIST OF ILLUSTRATIONS

| <i>Number</i>   | <i>Page</i> |
|---|-------------|
| 1.1 Schematic illustrating two methods of hydriding a hydride-forming metal. On the left, hydriding the metal (gray particles) occurs by electrochemical reduction of water in an aqueous electrolyte. The right side illustrates hydriding from the gas phase; a high partial pressure of hydrogen gas is used to drive the hydriding transition. . . . .  | 3           |
| 1.2 Composite PCT for the V-H system as published by Yukawa, et al. and Reilly and Wiswall. Yukawa investigated the monohydride transition electrochemically, whereas Reilly and Wiswall characterized the dihydride transition in the gas-phase. . . . .   | 7           |
| 1.3 Experimentally determined temperature-composition phase diagram for the V-H system. Black circles represent data points, and the connecting lines serve as approximate phase boundaries. The $\beta/(\beta + \gamma)$ phase boundary is an average value due to the finite width of the vertical component of the PCTs in Figure 1.2. . . . .   | 8           |
| 1.4 Full pressure-composition isotherm for 200 mesh Pd powder measured at 333 K. The Pd powder had been cycled two times prior to this PCT measurement. A hysteresis of 0.88 was calculated using Equation 1.5. Dashed lines illustrate the graphical construction method used to determine phase boundaries in the sloping regions of the plateau. . . . .   | 10          |
| 1.5 Comparison of pressure hysteresis values reported in the literature for bulk Pd. . . . .  | 11          |
| 2.1 High-resolution TEM image of as-received nanocrystalline Pd powder prior to hydrogen exposure. . . . .  | 21          |
| 2.2 Inverted dark field TEM micrograph of the nanocrystalline Pd with inverted electron diffraction pattern (330 mm camera length) inset. The dark field image was acquired with a 10 $\mu\text{m}$ objective aperture capturing 111 diffracted beams. A 40 $\mu\text{m}$ selected area aperture was used when acquiring the electron diffraction pattern. Scale bar for the electron diffraction pattern is 2 $\text{nm}^{-1}$ . . . . . | 22          |

|     |  |    |
|-----|--|----|
| 2.3 | a) Pressure-composition isotherms for bulk and nanocrystalline PdH. An additional isotherm of the bulk PdH was measured at 435 K. The inset plots the plateau region on a linear pressure scale to highlight the shape of the isotherm curves. Closed symbols denote absorption, and open symbols correspond to the subsequent desorption. b) 333 K minor loop for bulk PdH measured <i>in situ</i> . After hydriding to approximately 80% transformed, the isotherm was reversed and the sample was dehydrided. . . . .                         | 24 |
| 2.4 | <i>In situ</i> X-ray diffraction patterns of hydrogen absorption (left) and desorption (right) by bulk Pd powder. The color of each trace corresponds to the total hydrogen concentration (in H/M) as indicated by the central legend. . . . .   | 25 |
| 2.5 | <i>In situ</i> X-ray diffraction patterns of hydrogen absorption (left) and desorption (right) by nanocrystalline Pd powder. The color of each trace corresponds to the total hydrogen concentration (in H/M) as indicated by the central legend. . . . .  | 26 |
| 2.6 | Refined $\alpha$ phase fraction for the a) bulk and b) nanocrystalline PdH powders. The black arrows indicate the direction of transformation, and shading of the traces indicates the error bars. . . . .   | 28 |
| 2.7 | a) Refined lattice parameters of the a) bulk and b) nanocrystalline Pd powders during hydrogen absorption and desorption. The red and blue traces correspond to the solid solution $\alpha$ phase and hydride $\beta$ phase, respectively. Error bars are indicated by the shaded region. . . . .  | 30 |
| 2.8 | Variation of dimensionless strain energy with inclusion position. An $0.4R$ inclusion is subjected to a uniform isotropic eigenstrain field $\epsilon_{ij}^* = \frac{1}{2}\epsilon^*\delta_{ij}$ . Strain energy density is normalized by $(4\mu\epsilon^{*2})/(\kappa + 1)^2$ . Inset are heat maps of strain energy density for particles with inclusions located at the origin (left) and displaced $0.6R$ (right). The matrix boundary is constrained by traction-free conditions; displacements due to the inclusion are not shown. . . . . | 34 |

|     |   |    |
|-----|---|----|
| 2.9 | Absorption and desorption spinodal phase diagrams determined from terminal compositions of bulk and nanocrystalline PdH. Bulk and nanocrystalline PdH data from this study are plotted as circles and triangles, respectively. Additional bulk data from Wicke et al. are plotted as upside down triangles. 6 and 4 nm nanoparticle PdH data from Vogel et al. are plotted as squares and diamonds, respectively. Filled markers denote absorption, open markers denote desorption. The black line denotes a hypothetical equilibrium boundary for a barrier-free transformation. . . . . | 36 |
| 3.1 | Pourbaix diagram of V with the potential of the Hg/HgO reference electrode indicated by the short-dash blue line. The orange box outlines the operational pH and potential ranges for MH batteries, and the green lines indicate how equilibrium shifts with varying concentrations of dissolved V (in units of grams V per kilogram H <sub>2</sub> O). Line a: $2\text{H}^+ + 2\text{e}^- \rightarrow \text{H}_2$ ; and line b: $2\text{H}_2\text{O} \rightarrow \text{O}_2 + 4\text{H}^+ + 4\text{e}^-$   | 40 |
| 3.2 | X-ray diffractograms of Ti <sub>29</sub> V <sub>62-x</sub> Ni <sub>9</sub> Cr <sub>x</sub> ( $x = 0, 6, \text{ and } 12$ ) alloys after hydrogen activation and pulverization of the arc melted ingots. .   | 44 |
| 3.3 | Backscattered electron images at (a) low and (b) high magnification of a polished Ti <sub>29</sub> V <sub>50</sub> Ni <sub>9</sub> Cr <sub>12</sub> ingot. . . . .  | 45 |
| 3.4 | Hydrogen absorption isotherms of Ti <sub>29</sub> V <sub>62-x</sub> Ni <sub>9</sub> Cr <sub>x</sub> ( $x = 0, 6, \text{ and } 12$ ) alloys as measured on a Sievert's apparatus at room temperature (298 K). . . . .  | 47 |
| 3.5 | Characterization of the three alloy electrodes: (a) First cycle charge/discharge curves for the alloy electrodes in a beaker cell. <i>Ex situ</i> experiments were performed at the numbered points on the graph. (b) Diffractograms of the three alloy electrodes at corresponding states of charge. Hydride phases are marked with squares (BCC), triangles (BCT), and circles (FCC). . . . .   | 48 |
| 3.6 | The charge/discharge curves for (a) Ti <sub>29</sub> V <sub>62</sub> Ni <sub>9</sub> and (b) Ti <sub>29</sub> V <sub>50</sub> Ni <sub>9</sub> Cr <sub>12</sub> electrodes in an Ar-purged three-electrode cell. . . . .   | 52 |

|     |   |    |
|-----|---|----|
| 3.7 | Cycling performance of coin cells containing (a) $\text{Ti}_{29}\text{V}_{62}\text{Ni}_9$ electrodes with $\text{KVO}_3$ additions to the KOH electrolyte and (b), (c) $\text{Ti}_{29}\text{V}_{62-x}\text{Ni}_9\text{Cr}_x$ electrodes with KOH electrolyte. The MH electrodes were charged to 550 mAh/g in (a) and (b), and charged to 400 mAh/g in (c). In (a), cycling was interrupted after 110 cycles and restarted after two weeks for the cell containing KOH with 500 mM $\text{KVO}_3$ . In (b) and (c), cycling was interrupted for two weeks after the 100th cycle for the $\text{Ti}_{29}\text{V}_{56}\text{Ni}_9\text{Cr}_6$ and $\text{Ti}_{29}\text{V}_{50}\text{Ni}_9\text{Cr}_{12}$ electrodes. . . . . | 54 |
| 3.8 | Schematics illustrating the (a) operational and (b) local oxidation that occurs for V in the $\text{Ti}_{29}\text{V}_{62}\text{Ni}_9$ alloy electrodes. . . . .   | 57 |
| 3.9 | Gravimetric and volumetric energy density analysis of a MH air cell as a function of the specific capacity and thickness of the MH electrode. The shaded areas indicate the published energy density ranges for 18650 type Li-ion batteries. . . . .  | 59 |
| A.1 | Scanning electron micrograph of a bulk Pd particle consisting of coalesced grains. The inset shows the scale of individual particles. . . . .   | 65 |
| A.2 | Comparison of pressure composition isotherms measured in a Sievert's apparatus and <i>in situ</i> hydrogen environment chamber. Isotherms for bulk Pd are plotted in a) and for nanocrystalline Pd in b), both at 333K. . . . .   | 67 |
| A.3 | Displacement field $u_1$ for the case published by Zou. Displacement is normalized by $(1 - \nu)/r\epsilon^*$ to be unitless. . . . .   | 69 |
| A.4 | Displacement fields $u_1$ for $0.4r$ inclusions located a) at the center and b) displaced to the edge of the domain. Displacement is normalized by $(4r\epsilon^*)/(\kappa + 1)$ to be unitless. . . . .  | 69 |
| A.5 | Displacement fields $u_2$ for $0.4r$ inclusions located a) at the center and b) displaced to the edge of the domain. Displacement is normalized by $(4r\epsilon^*)/(\kappa + 1)$ to be unitless. . . . .  | 70 |
| A.6 | Stress fields $\sigma_{11}$ for $0.4r$ inclusions located a) at the center and b) displaced to the edge of the domain. Stresses are normalized by $(4\mu\epsilon^*)/(\kappa + 1)^2$ to be unitless. . . . .   | 70 |
| A.7 | Stress fields $\sigma_{12}$ for $0.4r$ inclusions located a) at the center and b) displaced to the edge of the domain. Stresses are normalized by $(4\mu\epsilon^*)/(\kappa + 1)^2$ to be unitless. . . . .   | 71 |

|     |   |    |
|-----|---|----|
| A.8 | Stress fields $\sigma_{22}$ for $0.4r$ inclusions located a) at the center and b) displaced to the edge of the domain. Stresses are normalized by $(4\mu\epsilon^*)/(\kappa + 1)^2$ to be unitless. . . . .   | 71 |
| B.1 | Lattice parameters of dehydrated $\text{Ti}_{29}\text{V}_{62-x}\text{Ni}_9\text{Cr}_x$ ( $x = 0, 6, \text{ and } 12$ ) alloys. . . . .  | 72 |
| B.2 | Backscattered electron images of (a) $\text{Ti}_{29}\text{V}_{62}\text{Ni}_9$ and (b) $\text{Ti}_{29}\text{V}_{56}\text{Ni}_9\text{Cr}_6$ alloy ingots. Compositions superimposed on the image indicate average compositions of the V-rich (dark) and Ni-rich (light) regions as determined by EDS. . . . .   | 74 |
| B.3 | Discharge curve of $\text{Ti}_{29}\text{V}_{62}\text{Ni}_9$ electrode in various KOH electrolytes. Plateaus associated with V and Ni oxidation are indicated with arrows. . . . .   | 75 |
| B.4 | XPS spectra of V, Cr, Ni, and Ti prior to charge [1] and after full discharge [4] of $\text{Ti}_{29}\text{V}_{62-x}\text{Ni}_9\text{Cr}_x$ ( $x = 0, 6, \text{ and } 12$ ) alloy electrodes. Boxed numbers correspond to the state of charge indicated in 3.5a. . . . .   | 76 |
| B.5 | Cycle performance of $\text{Ti}_{29}\text{V}_{62-x}\text{Ni}_9\text{Cr}_x$ ( $x = 0, 6, \text{ and } 12$ ) alloy electrodes in various electrolytes. All tests were performed in air-saturated beaker cells. Cells were charged to 800 mAh/g, then discharged following the three-step discharge procedure up to $-0.75\text{V}$ vs. Hg/HgO. . . . .  | 77 |
| B.6 | Operation potential for the $\text{Ni}(\text{OH})_2/\text{NiO}(\text{OH})$ electrode used in coin cells. Current density is based on the mass loading of the $\text{Ni}(\text{OH})_2$ electrode powder mixture. Closed and open symbols correspond to the plateau potentials for charge and discharge, respectively. The boxed region indicates the current density range associated with the MH electrode (10 to 100 mA/g for a $3 \text{ mg/cm}^2$ loading). . . . .  | 78 |
| B.7 | Charge/discharge curves of a). $\text{Ti}_{29}\text{V}_{62}\text{Ni}_9$ and b). $\text{Ti}_{29}\text{V}_{50}\text{Ni}_9\text{Cr}_{12}$ electrodes in the coin cell configuration. The cells were charged for 550 mAh/g and three-step discharged at 100, 40, and 20 mA/g to 1.10V. The decrease of discharge capacity at the high current step shows that the rate capability of the MH electrode decreases with cycling, despite excellent capacity retention. . . . . | 79 |
| B.8 | Top view (left) and 3D side view (right) drawings of the 100-Wh MH-air cell. Dimensions not to scale. . . . .   | 82 |
| B.9 | Plot of electrode potential versus current density for the air electrode manufactured by Electric Fuel.[120] . . . . .  | 83 |

|      |   |    |
|------|---|----|
| C.1  | Raw diffraction data from the NIST Standard Reference Material 640b (powdered Si) collected with the Inel CPS 120 Detector. Tick marks indicate expected peak positions from Mo $K\alpha_1$ (red) and $K\alpha_2$ x-ray wavelengths. . . . .  | 86 |
| C.2  | Diffraction pattern of the NIST SRM 640b (Si) obtained on the Inel CPS 120 detector with output lines switched. The anomalous shoulder peaks are still observed to the right of the main peak, as indicated by the black arrows. . . . .  | 87 |
| C.3  | Comparison of peak shape of signal obtained through Pb slits to Bragg reflection of a Si standard. The Si Bragg peak is approximately twice as wide as the signal passed through the Pb slits. . . . .  | 90 |
| C.4  | Primary and shoulder peak separation (in channel numbers) as a function of channel number of the primary peak. Both peaks are fit with a separate Lorentzian function. . . . .  | 91 |
| C.5  | Relative magnitude of the shoulder peak as a function of channel number. . . . .  | 91 |
| C.6  | Half-width at half maximum of the shoulder peaks as a function of channel number. . . . .   | 92 |
| C.7  | Plot illustrating the instrument function determination. The dotted line is raw data obtained from the Pb slit/ $\text{GeO}_2$ setup, the dashed line is a Lorentzian fit to the main peak, and the solid line plots the result of convolving the instrument function with the Lorentzian peak. Examples of the instrument function are provided in Figure C.8. | 93 |
| C.8  | Two (solid and dashed lines) of 18 instrument functions describing shoulder behavior of the Inel CPS120 detector. The functions consist of a delta function at 4096 and a small peak resulting in a shoulder in the raw diffraction data. . . . .   | 94 |
| C.9  | Raw (dotted red line) and deconvoluted (solid blue line) bulk Pd diffraction patterns acquired with the CPS 120 detector. Primary peak shapes are well preserved. . . . .   | 95 |
| C.10 | Raw (dotted red line) and deconvoluted (solid blue line) nanocrystalline Pd diffraction patterns acquired with the CPS 120 detector. Primary peak shapes are well preserved. . . . .  | 96 |

## LIST OF TABLES

| <i>Number</i>   | <i>Page</i> |
|---|-------------|
| 2.1 Terminal compositions of the hydriding transition for bulk and nanocrystalline PdH obtained from <i>in situ</i> XRD results at 333 K. High temperature (435 K) compositions for the bulk Pd are evaluated from the pressure composition isotherm. . . . .   | 27          |
| 2.2 Variation of lattice parameter with hydrogen concentration $da/dc$ ( $\text{\AA}/\text{H}$ ) in single phase regions. All data are fitted with a linear function according to Vegard's Law. Empty entries correspond to regions with insufficient data points to fit. . . . .   | 29          |
| 2.3 Comparison of experimentally determined hysteresis values to those predicted by S-K theory. S-K hysteresis values are calculated according to Equation 1.8 with values listed in this section. Experimental hysteresis values for the 300 nm nanoparticles are determined from refs. [24] and [25]. . . . .   | 32          |
| 2.4 Summary of hysteresis energies and measured and estimated misfit strain values for bulk and nanocrystalline PdH at 333 K. Misfit strains are estimated from hysteresis energies according to Equation 2.2. . . . .  | 33          |
| 3.1 Summary of the compositions of the majority V-rich and minority Ni-rich regions within the alloy ingots. The reported compositions are the average compositions as determined by EDS. . . . .   | 44          |
| 3.2 Results from ICP-MS analysis of KOH electrolyte collected from cells containing $\text{Ti}_{29}\text{V}_{62-x}\text{Ni}_9\text{Cr}_x$ ( $x = 0, 6, 12$ ) alloy electrodes. Electrolyte was collected from cells fully charged, discharged to -0.75 V, and discharged to -0.50 V, as indicated in Figure 3.5. Data from a cell cycled 10 times are also presented. . . . . | 50          |
| B.1 ICP-MS analysis of KOH electrolytes in which $\text{Ti}_{29}\text{V}_{62-x}\text{Ni}_9\text{Cr}_x$ ( $x = 0$ and 12) alloy electrodes were stored for 10 days. . . . .  | 73          |
| B.2 Input values and energy density results for an example case of a 100 Wh MH-Air cell. . . . .  | 81          |

## *Chapter 1*

### INTRODUCTION

In the late 1860s, Thomas Graham published "On the Occlusion of Hydrogen Gas by Metals" in which he reported on the absorption and desorption of hydrogen gas by iron, platinum, and palladium.[1] Pure Pd was found to absorb the most hydrogen with a stoichiometry of  $\text{PdH}_{0.772}$  obtained at  $11^\circ\text{C}$  and 756 mmHg pressure. Measurements of electrical conductivity and magnetic properties of PdH led Graham to incorrectly conclude that hydrogen itself is a white, lustrous metal. Following Graham, work by Troost, Hautefeuille, and especially Winkler uncovered hydrides of K, Na, Ce, Ca, Sr, Ba, Y, Th, Zr, and La. One of the first applications of these metal hydrides involved calcium hydride; an apparatus containing CaH was mounted to a carriage to allow for portable production of hydrogen with which to fill the ballast of dirigibles.[2]

Metal hydride research has expanded significantly since early work by Graham et al. The ability to absorb significant quantities of hydrogen, oftentimes with hydrogen densities greater than liquid hydrogen itself, has driven the development of metal hydrides for various technical applications which involve gas compression or hydrogen as an energy source. Recent results have demonstrated that gaseous hydrogen can be produced without  $\text{CO}_2$  emissions through photoelectrochemical water splitting or methane decomposition.[3, 4]. Hydrogen can therefore be used as an energy carrier or energy storage medium for a renewable energy infrastructure. Solar and wind power generated hydrogen can be stored for later use to run fuel cells, or be distributed via pipelines for use in the transportation sector. Recently, hydrogen fuel cell-powered commercial transit options have been introduced including the Toyota Mirai automobile and the Coradia iLint commuter train.[5]

#### **1.1 Metal Hydrides as Energy Materials**

Metal hydrides (MH) as initially discovered, and as will be referred to for the rest of this thesis, consist of an elemental or alloy metal lattice with hydrogen atoms occupying interstitial sites. Rare-earth MH were previously utilized prominently as anode materials in nickel-metal hydride (Ni-MH) batteries, although niche applications including nuclear reactor cladding material, switchable mirrors, and cryogenic cooling for the European Space Agency's Planck mission were developed.[6–9]

Other applications of transition MH include thermal energy storage and multi-stage hydrogen compressors for hydrogen filling stations.[10, 11]

Another class of MH, called complex metal hydrides, is also intensely studied. Complex metal hydrides typically contain an alkali metal cation ionically bonded to a metal- or metalloid-based anion. In these systems, the hydrogen is bonded with heavy covalent character to the anion species. Recently,  $\text{Li}^+$ ,  $\text{Na}^+$ , and  $\text{Mg}^{2+}$  borohydride-based compounds have been demonstrated as potential solid state electrolytes for their respective eponymous ion batteries.[12]

Computational modeling has predicted the existence of several high temperature superconducting MH.[13, 14] These materials contain very high hydrogen concentrations ( $\text{H}/\text{M} \geq 6$ ) and require high pressure and temperature synthesis in a diamond anvil cell. Despite these difficulties, synthesis of superconducting lanthanum superhydride with  $T_c$  approaching 280 K has been reported in the literature.[15] This thesis will not discuss these materials further; interested readers can find more information in the numerous reviews and papers on these topics.

Several academic questions still exist regarding thermodynamics and kinetics of more traditional transition metal and elemental MH. The remainder of this Introduction will provide a brief overview of MH using examples from transition metal and rare-earth MH. An initial overview of basics of hydrogen absorption/desorption, the metal-hydrogen phase diagram and (de)hydriding phase transitions will provide context for theories of hysteresis in MH.

## **1.2 Chemisorption of Hydrogen by Metal Hydrides**

### **Methods of Hydriding**

The absorption of hydrogen (hydriding) by elemental metals or intermetallic and solid solution alloys has been well documented in the literature, with over 2400 hydride-forming metals identified. Typical MH absorb up to 2 hydrogens per metal atom ( $\text{H}/\text{M}$ ), with hydrogen residing in tetrahedral or octahedral interstitial sites.[7, 16] Absorption of hydrogen causes lattice expansions greater than 10% by volume and oftentimes a transition to a different crystal structure.

One convenient aspect of MH is that hydrogen as a solute can be introduced to a host metal which is in the solid state. The diffusivity of hydrogen in elemental metals approaches  $10^{-5} \text{ cm}^2/\text{s}$  at room temperature, allowing for hydriding transitions to be driven by an external source of hydrogen.[17] Typically, hydrogen is introduced to a hydride-forming metal either electrochemically or from the gas phase. These

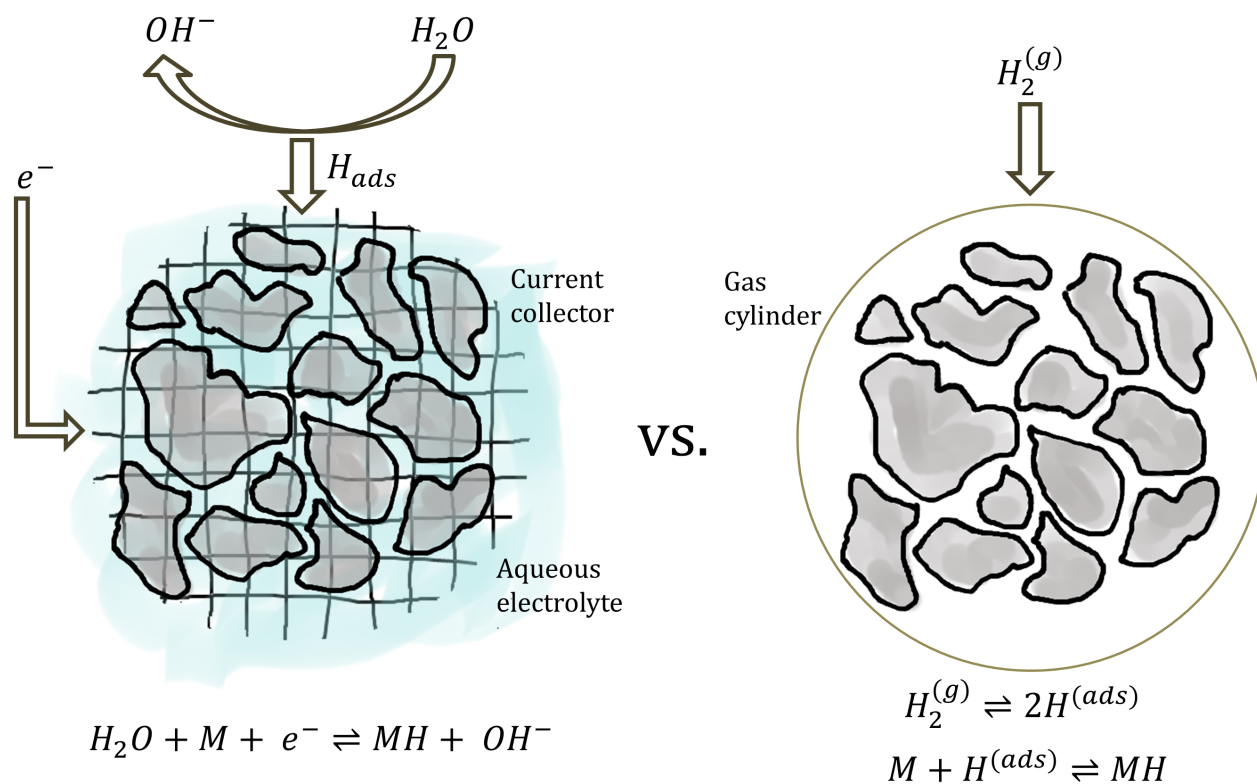


Figure 1.1: Schematic illustrating two methods of hydriding a hydride-forming metal. On the left, hydriding the metal (gray particles) occurs by electrochemical reduction of water in an aqueous electrolyte. The right side illustrates hydriding from the gas phase; a high partial pressure of hydrogen gas is used to drive the hydriding transition.

processes are illustrated schematically in Figure 1.1.

Electrochemical hydriding occurs by redox processes at the surface of an electrode which contains the hydride-forming metal.[7] Reduction of water in an aqueous electrolyte produces an adsorbed hydrogen atom, which diffuses into the hydride-forming metal and subsequently forms an MH. The redox equation associated with this process (see Equation 1.9) is provided in the left panel of Figure 1.1. To desorb hydrogen, the current is reversed, and hydrogen recombines with a hydroxide ion ( $\text{OH}^-$ ) to form water.

Gas-phase hydriding occurs in a similar manner to electrochemical hydriding, and is illustrated in the right panel of Figure 1.1. Hydrogen gas is introduced into a pressure vessel containing a hydride-forming metal. The chemical potential  $\mu$  of the gas is:

$$\mu_{\text{H}_2}^{(\text{g})} = \mu_0 + RT \ln \frac{p_{\text{H}_2}}{p_0} \quad (1.1)$$

with  $R$  the gas constant,  $T$  the temperature, and  $p$  the partial pressure of the gas species. Increasing the hydrogen partial pressure will increase the chemical potential,  $\mu$ , of hydrogen gas until hydride formation becomes thermodynamically favorable (i.e.  $1/2\mu_{\text{H}_2}^{(\text{g})} > \mu_{\text{MH}}$ ).[16] Hydrogen molecules will adsorb on the surface of the hydride-forming metal, dissociate, and diffuse into the metal to form a hydride. Reducing hydrogen chemical potential by reducing partial pressure in the pressure vessel will drive a dehydriding transition, and hydrogen will be released from the MH.

Electrochemical and gas-phase (de)hydriding are related two ways; by electrode potential and hydrogen partial pressure, and by total hydrogen capacity. Electrode potential is defined by the Nernst equation:

$$E = E^0 + \frac{RT}{nF} \ln K \quad (1.2)$$

where  $E$  is electrode potential,  $E^0$  the standard potential,  $n$  the number of electrons in the redox reaction,  $F$  is Faraday's constant, and  $K$  the reaction quotient (often given as the ratio of activities of the reacting species). For metal hydride batteries in an alkaline aqueous electrolyte (6 M potassium hydroxide (KOH) solution, pH = 14) at 293 K,  $n = 1$ , the Nernst equation becomes[7]:

$$E_{\text{MH,eq}}(\text{V vs. Hg/HgO}) = -0.9234 - 0.0291 \log \frac{p(\text{H}_2)}{p_0} \quad (1.3)$$

An Hg/HgO standard reference electrode is typically used in alkaline electrolytes, giving the value of -0.9234 V for the H<sub>2</sub>O/H<sub>2</sub> redox couple. The reaction quotient  $K$  is evaluated as the ratio of activity for H<sub>2</sub>O and H<sub>2</sub>, which can be expressed as the ratio of activity of H<sub>2</sub>O to fugacity of H<sub>2</sub> times partial pressure of H<sub>2</sub> gas. Activity and fugacity values at T = 293 K in 6 M KOH are used to evaluate the leading coefficient in the last term on the right hand side of Equation 1.3.[7] Thus the MH electrode potential in an electrochemical cell can be directly connected to hydrogen partial pressures required for gas phase hydriding.

Electrochemical specific capacity is expressed in mAh/g, whereas gas-phase specific capacity is expressed as either mole fraction (H/M) or weight percent (wt.%). The connection between gas-phase and electrochemical capacity can be determined through simple dimensional analysis. Consider 100 g of MH containing 1 wt.% of hydrogen:

$$\begin{aligned} & \frac{1.0 \text{ g H}}{100 \text{ g MH}} \times \frac{1 e^-}{1 \text{ H}} \times \frac{1.008 \text{ mol H}}{1.0 \text{ g H}} \times 96,500 \frac{\text{C}}{\text{mol}} \times \frac{1000 \text{ mA}}{\text{A}} \times \frac{1 \text{ hr}}{3600 \text{ sec}} \\ & = 266 \left( \frac{\text{mAh}}{\text{g}} \right) \end{aligned} \quad (1.4)$$

Thus 1 wt.% of gas-phase storage corresponds to 266 mAh/g of electrochemical capacity.

### The Metal-Hydrogen Phase Diagram

Metal-hydrogen phase diagrams are constructed from pressure-composition isotherms (PCTs). A PCT is measured by iteratively dosing a reactor containing a hydride-forming metal with an aliquot of hydrogen and allowing the hydrogen partial pressure to equilibrate. With each dose, some amount of hydrogen is absorbed by the metal. This process is reversed to characterize hydrogen desorption.<sup>1</sup> The hydrogen concentration in the metal is evaluated either volumetrically (by accounting for the change in moles of hydrogen gas) or gravimetrically (tracking changes in mass). A phase transition begins when the chemical potentials of two hydride phases are equal. Hydrogen is absorbed or desorbed as one phase replaces the other at a constant partial pressure known as the plateau pressure. Plotting hydrogen partial pressure (or hydriding potential as given by Equation 1.3) on the ordinate indicates the relative stability of the hydride phase; low partial pressures correspond to a

<sup>1</sup>Throughout this thesis, pressure composition isotherms are referred to as absorption or desorption isotherms to designate the direction of the reaction.

hydride phase that readily absorbs hydrogen but is difficult to remove hydrogen from.

Figure 1.2 shows a composite 343 K PCT for the V-H system.[18, 19] Vanadium can absorb up to 2 H/M and goes through two phase transformations; the body-centered cubic (BCC) solid solution  $\alpha$  phase transforms to a tetragonally distorted BCT monohydride  $\beta$  phase at low hydrogen partial pressures. The monohydride phase then transforms to the face-centered cubic (FCC) dihydride  $\gamma$  phase at significantly higher partial pressures. Characterization of the monohydride transition was performed electrochemically due to the difficulty in accurately measuring the low partial pressures with pressure transducers.[18] Plateau pressures for elemental or intermetallic MH phase diagrams are constant. When energetic heterogeneities are introduced in solid solution alloys, these plateaus develop a slope.

Temperature-composition phase diagrams are produced from measurements of PCTs at several temperatures. Phase boundaries are determined from terminal compositions of the plateaus in PCTs, and often narrow with increasing temperature. The temperature-composition phase diagram for VH, as measured by Reilly and Wiswall, is reproduced in Figure 1.3.[19]

### 1.3 Hysteresis in Metal Hydrides

After Graham's work on the absorption of hydrogen by platinum, iron, and palladium, several researchers noticed a peculiarity in the absorption and desorption of hydrogen by palladium[20]:

When  $r_\alpha < r < r_\beta$  ( $r$  the hydrogen concentration) the isotherm is flat; the pressure has a special value, but the amount of hydrogen dissolved is not controlled by it. In this region the system is sluggish, different curves being obtained when hydrogen is added or removed. These "hysteresis" curves, as they are called...

This phenomena of non-reversibility of hydrogen absorption and desorption by MH is known as hysteresis. Pressure hysteresis is conveniently quantified with respect to absorption and desorption pressure[16]:

$$\text{Hysteresis} = \ln \left( \frac{p_{\text{abs}}}{p_{\text{des}}} \right) \quad (1.5)$$

At a constant temperature, the absorption pressure is greater than desorption pressure. Hysteresis also manifests as a difference in terminal compositions at phase

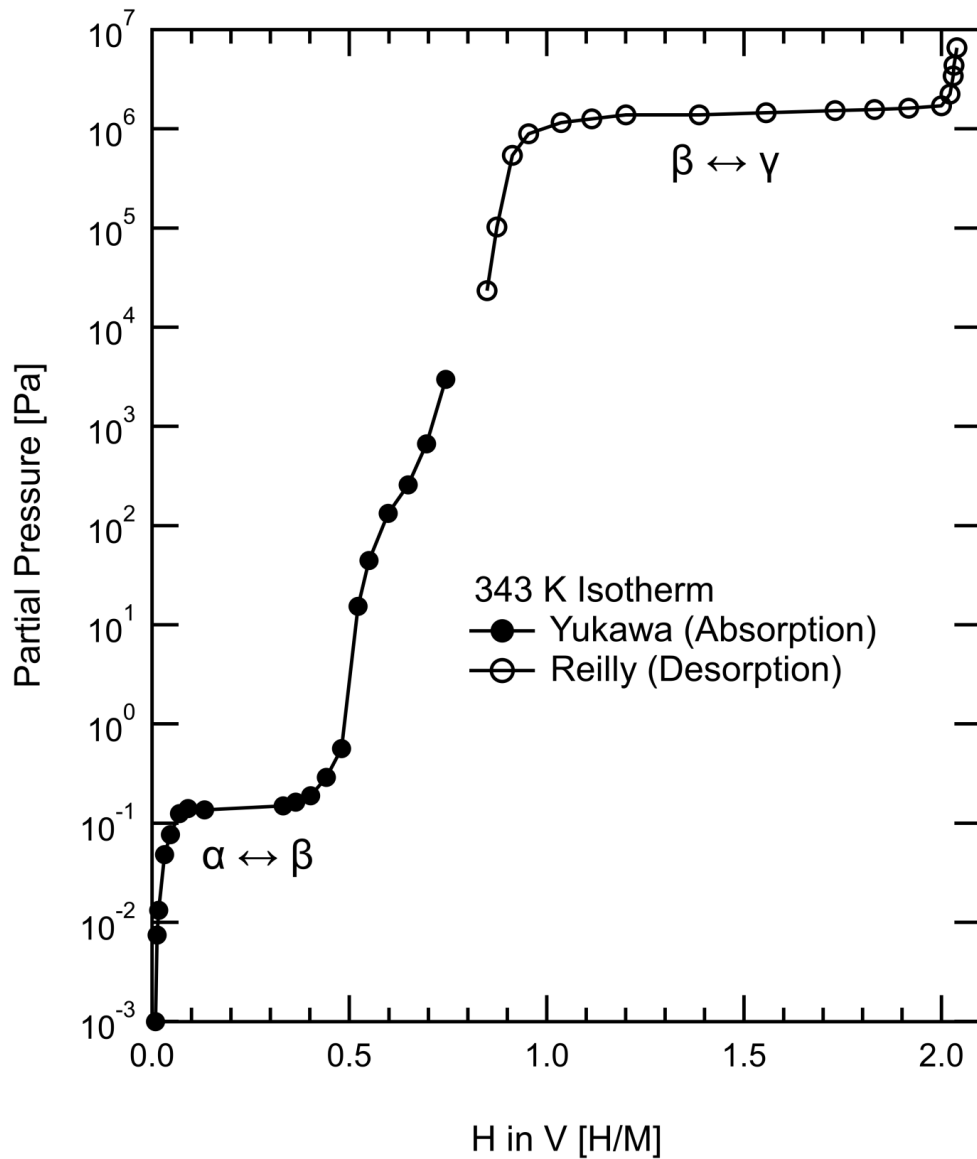


Figure 1.2: Composite PCT for the V-H system as published by Yukawa, et al. and Reilly and Wiswall. Yukawa investigated the monohydride transition electrochemically, whereas Reilly and Wiswall characterized the dihydride transition in the gas-phase.

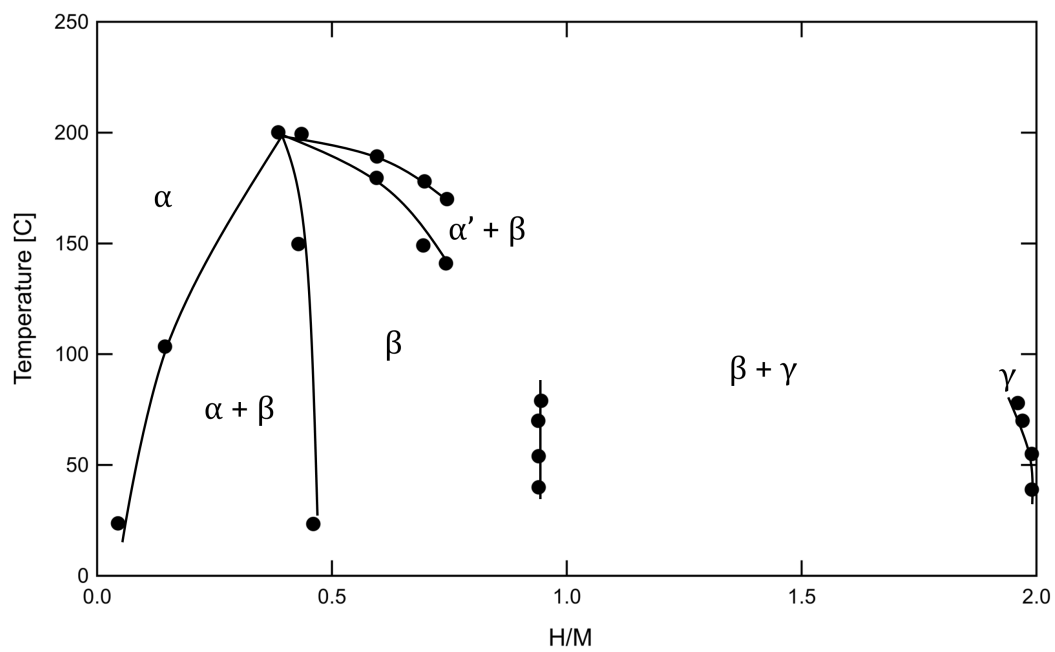


Figure 1.3: Experimentally determined temperature-composition phase diagram for the V-H system. Black circles represent data points, and the connecting lines serve as approximate phase boundaries. The  $\beta/(\beta + \gamma)$  phase boundary is an average value due to the finite width of the vertical component of the PCTs in Figure 1.2.

boundaries for absorption and desorption, a phenomenon known as solvus hysteresis. Pressure and solvus hysteresis in PdH are apparent in the 333 K PCT plotted in Figure 1.4. With absorption and desorption plateau pressures of 75 and 31 Torr, respectively, the pressure hysteresis is 0.88. Solvus hysteresis is less convenient to quantify; the sloping nature of the plateau pressure at the end of the phase transformations makes determination of the phase boundary difficult. Frieske and Wicke used a graphical construction in which the plateau pressure is extended until it intersects with the opposite isotherm branch.[21] The composition at which the intersection occurs is taken as the phase boundary. By this method, the solvus hysteresis in Figure 1.4 is  $0.61 - 0.56 = 0.05$  at the  $\beta$  phase boundary and  $0.04 - 0.015 = 0.025$  at the  $\alpha$  phase boundary. Dashed lines in Figure 1.4 illustrate the graphical construction method.

Hysteresis in MH has been studied extensively, with the majority of the work focusing on PdH and other MH with experimentally convenient transition pressures and temperatures. It is well established that hysteresis decreases with temperature and will disappear above a critical temperature  $T_c$ . Figure 1.5 plots hysteresis as a function of temperature for several bulk PdH studies.[21–23] At 333 K, the reported hysteresis varies by a factor of 2, indicating that hysteresis may have a size dependence. Recently, several investigations of PdH nanostructures have revealed that hysteresis increases with particle size, up to a maximum size of 300 nm.[24, 25] Despite decades of research, no analytical model has been developed which completely describes hysteresis in MH.

### Theories of Metal Hydride Hysteresis and Equilibrium

Early work regarding hysteresis was primarily focused on determining which branch of the PCT is closer to equilibrium. Initially, researchers hypothesized that true equilibrium resides halfway between the two branches. Lacher developed a statistical mechanics model using a Bragg-Williams approximation which was subsequently fit to PdH isotherms[20]:

$$\log_{10} p^{1/2}(\text{atm.}) = \log_{10} \frac{\theta}{1 - \theta} + 2.3009 - (445.6 + 986.7\theta)/T \quad (1.6)$$

with  $\theta$  the fraction of filled H sites in the lattice. The model accurately reproduces isotherms above  $T_c$ , and the pressure is assumed to be constant in a two phase region below  $T_c$ . Lacher claims that hysteresis is due to increased vapor pressure of the nucleating phase due to a small initial size. As a result, a supersaturated  $\alpha$  phase forms during absorption, and an “undersaturated”  $\beta$  phase forms during desorption.

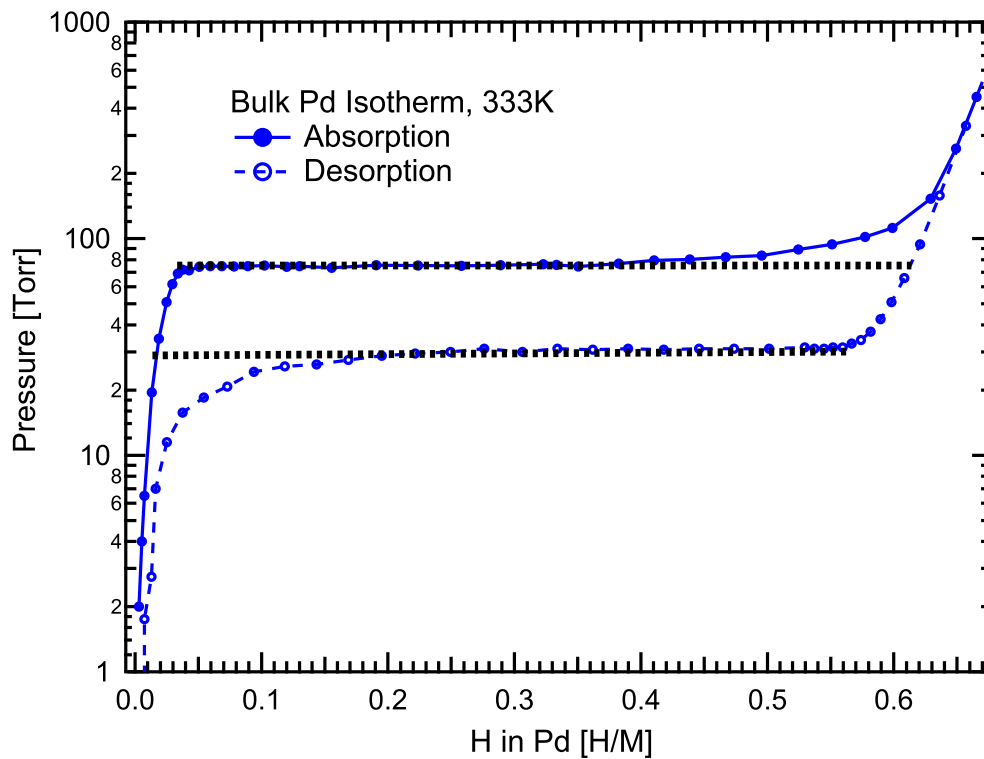


Figure 1.4: Full pressure-composition isotherm for 200 mesh Pd powder measured at 333 K. The Pd powder had been cycled two times prior to this PCT measurement. A hysteresis of 0.88 was calculated using Equation 1.5. Dashed lines illustrate the graphical construction method used to determine phase boundaries in the sloping regions of the plateau.

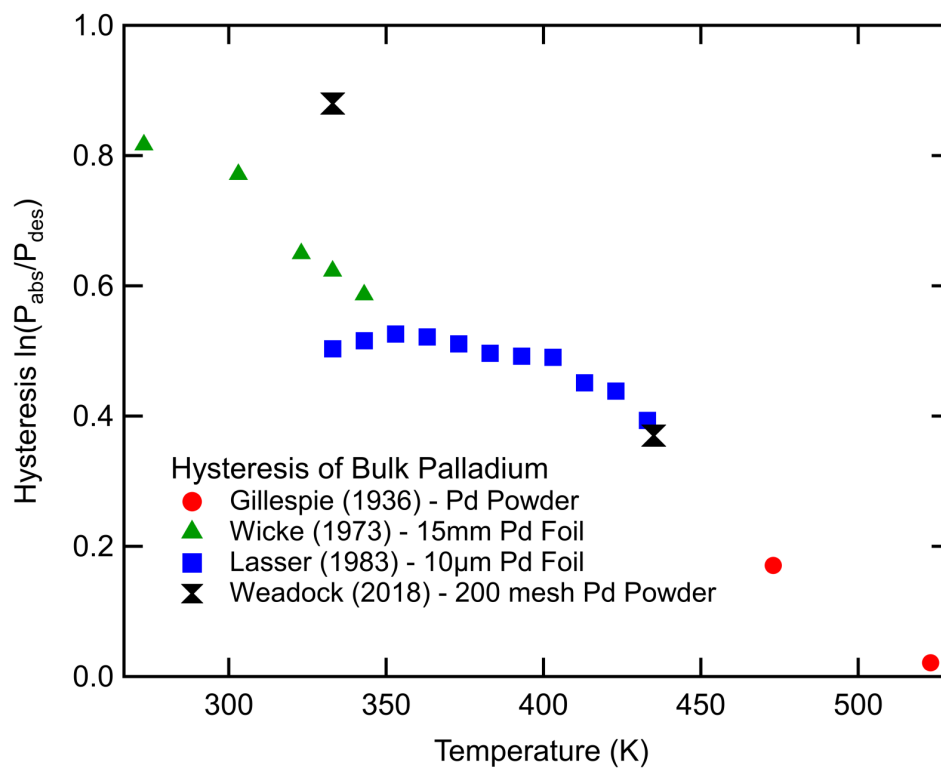


Figure 1.5: Comparison of pressure hysteresis values reported in the literature for bulk Pd.

This conclusion suggests hysteresis affects both branches of the isotherm equally, and true equilibrium exists halfway between these branches. Despite hypothesizing that hysteresis arises from mechanical constraints on the nucleating phase, Lacher's theory does not incorporate lattice expansion of Pd with H.

Everett and Nordon provided a critical review of Lacher's theory, demonstrating that Equation 1.6 does not accurately fit both absorption and desorption branches of PdH PCTs below the critical temperature.[26] Rather, separate functions are required for the  $\alpha$  and  $\beta$  phase indicating that the vibrational partition function or proton-site interaction energy is different in both phases. The phase transformation is not considered complete until a hydrogen concentration is reached at which equations describing absorption and desorption are equal. This fact led Everett and Nordon to question if two-phase reversible equilibrium is possible in PdH. Lacher's description of the origin of hysteresis, however, was accepted and expanded upon by Everett and Nordon. Nuclei of small size in an infinite crystal will have growth suppressed by hydrostatic forces exerted by the matrix. This barrier can only be overcome, the authors claim, by increasing hydrogen pressure. Furthermore, deviations from a flat plateau (evident at the end of the transition in Figure 1.4) were proposed to be due to changes in the energetics of any remaining parent phase caused by lattice strains.

Flanagan et al. carefully studied single phase regions of PdH isotherms and noticed an increase in hydrogen solubility in the  $\alpha$  phase of an unannealed Pd sample as compared to an annealed sample.[27, 28] Similar solubility enhancements were observed in the  $\beta$  to  $\alpha$  transition, leading the authors to propose that hydrogen cycling is accompanied by creation of a high density of dislocations in the metal. Solubility does not increase continually with cycling, therefore dislocations generated beyond an equilibrium dislocation density must be annihilated during the subsequent PCT branch. Flanagan and Clewley proposed that hysteresis is due to the energetic cost of generating dislocations during (de)hydriding and can be expressed in terms of the enthalpy of dislocation formation  $\Delta H_{\text{disl}}$ [29]:

$$\ln \left( \frac{p_{\text{abs}}}{p_{\text{des}}} \right) = \frac{4\Delta H_{\text{disl}}}{RT} \quad (1.7)$$

Analysis of pressure hysteresis is extended to solvus hysteresis, and the change in terminal composition is expressed as a function of the equilibrium pressure and phase boundary compositions.[29] In Flanagan's analysis, the equilibrium values exist halfway between experimentally observed absorption and desorption isotherms.

Other groups claim that the desorption branch represents the true equilibrium of (de)hydriding transitions. Several experiments from the group of Wicke et al. demonstrate that absorption pressure decreases with cycling, whereas the desorption pressure stays relatively constant.[21, 30] Their isotherm measurements on bulk Pd foil and Pd black (i.e. nanocrystalline Pd) revealed a large difference in absorption pressure, but no change in desorption pressure between the samples. Wicke and Blaurock also performed a detailed analysis of solvus hysteresis in PdH and PdD to determine critical hydrogen concentration ( $n_c$ ) at  $T_c$ . [30] Analysis of isotherms measured above  $T_c$  yielded  $n_c = 0.257 \pm 0.004$ , and analysis of subcritical isotherms yielded  $0.25 < n_c^{\text{des}} < 0.26$  and  $0.29 < n_c^{\text{abs}} < 0.30$ . Agreement between the equilibrium supercritical concentration and equilibrium concentration determined on desorption provided additional evidence to the hypothesis that desorption isotherms represent true strain-free equilibrium.

Schwarz and Khachaturyan (S-K) presented a material-agnostic analysis of hysteresis which considers how elastic strains modify thermodynamics of two-phase hydriding and dehydriding phase transitions.[31, 32] When nucleation proceeds coherently, an elastic energy term is introduced, which depends solely on the total concentration  $\bar{c}$  of solute atoms (and not volume fraction or solute distribution between two phases). This is known as the Bitter-Crum theorem, a result derived from Eshelby's theory for elastic inclusions in an infinite matrix.[33–35] In the Bitter-Crum theorem, the two phases are required to have the same elastic constant and be elastically isotropic. All strains are purely dilatational, the crystal is assumed infinite, and no interactions between solute atoms are included.

According to S-K theory, the free energy of a coherent system is equal to the sum of the "chemical" free energies of the two phases plus a coherent strain energy term.[31, 32] The hydriding and dehydriding transitions begin at the compositions  $c_\alpha^{\text{coh}}$  and  $c_\beta^{\text{coh}}$ , which are determined from the common tangent construction between these chemical free energies. In the incoherent case, the free energy of the system becomes a weighted sum of free energies (chemical plus elastic) of each phase, there is no additional coherency term. The miscibility gap in this case is determined by a common tangent construction between the total free energy curves. Incoherent terminal compositions are  $c_\alpha^{\text{inc}} < c_\alpha^{\text{coh}}$  and  $c_\beta^{\text{inc}} > c_\beta^{\text{coh}}$ .

For coherent nucleation, the consequence of the elastic strain energy depending solely on the total solute concentration is that the chemical potential in the two phase region is no longer determined by a common tangent construction and instead

decreases linearly with  $\bar{c}$ . In the case of hydriding, the inclusion of the energy barrier shifts the system to the total free energy curve (chemical plus elastic) with a corresponding increase in chemical potential. The  $\alpha$  to  $\beta$  transition begins at  $\mu(c_\alpha^{\text{coh}}) > \mu(c_\beta^{\text{coh}})$ , and is complete when  $\bar{c} = c_\beta^{\text{end}} > c_\beta^{\text{coh}}$ . The effect is similar for dehydriding; the transition begins at  $\mu(c_\beta^{\text{coh}}) < \mu(c_\alpha^{\text{coh}})$  and ends with  $\bar{c} = c_\alpha^{\text{end}} < c_\alpha^{\text{coh}}$ . In an open coherent system, this macroscopic nucleation barrier can only be overcome by increasing (or decreasing) the chemical potential of hydrogen gas to match the shift between free energy curves.<sup>2</sup> In S-K theory, the presence of the barrier results in a pressure hysteresis given by:

$$\ln\left(\frac{p_{\text{abs}}}{p_{\text{des}}}\right) = \frac{8v_0G_s\frac{1+\sigma}{1-\sigma}\epsilon_0^2(c_\beta^{\text{coh}} - c_\alpha^{\text{coh}})}{k_B T} \quad (1.8)$$

where  $G_s$  is the shear modulus,  $\sigma$  the Poisson ratio,  $\epsilon_0$  the fractional change in lattice parameter with respect to hydrogen concentration, and  $c_\beta^{\text{coh}}$  and  $c_\alpha^{\text{coh}}$  as defined above.  $v_0$  is the molar volume of the hydride-forming metal. If total strain energy associated with hydriding overcomes the elastic limit, coherency will be lost and hysteresis will be reduced. As such, these results provide an upper bound on pressure hysteresis. The formalism developed by Schwarz and Khachaturyan also accounts for the solvus hysteresis, although no explicit expression is derived.

Qian and Northwood recognized that large stresses associated with hydriding will cause yielding at the matrix-precipitate interface and developed an expression for the hysteresis in terms of irreversible work due to elastoplastic deformation associated with accommodating a growing precipitate.[36] Their analysis also considered changes in mechanical properties with composition and size. The accommodation energies depend on the yield stress of the matrix; if mechanical properties of the hydride phase are different than the metal, hysteresis will not be symmetric. Accommodation energy is also modified by particle size. When precipitate size is comparable to the matrix, e.g. in nanoparticles, internal stresses are mitigated by "image" forces at the free surface. If stresses are reduced below the yield stress of the matrix, no plastic deformation will occur and the transformation will be entirely elastic.

Recently, Griessen et al. developed a mean field model to predict size dependent spinodal pressures and associated hysteresis in Pd nanostructures.[24] Unlike some earlier models mentioned, elastic and electronic H-H interactions are included (as-

---

<sup>2</sup>This result is also proposed by Everett and Nordon, however Schwarz and Khachaturyan provided a rigorous thermodynamic derivation to prove this statement.

sumed to be the same as in bulk Pd). This model assumes a coherent core-shell hydriding geometry with differing hydrogen concentrations in each component and accounts for the associated surface tension and clamping contributions. Enthalpies of formation for the core and shell are obtained from fits to several datasets. Experimental hysteresis values are reproduced for numerous Pd nanostructures (some not included in the initial fitting) by assuming a coherent transition with a modified surface-shell-core coupling. However, recent experimental studies demonstrate that spherical cap nuclei are energetically favorable to core-shell geometries assumed in the Griessen, et al., model.[25, 37] An increased solubility of hydrogen in the  $\alpha$  phase and reduction in total capacity is attributed to thermodynamically-distinct absorption sites on or near nanostructure surfaces.[24, 38, 39]

Other theories of hysteresis have been published in the literature, with experimental studies of hysteresis existing for PdH, LaNi<sub>5</sub>H, NbH, UH, ZrNiH, and others.[40] In all cases, the proposed origin is either elastic or plastic deformation or some combination of the two. As such, this section of the Introduction is not exhaustive and instead serves to introduce hysteresis and provide relevant recent examples from the literature.

Chapter 2 presents an experimental study of hysteresis in bulk and nanocrystalline Pd. A comparison of isotherm measurements and *in situ* X-ray diffraction observations of the phase transformations are used to evaluate aforementioned theories of hysteresis and "equilibrium" PCTs.

### **Effects of Metal Hydride Hysteresis**

The effect of hysteresis in MH systems is that hydrogen absorption and desorption are no longer reversible in the thermodynamic sense below  $T_c$ . In this temperature regime, desorption of hydrogen from a metal hydride will not occur along the absorption branch. As will be demonstrated in Section 2.3, reversing even an incomplete hydrogen absorption process (a so called "minor loop")[41] is not possible. Thus, the existence of hysteresis results in a thermodynamic inefficiency for engineering systems which utilize MH. These inefficiencies manifest for both gas-phase and electrochemical hydrogen absorption and desorption, as evidenced by the following examples:

- Consider a hydrogen fuel cell with a MH tank as the hydrogen storage medium. The fuel cell requires a hydrogen pressure of 30 psig to run, so an MH must be chosen which will desorb hydrogen at a partial pressure greater than 30

psig at the operating temperature.[42] At 100° C,  $\text{LaNi}_{5.68}\text{Sn}_{0.32}$  desorbs hydrogen at 43 psi.[43] Due to the hysteresis, hydrogen absorption at the same temperature occurs at 47 psi. Thus an additional work term associated with the compression of hydrogen to 47 psi must be considered in calculating the efficiency of this MH-fuel cell system.

- Hysteresis inefficiencies in an electrochemical MH system (Ni-MH battery) are apparent from the Nernst equation (1.3). From the second term on the right-hand side, we see that the potential changes by 29.1 mV per decade of pressure. For  $\text{LaNi}_5$ -based metal hydride electrodes, hysteresis can result in charge/discharge overpotentials up to 20 mV for a cell with an operating voltage of 1.2V.[44]

In both cases, the inefficiency may not represent a large portion of the useful work obtained from the system, but with continued cycling of the system, these small losses will sum to a significant amount.

In addition to theoretical work regarding the origin of hysteresis, there has been significant effort in developing strategies to reduce or eliminate it. Alloying of pure elemental or intermetallic hydrides has been demonstrated to reduce hysteresis and the width of the two phase region. Substitution of up to 10% of Ni with Ge in  $\text{LaNi}_5$  reduces hysteresis by a factor of five at room temperature, with a reduction in hydrogen capacity of 25%.[44] Alloying Pd with several metals, most notably Ag, reduces and in some cases eliminates the two phase region at a constant temperature.[45] Wang et al. found a near elimination of hysteresis in an internally oxidized Pd/ $\text{Cr}_2\text{O}_3$  composite at 493 K, a temperature at which pure Pd still exhibits significant hysteresis.[41] The authors propose this is a microstructure effect but provide no microstructural analysis.

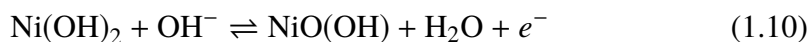
Another avenue of reducing hysteresis is to use a nanosized MH. As demonstrated in Section 2.3, nanocrystalline Pd has a smaller hysteresis than bulk Pd at the same temperature, but also a smaller capacity. It is apparent that there is a trade off between a decreased capacity or reduced hysteresis. When designing an MH system, it is therefore important to weigh which aspect will have a more deleterious effect on the overall performance of the system.

#### 1.4 Nickel-Metal Hydride Batteries

The most well-known application of MH is the Ni-MH battery, which served as the rechargeable battery of choice prior to the introduction of Li-ion batteries. In these systems, a Ni(OH)<sub>2</sub>/NiO(OH) cathode is paired with a hydride-forming metal anode, and charge/discharge reactions at the anode proceed according to the schematic in Figure 1.1. The redox reaction at the anode is:



with the redox potential determined by Equation 1.3. On the cathode side, the redox reaction is:



with an associated redox potential of 0.41 V vs. Hg/HgO. In Equations 1.9 and 1.10, moving from right to left corresponds to charging.

There are additional constraints when using MH for electrochemical hydrogen storage. In an aqueous electrolyte, the charging potential must be less negative than the potential for hydrogen evolution to facilitate absorption of evolved hydrogen. Otherwise, the pressure of the cell can increase, resulting in catastrophic failure. If the MH cannot catalyze the reduction of water to form hydrogen, an electrocatalyst must be incorporated into the electrode formulation to evolve hydrogen to be absorbed by the hydride-forming metal. The final constraint is that the MH should be stable against corrosion in the aqueous alkaline electrolyte. Corrosion can be addressed with alloying or encapsulation with an inert metal (such as Pd), but both options often result in a loss of specific capacity.[18, 46, 47] In Chapter 3, an alternative option of electrolyte modification is presented as a promising way to mitigate corrosion.

The first Ni-MH battery was demonstrated by Battelle in 1967 and utilized a TiNi-based AB alloy as the anode.[7, 48] State-of-the-art commercial MH alloys are “AB<sub>5</sub>” alloys based on the Haucke phase of LaNi<sub>5</sub>. These alloys have been heavily developed, with substitutions on both the La and Ni sites to reduce cost, alter the hydride stability, and improve the lifetime.[7] Lanthanum is often substituted with mischmetal, (Mm) a less expensive mixture of rare-earth metals primarily composed of Ce (30 - 52 wt%) and La (13 - 25 wt%). Other La site substitutions include Ce, Pr, Nd, Zr, and Hf. Substitutions on the Ni site include Sn, Al, Mn, Cu, Co, Cr, Fe, Si, and Zn.[7, 44] These AB<sub>5</sub> alloys offer a reversible capacity of around 300 mAh/g.[49–51] Development of a higher capacity anode would make Ni-MH

batteries competitive with Li-ion batteries in terms of energy density, with the added safety benefit of using an aqueous electrolyte rather than an organic one.

For many years, vanadium-based BCC alloys have been proposed as higher capacity alternatives to AB<sub>5</sub> materials.[52–55] Pure V absorbs up to 2 H/M, which corresponds to 3.9 mass% hydrogen storage capacity, or 1037 mAh/g theoretical electrochemical capacity. The VH ↔ VH<sub>2</sub> phase transformation takes place at 4 atm hydrogen equilibrium pressure at 313 K, which can be altered to some extent by alloying with other transition metals.[19, 56, 57] The V ↔ VH phase transformation occurs at a very low hydrogen equilibrium pressure (on the order of 10<sup>-6</sup> atm), and this monohydride transition is generally considered to be too stable for electrochemical applications.[18] This limitation has been thought to restrict the accessible electrochemical capacity of V-based BCC alloys to half of their theoretical values.[47] There is little physical evidence, however, of the extent of the phase transformation or even if electrochemical dehydrogenation of the monohydride phase is possible at all.

Vanadium is often alloyed with titanium for lower cost and faster hydrogen absorption kinetics.[18, 58–60] Nickel is indispensable for electrochemical activity, and many studies focused on the Ti-V-Ni ternary system as electrode materials for Ni-MH batteries.[54, 61] The Ti-V-Ni-based alloys tend to unmix chemically on the BCC lattice, forming an electrocatalytically active Ni-rich minority region (maximum hydrogen capacity of 1.3 mass%) and a majority V-rich region which forms a high capacity MH.[47, 52, 53, 62–66] One of the highest capacity BCC alloy compositions is TiV<sub>2.1</sub>Ni<sub>0.3</sub>, or Ti<sub>29</sub>V<sub>62</sub>Ni<sub>9</sub>. The hydrogen absorption capacity for Ti<sub>29</sub>V<sub>62</sub>Ni<sub>9</sub> was reported to be 4.0 mass% in gas-phase reactions; electrochemically, however, it discharges 470 mAh/g initially before quickly losing one third of its capacity in 10 cycles.[47] Dissolution of V from the electrode was identified as the cause of the electrode failure. The cycle performance was improved by alloying with Cr, but the capacity of Ti<sub>29</sub>V<sub>62-x</sub>Ni<sub>9</sub>Cr<sub>x</sub> ( $x \leq 12$ ) alloy electrodes still decreased substantially over 30 cycles.[46] Recently, the same group reported further improvement of cycle stability for a Ti<sub>29</sub>V<sub>44</sub>Ni<sub>9</sub>Cr<sub>18</sub> alloy, but with a much lower reversible capacity of about 300 mAh/g.[67] The trade-off between long cycle life and high capacity suggests it may not be possible to develop Ti-V-Ni-based alloy electrodes by Cr-substitution alone. Chapter 3 is focused on the development of stable V-based BCC MH electrodes.

## Chapter 2

# ELASTIC ENERGY AND THE HYSTERESIS OF PHASE TRANSFORMATIONS IN PALLADIUM HYDRIDE

### 2.1 Chapter Overview

The palladium-hydrogen system is the prototypical metal hydride (MH), and a convenient one for studying hysteresis. Face-centered cubic (FCC) palladium undergoes an isostructural expansion of approximately 10% when it absorbs up to 0.7 H per Pd.[68] Hydrogen absorption and desorption occurs quickly, and at convenient hydrogen partial pressures in the range of  $10^3$  to  $10^5$  Pa. The hysteresis behavior of both bulk and nanoscale PdH has been studied previously, and there is a clear trend of size dependence.[24, 25, 37, 69–76] The (de)hydriding transitions of bulk and nanoscale PdH are characterized with simultaneous measurements of pressure composition isotherms and *in situ* X-ray diffraction. This is the first such study for nanoscale PdH. Previous *in situ* studies on nanoscale PdH have used hydrogen partial pressure, lattice parameter, luminescence, or plasmon intensity as a proxy for hydrogen concentration.[37, 69, 71, 74, 75, 77, 78] Directly measured hysteresis, composition dependent phase fractions, and lattice parameters are used to evaluate some of the theories of hysteresis in metal hydrides presented in Chapter 1, and show a directional dependence of the coherent spinodal phase diagram.

### 2.2 Experimental Details

Palladium powder (200 mesh, 99.95% metals basis) was purchased from Alfa Aesar (Ward Hill, MA, USA). The powder was annealed at 1273 K for one hour under  $N_2$  flow in a Lindberg horizontal tube furnace before any hydriding experiments. Palladium nanopowder (99.95%) was purchased from US Research Nanomaterials, Inc., (Houston, TX, USA) and degassed at 353 K for at least 8 hours prior to any hydriding experiments.

*In situ* X-ray diffraction (XRD) experiments were performed using an Inel CPS 120 powder diffractometer utilizing  $Mo K\alpha$  radiation. A Si  $\langle 110 \rangle$  single crystal oriented in the  $\langle 220 \rangle$  direction was used as the incident beam monochromator. Two-theta calibration of the CPS 120 detector was performed with a NIST SRM 660a ( $LaB_6$ ). More details of the diffractometer alignment and data processing can be found in Appendix C. At least 200 mg of sample was first loaded into a temperature controlled

vertical sample holder, then placed into a stainless steel chamber (980 mL) with a Be window. This reactor is connected to a gas manifold with VCR fittings and MKS Baratron pressure transducers. Prior to hydrogen uptake, the sample was evacuated at 353 K for 72 hours. Each sample was cycled at least once prior to collection of data presented here. At least two complete isotherms were measured for each temperature.

Electron micrographs of annealed bulk Pd powder were acquired with a high resolution Zeiss 1550VP Field Emission scanning electron microscope (SEM). Nanocrystalline Pd powder was analyzed with bright and dark-field transmission electron microscopy (TEM) using an FEI Tecnai F-30UT STEM. The powder was dispersed in isopropanol and sonicated one hour to reduce agglomeration before loading on an amorphous carbon grid for TEM characterization.

Pressure-composition isotherms of bulk Pd powder and nanocrystalline Pd powder were also measured on an independent volumetric Sievert's type apparatus. At least 1.0 g of sample were loaded into an AISI 316L stainless steel reactor (5 mL) and evacuated (baseline  $10^{-5}$  Pa) at 473 K (bulk Pd) or 353 K (nanocrystalline Pd) for 8 hours. Each sample was cycled at least once prior to collection of data presented here, and at least two complete isotherms were measured.

Hydrogen concentrations in the sample were calculated volumetrically with the NIST REFPROP database.[79, 80] Absorption and desorption isotherms were measured at 333 K for both the *in situ* XRD and Sievert's-type apparatus experiments. An additional pressure composition isotherm was measured on the Sievert's-type apparatus for bulk Pd at 435 K. At each hydriding (dehydriding) step, equilibration was reached when pressure in the reactor did not change for a period of 15 minutes. After equilibration, the next quantity of hydrogen was added (removed for dehydriding) from the reactor.

### 2.3 Results

The structure of the bulk and nanocrystalline Pd powders were investigated with SEM and TEM, respectively. A high-resolution TEM image of nanocrystalline Pd is provided in Figure 2.1, and SEM images of bulk Pd are provided in Appendix A (Figure A.1). Annealed bulk Pd particles are  $43.5 \pm 12.90 \mu\text{m}$  in size with easily distinguishable coalesced grains  $3.0 \pm 1.26 \mu\text{m}$  in diameter. The nanocrystalline Pd consists of agglomerated crystallites  $7.47 \pm 2.35 \text{ nm}$  in diameter, as measured from dark field images. A representative dark field TEM image (inverted) is provided in

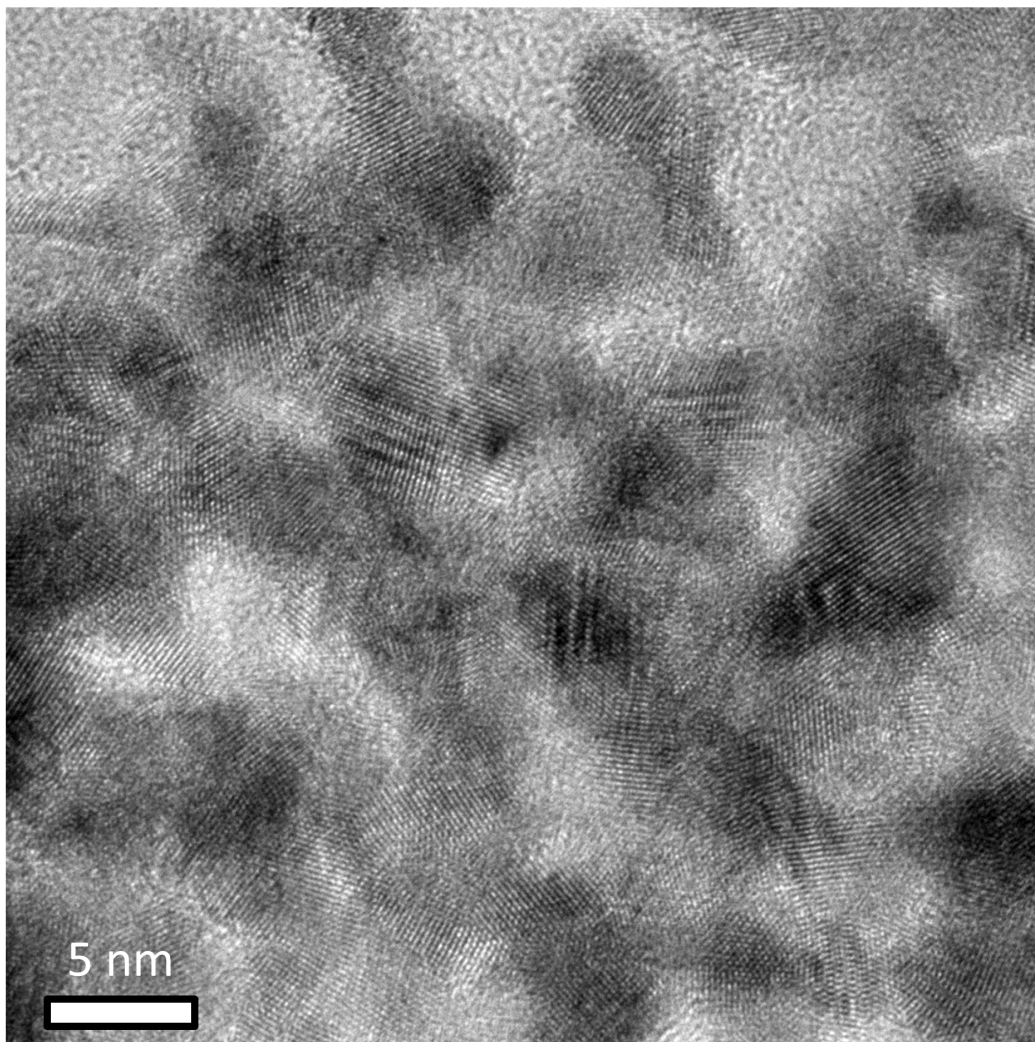


Figure 2.1: High-resolution TEM image of as-received nanocrystalline Pd powder prior to hydrogen exposure.

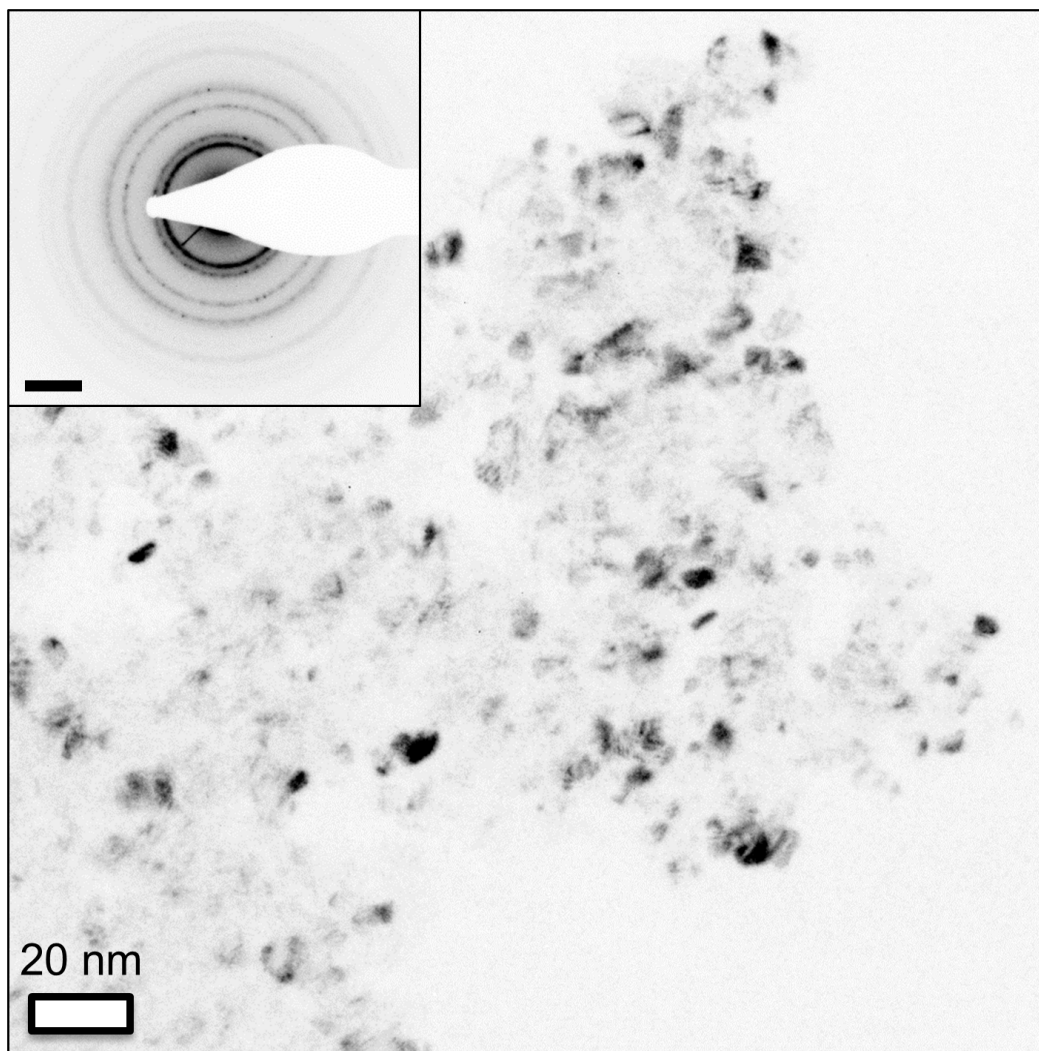


Figure 2.2: Inverted dark field TEM micrograph of the nanocrystalline Pd with inverted electron diffraction pattern (330 mm camera length) inset. The dark field image was acquired with a  $10\ \mu\text{m}$  objective aperture capturing 111 diffracted beams. A  $40\ \mu\text{m}$  selected area aperture was used when acquiring the electron diffraction pattern. Scale bar for the electron diffraction pattern is  $2\ \text{nm}^{-1}$ .

Figure 2.2 with the corresponding electron diffraction pattern inset.

Pressure-composition isotherms measured on a Sievert's apparatus for bulk and nanocrystalline Pd are plotted in Figure 2.3a. Uptake values of approximately 0.6 and 0.7 H/M are found for the nanocrystalline and bulk PdH, respectively, consistent with other reports.[38, 39, 73] The 333 K pressure hysteresis measured from the isotherms (according to the left hand side of Equation 1.8) is 0.37 for nanocrystalline PdH and 0.88 for bulk PdH. High temperature hysteresis of the bulk PdH at 435 K is 0.37. A significant reduction in the absorption plateau pressure for the nanocrystalline PdH (from 10 kPa to 6.9 kPa) contributes primarily to the reduction in the hysteresis at 333 K. Only a small increase in the desorption plateau is observed for the nanocrystalline PdH. Another important difference is that the transition is more gradual for the nanocrystalline PdH; a sharp initial transition is observed for the bulk PdH.

Figure 2.3b plots a minor loop isotherm for PdH measured on the *in situ* system in which the hydriding transformation was stopped at 80% completion then reversed. Rather than traversing back along the absorption branch, the pressure decreases to the desorption branch before significant quantities of hydrogen are removed. Similar results have been reported previously.[41]

Isotherms measured during the *in situ* hydriding experiments are consistent with those plotted in Figure 2.3a. They are compared in Figure A.2 and discussed in Appendix A. The hysteresis measured in both apparatuses are the same.

The *in situ* diffraction patterns from a full hydriding and dehydriding cycle for the bulk and nanocrystalline PdH powders are shown in Figures 2.4 and 2.5, respectively. Raw diffraction data were initially processed with a deconvolution algorithm to remove instrument effects. Rietveld refinement with the GSAS-II software package was subsequently used to extract phase fraction and lattice parameter data from the deconvoluted *in situ* XRD results.[81] The bulk and nanocrystalline PdH data were both fit to a two-phase model consisting of the solid solution  $\alpha$ -phase and hydride  $\beta$ -phase, with the sum of the phase fractions constrained to be unity.[77] Crystallite size for nanocrystalline PdH was set at 7 nm, as determined by TEM and consistent with XRD.

The phase fraction of  $\alpha$  phase as a function of hydrogen content for both bulk and nanocrystalline Pd is plotted in Figure 2.6. Our direct measurement of hydrogen content in nanocrystalline PdH is different than other studies which convert lattice

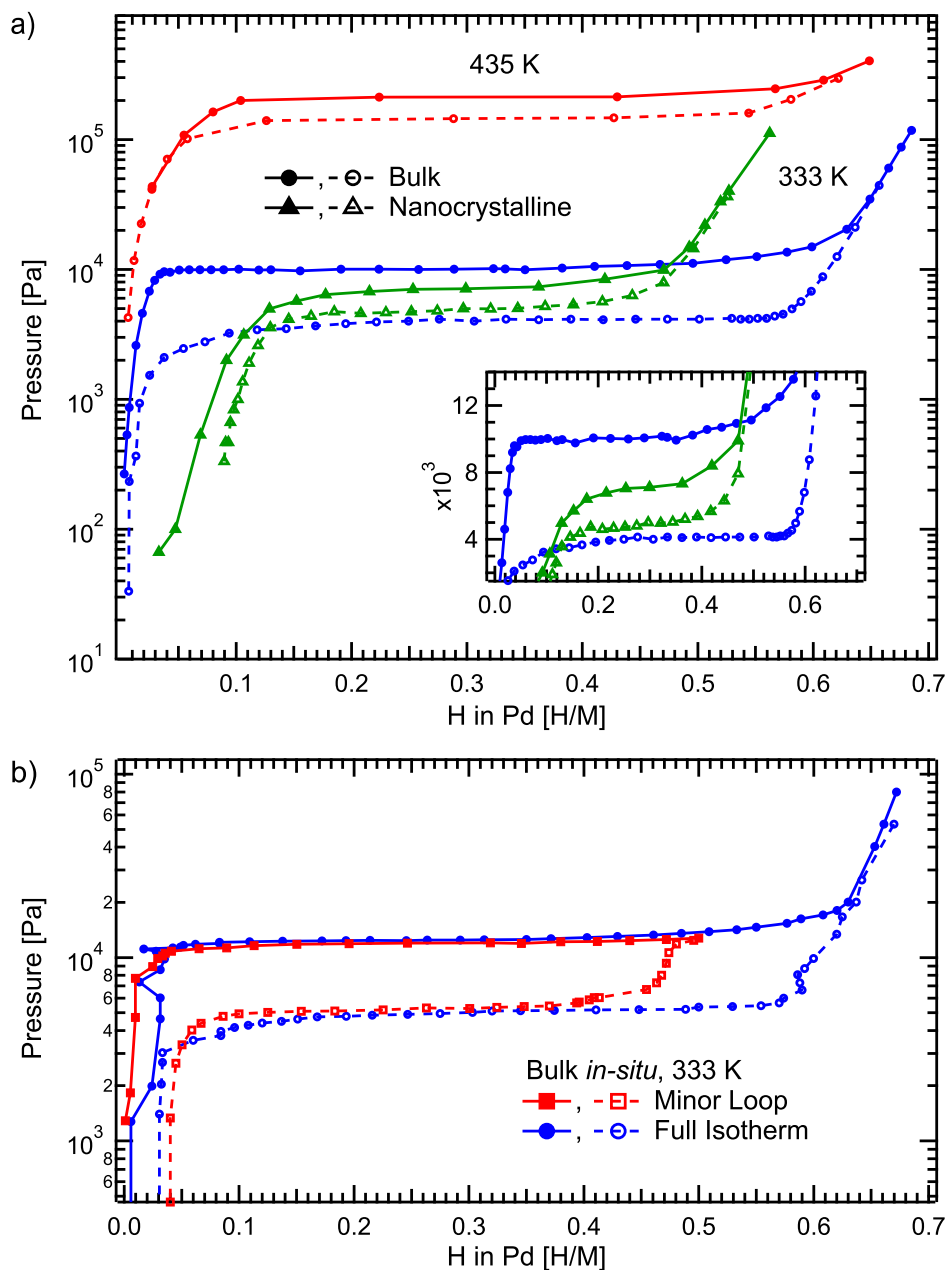


Figure 2.3: a) Pressure-composition isotherms for bulk and nanocrystalline PdH. An additional isotherm of the bulk PdH was measured at 435 K. The inset plots the plateau region on a linear pressure scale to highlight the shape of the isotherm curves. Closed symbols denote absorption, and open symbols correspond to the subsequent desorption. b) 333 K minor loop for bulk PdH measured *in situ*. After hydriding to approximately 80% transformed, the isotherm was reversed and the sample was dehydrided.

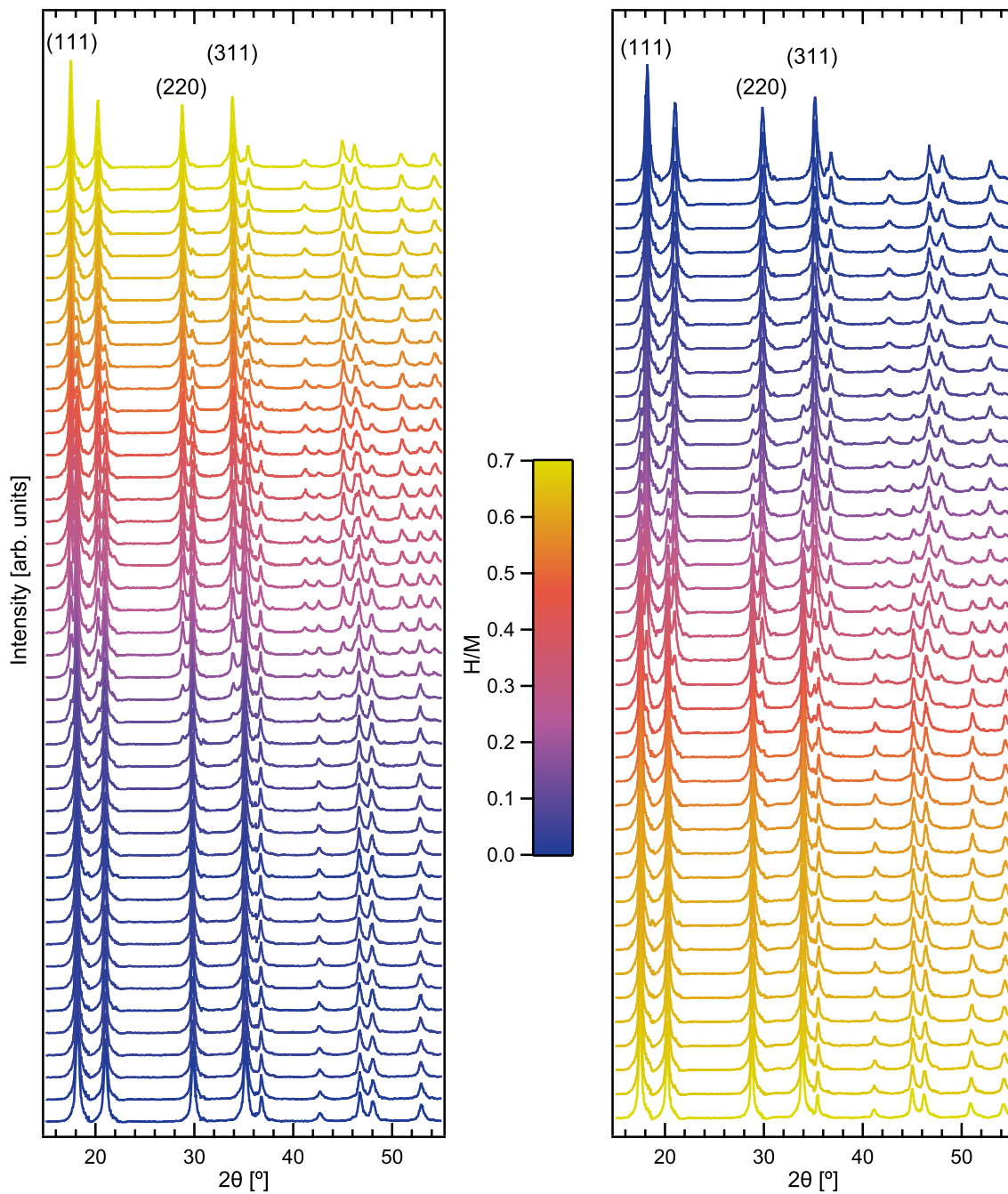


Figure 2.4: *In situ* X-ray diffraction patterns of hydrogen absorption (left) and desorption (right) by bulk Pd powder. The color of each trace corresponds to the total hydrogen concentration (in H/M) as indicated by the central legend.

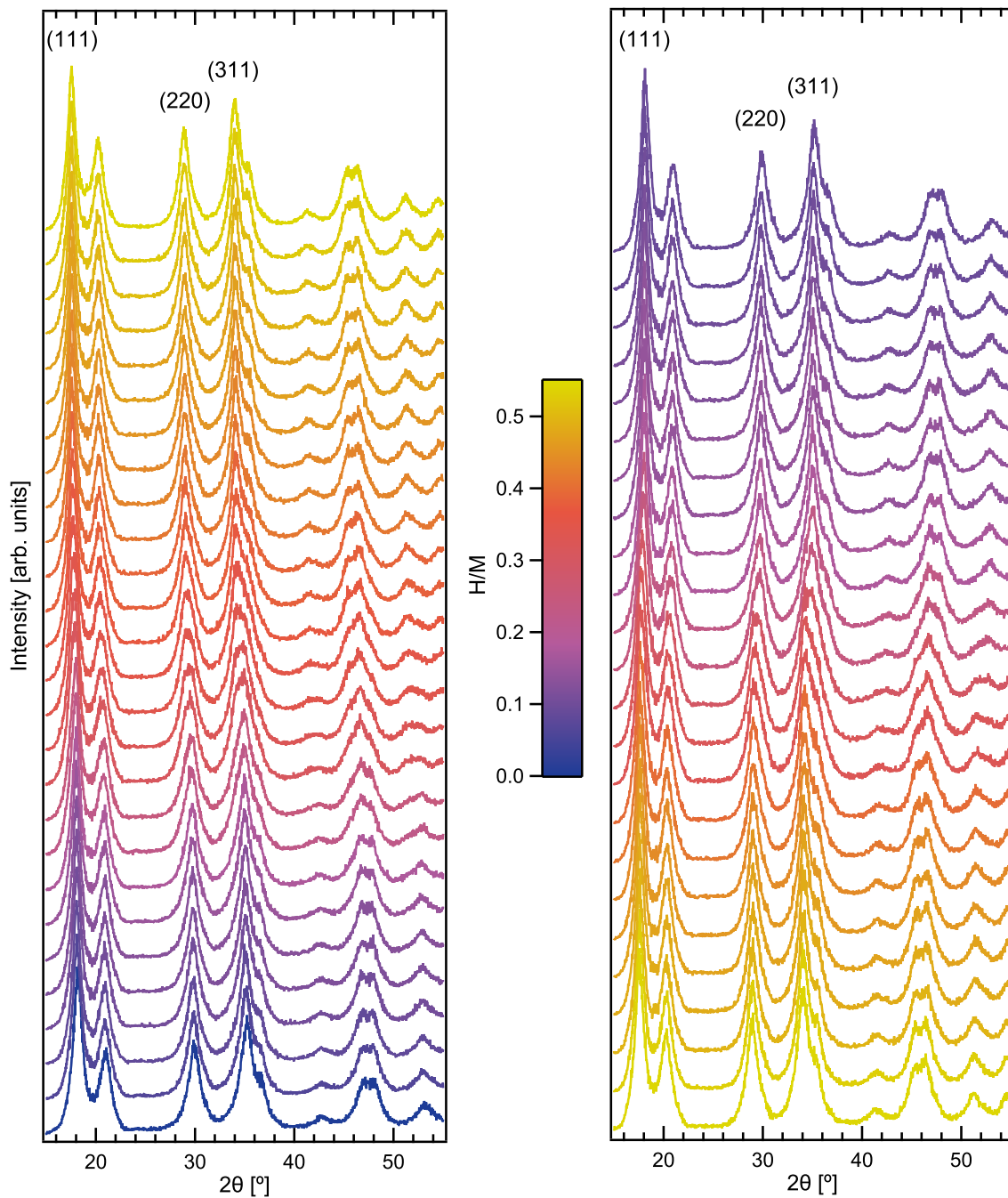


Figure 2.5: *In situ* X-ray diffraction patterns of hydrogen absorption (left) and desorption (right) by nanocrystalline Pd powder. The color of each trace corresponds to the total hydrogen concentration (in H/M) as indicated by the central legend.

Table 2.1: Terminal compositions of the hydriding transition for bulk and nanocrystalline PdH obtained from *in situ* XRD results at 333 K. High temperature (435 K) compositions for the bulk Pd are evaluated from the pressure composition isotherm.

| Sample                    | Bulk  |       | Nanocrystalline |
|---------------------------|-------|-------|-----------------|
|                           | 333 K | 435 K | 333 K           |
| $c_{\alpha}^{\text{abs}}$ | 0.04  | 0.10  | 0.125           |
| $c_{\beta}^{\text{abs}}$  | 0.63  | 0.59  | 0.47            |
| $c_{\alpha}^{\text{des}}$ | 0.013 | 0.07  | 0.115           |
| $c_{\beta}^{\text{des}}$  | 0.56  | 0.51  | 0.46            |

parameter to hydrogen content using a  $3(\Delta a/a_0) = 0.19\Delta c$  relationship reported for bulk PdH.[17, 69, 77] In Figure 2.6a, the rate of transformation in bulk PdH is greater than linear until an inflection point halfway through the transformation. Past this, the rate of transformation remains linear until the phase transformation is complete. This is in contrast to the results for nanocrystalline PdH (Figure 2.6b) which exhibit a much more linear transformation. The phase fraction data is used to determine terminal compositions of the two-phase region. Terminal compositions are identified as the composition at which the  $\alpha$ -phase fraction changes from a constant value in the single phase region of the isotherm. These compositions are reported in Table 2.1. Other studies use graphical constructions or analytical models to determine terminal compositions.[30, 69, 82] Vogel et al. report a much larger solvus hysteresis in PdH nanoparticles than we report for nanocrystalline PdH powder. Their *in situ* isotherms contain fewer data points and do not directly measure hydrogen concentration, however.[77] No *in situ* data was measured for bulk PdH at 435 K because the hydrogen environment chamber is not suited to accommodate required hydrogen partial pressures. In this case, terminal compositions were determined by the graphical method proposed by Wicke et al. in which the plateaus are extended to the opposite isotherm branch, and the intersection point is taken as the terminal composition.[30]

Refined lattice parameters are plotted in Figure 2.7. Variation of lattice parameter with hydrogen concentration in single phase regions was fit to a linear function (Vegard's law); the results are summarized in Table 2.2. Within the two-phase region, lattice parameters for bulk phases are constant but there is variation in nanocrystalline Pd. This is apparent in the continual increase in  $\alpha$  phase lattice parameter during absorption. Lattice parameters for both phases are larger for

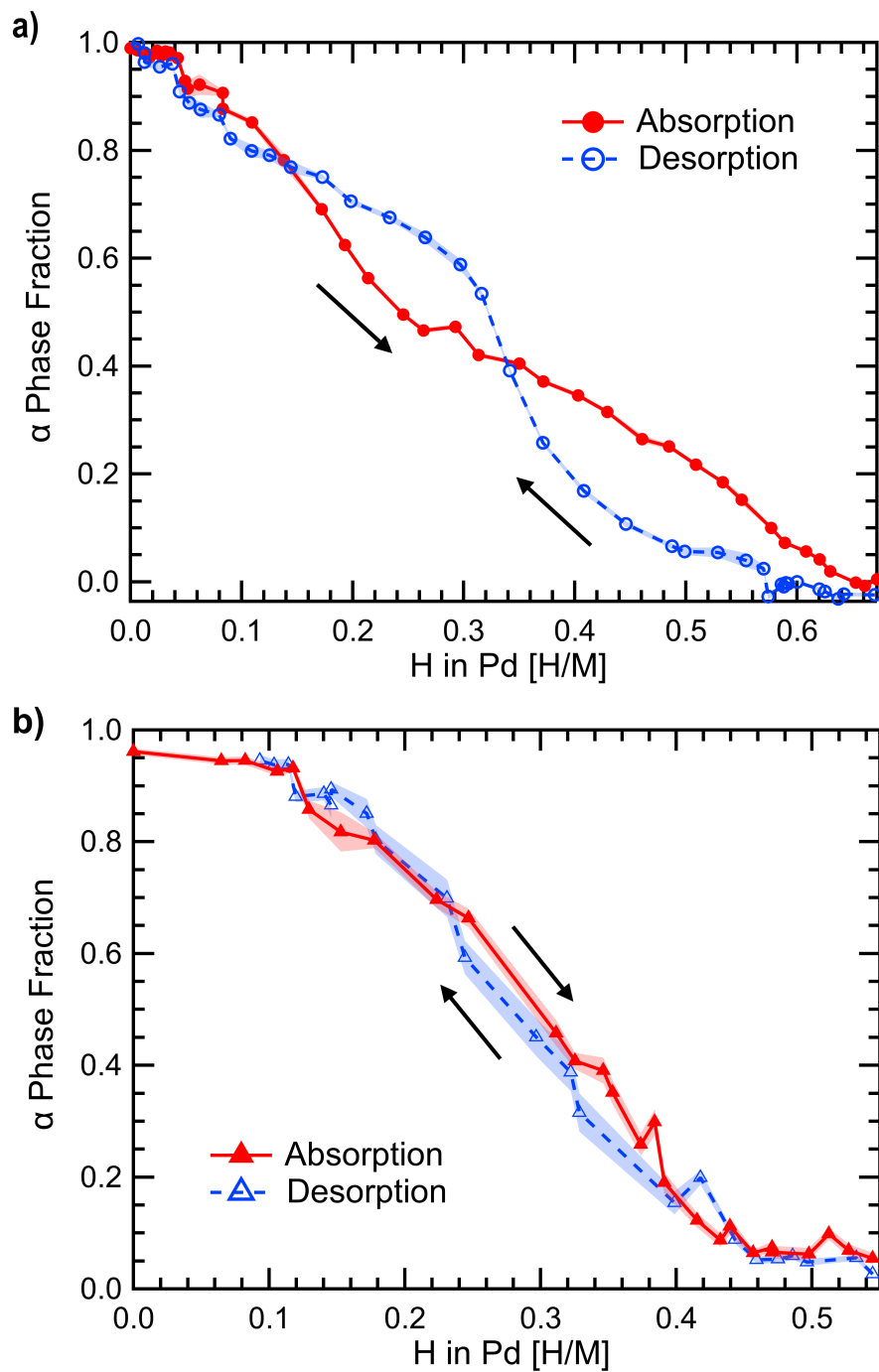


Figure 2.6: Refined  $\alpha$  phase fraction for the a) bulk and b) nanocrystalline PdH powders. The black arrows indicate the direction of transformation, and shading of the traces indicates the error bars.

Table 2.2: Variation of lattice parameter with hydrogen concentration  $da/dc$  ( $\text{\AA}/\text{H}$ ) in single phase regions. All data are fitted with a linear function according to Vegard's Law. Empty entries correspond to regions with insufficient data points to fit.

| Region                | Bulk              | Nanocrystalline   |
|-----------------------|-------------------|-------------------|
| $\alpha_{\text{abs}}$ | $0.174 \pm 0.058$ | $0.099 \pm 0.015$ |
| $\alpha_{\text{des}}$ | -                 | $0.071 \pm 0.041$ |
| $\beta_{\text{abs}}$  | $0.183 \pm 0.050$ | $0.140 \pm 0.012$ |
| $\beta_{\text{des}}$  | $0.151 \pm 0.011$ | $0.132 \pm 0.029$ |

absorption than desorption, with a significant difference for bulk Pd (Figure 2.7a).

## 2.4 Discussion

### Hysteresis of Bulk Palladium

The hysteresis and phase transformation behavior of bulk PdH indicate that a large nucleation barrier exists which is likely due to strains generated by a new phase. Our results (Table 2.1) for bulk PdH show that  $c_{\beta}^{\text{abs}} > c_{\beta}^{\text{des}}$  and  $c_{\alpha}^{\text{abs}} > c_{\alpha}^{\text{des}}$ . The shift in terminal composition to lower values on desorption is consistent with behavior predicted by Flanagan and S-K theory.[29, 31, 32] Furthermore, the abrupt transition to the plateau at the start of the (de)hydriding transition (Figure 2.3a) indicates the presence of a large nucleation barrier.

Changes in the terminal compositions affect both lattice parameter and phase fraction. A decrease in terminal composition corresponds to a reduction in lattice parameter, as seen in Figure 2.7a. During absorption,  $\bar{a}_{\beta} = 4.034\text{\AA}$ , whereas  $\bar{a}_{\beta} = 4.025\text{\AA}$  on desorption. Refined phase fractions for bulk PdH deviate from a linear behavior during initial stages of the phase transformation. During desorption, the  $\beta$  phase disappears slower than expected, whereas for absorption the  $\alpha$  phase transforms faster. In the presence of a barrier, an undersaturated  $\beta$  phase could form; rather than nucleating an  $\alpha$  precipitate, the  $\beta$  matrix continues to desorb hydrogen, retarding the transformation. Similarly, a supersaturated  $\alpha$  phase could form during hydriding. Once a  $\beta$  phase precipitate forms, it draws hydrogen from both the supersaturated  $\alpha$  phase as well as the gas phase. In this scenario, hydrogen in the supersaturated phase segregates to form additional  $\beta$  phase and a saturated  $\alpha$  phase. The nucleation barrier disappears as the transformation progresses. Refined phase fractions shift to a linear slope past the halfway point of the transformation, at a

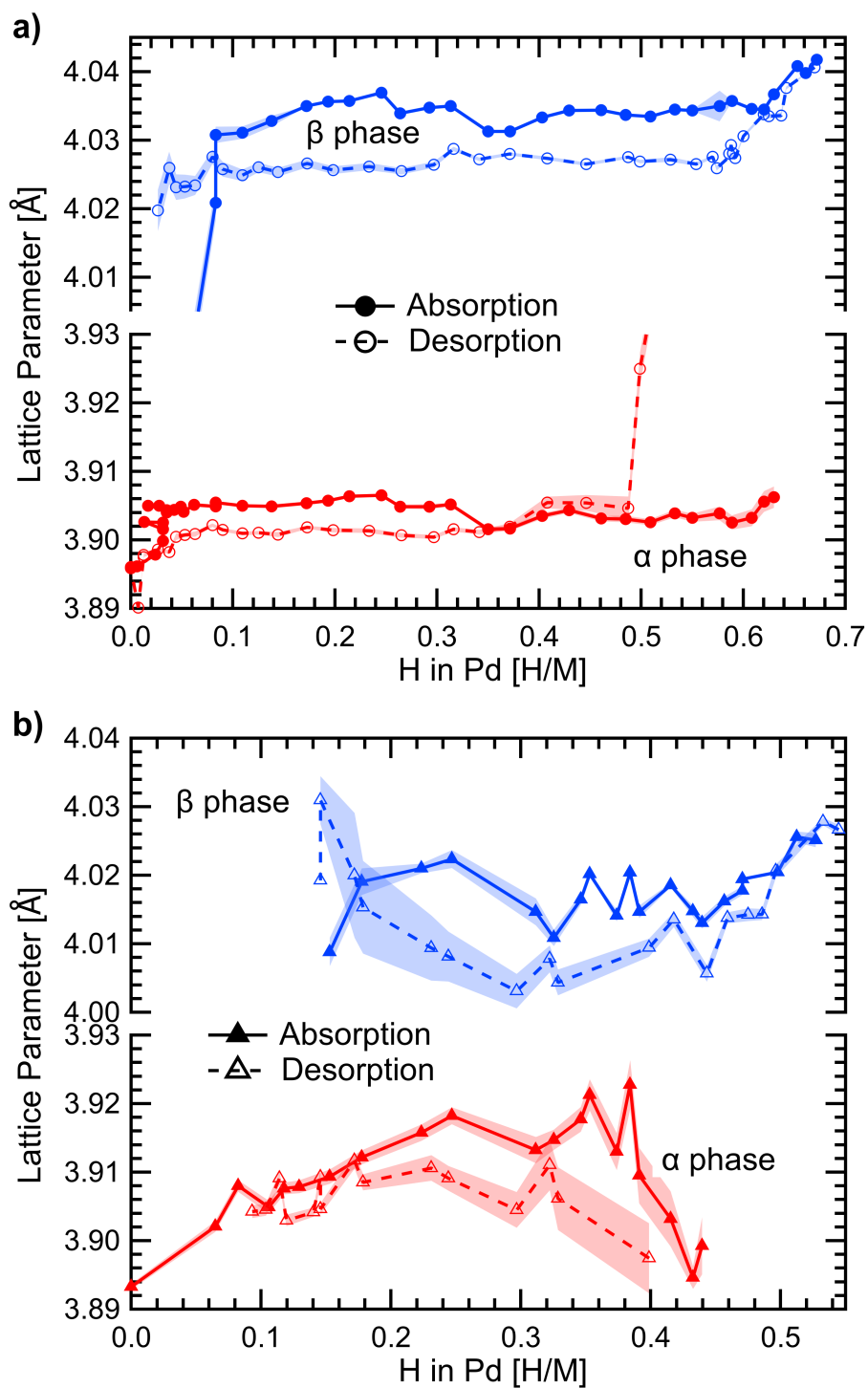


Figure 2.7: a) Refined lattice parameters of the a) bulk and b) nanocrystalline Pd powders during hydrogen absorption and desorption. The red and blue traces correspond to the solid solution  $\alpha$  phase and hydride  $\beta$  phase, respectively. Error bars are indicated by the shaded region.

hydrogen concentration at which isotherms begin to deviate from a constant-valued plateau pressure.

### Comparison of Bulk and Nanocrystalline Behavior

Nanocrystalline PdH has a smaller hysteresis, smaller total hydrogen capacity, and narrower miscibility gap than bulk PdH. A narrower miscibility gap corresponds to increased hydrogen solubility in the  $\alpha$  phase and decreased solubility in the  $\beta$  phase as seen in Figure 2.3. In Figure 2.7, we see that during absorption,  $a_\alpha$  approaches 3.92Å for nanocrystalline PdH, whereas  $\bar{a}_\alpha = 3.903\text{Å}$  for bulk PdH. Similarly,  $a_\beta$  for nanocrystalline PdH never exceeds 4.03Å, the minimum value measured during absorption in bulk PdH.

The variation of lattice parameter with hydrogen content,  $da/dc$ , is less in nanocrystalline than bulk PdH, especially for the  $\alpha$  phase. This means that the volume distortion and subsequent elastic energy contribution is less per hydrogen, allowing for increased solubility of hydrogen in the  $\alpha$  phase. It has been hypothesized that increased solubility of hydrogen in the  $\alpha$  phase and reduction in total capacity is due to a significant fraction of energetically favorable interstitial sites near the particle surface.[24, 38, 39] A high fraction of grain boundaries are visible in Figure 2.1 within the nanocrystalline Pd. Existence of energetically favorable sites or grain boundaries could provide a means for relaxation of elastic energy resulting in the reduced value of  $da/dc$  which we observe.

Phase fractions for nanocrystalline PdH are plotted in Figure 2.6b. The transformation proceeds linearly, in contrast to trends for bulk PdH. Nanocrystalline PdH isotherms do not exhibit abrupt transitions at the beginning of the plateau as in bulk PdH. Instead, the transition is more gradual (see inset in Figure 2.3), corresponding to a lower nucleation barrier. Additionally, a smaller hysteresis and a smaller difference in terminal compositions further indicate that the nucleation barrier is less for nanocrystalline than bulk PdH.

### Hysteresis and Hysteresis Energies

The S-K pressure hysteresis of Equation 1.8 is evaluated at 333 K with  $\nu_0 = 1.47 \times 10^{-29} \text{m}^3$ ,  $\sigma = 0.39$ ,  $\epsilon_0 = 0.063$ , and  $(c_\beta^{\text{coh}} - c_\alpha^{\text{coh}})$  as determined from our phase fraction data (Table 2.1).[17, 83] Shear moduli of  $G_s = 44$  and 35 GPa are used for bulk and nanocrystalline PdH, respectively.[84] S-K hysteresis values are compared to experiment in Table 2.3, and the S-K theory significantly overestimates hysteresis. Furthermore, we test the predicted temperature dependence by comparing ratios of

hysteresis at two temperatures. For bulk PdH, the measured ratio between 435 K and 333 K is 0.42, whereas the predicted ratio is 0.7. S-K theory does not quantitatively describe the thermodynamics of hysteresis.

Hydrogen absorption and desorption by PdH nanostructures has been demonstrated to occur without any plastic deformation, and the critical size below which no dislocation formation is observed is 300 nm. Hysteresis increases with particle size up to this critical size, with a maximum value of 1.41 evaluated from data reported by Ulvestad, et al.[24, 25] It is likely that the hydriding transition occurs coherently for nanoparticles below 300 nm, yet hysteresis predicted by the S-K theory is still an overestimate.

Table 2.3: Comparison of experimentally determined hysteresis values to those predicted by S-K theory. S-K hysteresis values are calculated according to Equation 1.8 with values listed in this section. Experimental hysteresis values for the 300 nm nanoparticles are determined from refs. [24] and [25].

|                             | Experiment | S-K Theory |
|-----------------------------|------------|------------|
| Bulk, 333 K                 | 0.88       | 5.2        |
| Bulk, 435 K                 | 0.37       | 3.6        |
| 7 nm nanocrystalline, 333 K | 0.37       | 2.8        |
| 300 nm nanoparticle, 300 K  | 1.41       | 2.5        |

Hysteresis energy can be expressed as the difference in chemical potential between absorption and desorption plateaus:

$$\Delta\mu_{\text{hyst}} = \frac{1}{2}k_B T \ln\left(\frac{p_{\text{abs}}}{p_{\text{des}}}\right) \quad (2.1)$$

Assuming that hysteresis is due to a macroscopic energy barrier, we can equate half the hysteresis energy to an elastic energy of the form:

$$E_{\text{el}} = \frac{1}{2}B\delta^2 \quad (2.2)$$

where  $B$  is bulk modulus (187 GPa for Pd) and  $\delta$  is a fractional change in volume.[83] For cubic crystals  $\delta$  is  $3(\Delta a/a)$ . Combining Equations 2.1 and 2.2, we estimate a misfit strain ( $\Delta a/a = |a_\beta - a_\alpha|/a_\alpha$ ) between  $\alpha$  and  $\beta$  phases and compare it to that obtained from lattice parameter data. The results are summarized in Table 2.4. Misfit strains estimated from hysteresis energies are within a factor of four of those obtained from lattice parameter measurement, indicating that hysteresis is due in large part to the existence of a macroscopic elastic energy barrier. That the estimated

value is less, however, indicates that misfit strain is mitigated in some way in both bulk and nanocrystalline PdH.

Table 2.4: Summary of hysteresis energies and measured and estimated misfit strain values for bulk and nanocrystalline PdH at 333 K. Misfit strains are estimated from hysteresis energies according to Equation 2.2.

|                               | Bulk  | Nanocrystalline |
|-------------------------------|-------|-----------------|
| $E_{hyst}[\frac{meV}{atom}]$  | 6.3   | 3.1             |
| $\epsilon_{misfit}$ measured  | 0.033 | 0.027           |
| $\epsilon_{misfit}$ estimated | 0.010 | 0.007           |

The elastic energy can depend strongly on the shape of a precipitate. For example, Nabarro calculated the energy of a misfitting ellipsoid embedded in an elastic medium, assuming the ellipsoid is incompressible and all elastic energy is in the surrounding medium.[85] This classic result showed that a sphere gives the highest energy, but this is reduced by shaping the precipitate as a thin oblate spheroid. The elastic energy per volume is reduced to zero as the precipitate becomes arbitrarily thin. Alpha-phase precipitates are observed to be shaped as thin plates, so there is a large reduction of total elastic energy compared to the case of spherical precipitates.[86] This is counteracted to some extent by surface energy. Nevertheless, we expect hydriding to proceed with a lower elastic energy barrier than for the spherical precipitates of the S-K analysis.

Other theories propose that hysteresis is due to continued formation of dislocations as hydriding transitions occur.[29] The energy of these dislocations is analogous to stored energy of cold work, or the energy released as dislocations are annealed out of cold-worked metals. In cold-worked FCC metals, stored energy is on the order of 0.1 meV/atom, far less than hysteresis energies calculated in Table 2.4.[87]

We observe in Figure 2.3a that the reduction in hysteresis of the nanocrystalline Pd is primarily due to a reduction in absorption pressure. This asymmetry in the hysteresis indicates that the mitigation of elastic energy could occur differently for absorption and desorption, adjusting the relative magnitudes of the nucleation barriers.

### Strain effects on hysteresis

Schwarz and Khachatryan's theory for hysteresis is derived from Eshelby's model for a misfitting precipitate in an infinite matrix. When the matrix becomes finite with respect to precipitate size, edge effects are important.[36] Recently, a solution

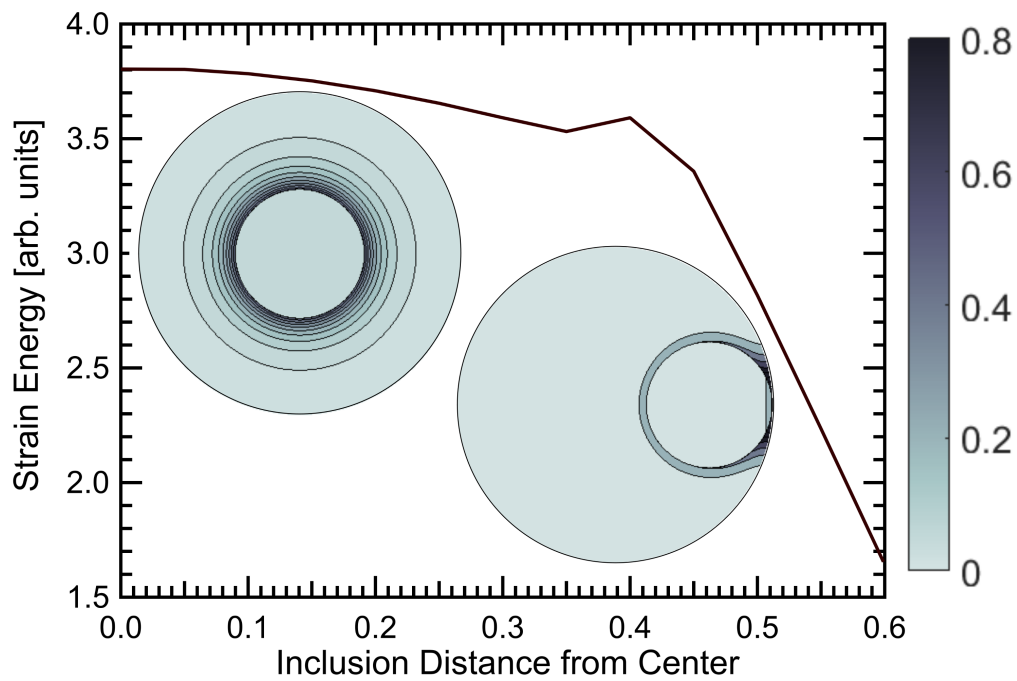


Figure 2.8: Variation of dimensionless strain energy with inclusion position. An  $0.4R$  inclusion is subjected to a uniform isotropic eigenstrain field  $\epsilon_{ij}^* = \frac{1}{2}\epsilon^*\delta_{ij}$ . Strain energy density is normalized by  $(4\mu\epsilon^{*2})/(\kappa + 1)^2$ . Inset are heat maps of strain energy density for particles with inclusions located at the origin (left) and displaced  $0.6R$  (right). The matrix boundary is constrained by traction-free conditions; displacements due to the inclusion are not shown.

to the finite Eshelby problem in two dimensions was reported for eccentrically placed circular inclusions in a circular matrix.[88, 89] We use this analysis to model effects of precipitate position within the matrix on displacement, stress, and strain energy (details in Supporting Information). The total strain energy of a precipitate of radius  $0.4R$  in a particle of radius  $R$  is plotted against precipitate center position in Figure 2.8, with inset plots of strain energy density for a centered inclusion and an inclusion displaced by  $0.6R$ . Additional plots showing for displacements and stresses are provided in Appendix A. A reduction in strain energy by more than a factor of two is achieved by shifting the precipitate to the particle edge. Further reduction of strain energy is possible by replacing the circular precipitate with a circular cap.[25]

The combined results from experiment and modeling demonstrate that accommodation of (de)hydriding stresses occurs differently in bulk and nanocrystalline PdH, altering isotherm behavior. Stresses imposed by both changing hydrogen concentration in single phase regions and by coherent nucleation of new phases are mitigated by surface effects in nanocrystalline PdH. It is likely that such surface effects could account for the smaller hysteresis of nanocrystalline PdH listed in Table 2.3. In bulk PdH, coherency stress can be reduced by precipitate shape or loss of coherency.[86] This distinction manifests as nucleation barriers with different slopes; a steep barrier for bulk and a more moderate barrier for nanocrystalline PdH. As particle size increases, so would the slope of the barrier and the hysteresis.

### **Hysteresis Effects on the Spinodal Phase Diagram**

Solvus hysteresis effects are apparent when plotting terminal compositions on the spinodal phase diagram. Figure 2.9 includes data from Table 2.1 and the literature.[30, 77] For bulk and nanocrystalline PdH, the absorption curve is shifted to the right compared to desorption. Wicke, et al., proposed that desorption is closer to true “strain-free” equilibrium, and thus should be used for the phase boundaries.[30] Our results in Figure 2.6a show that desorption in bulk PdH still exhibits a nucleation barrier and thus is not a stress-free transition. Nanocrystalline PdH has a lower nucleation barrier and hysteresis, so the shifts in terminal composition are smaller.

As a result of the splitting, the phase boundaries become directionally dependent. When hydrogen is added, the transition proceeds according to the phase boundary denoted by filled symbols in Figure 2.9, and when hydrogen is removed, the boundary shifts to that denoted by open symbols. This shift occurs even for partial isotherms,

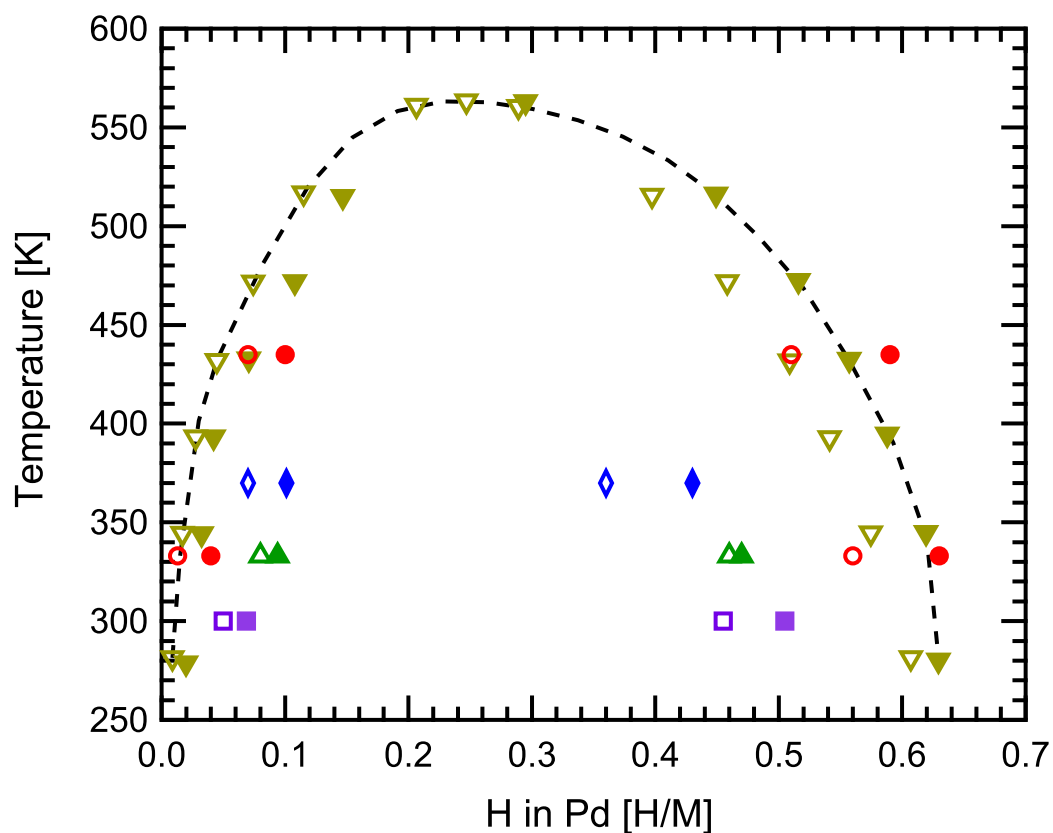


Figure 2.9: Absorption and desorption spinodal phase diagrams determined from terminal compositions of bulk and nanocrystalline PdH. Bulk and nanocrystalline PdH data from this study are plotted as circles and triangles, respectively. Additional bulk data from Wicke et al. are plotted as upside down triangles. 6 and 4 nm nanoparticle PdH data from Vogel et al. are plotted as squares and diamonds, respectively. Filled markers denote absorption, open markers denote desorption. The black line denotes a hypothetical equilibrium boundary for a barrier-free transformation.

as seen in the minor loop in Figure 2.3b. When the transformation is reversed within the two-phase region, the system shifts to the opposite isotherm branch (and associated spinodal) before any significant changes in phase fractions occur. Neither phase boundary is a chemical equilibrium boundary, but due to the existence of a nucleation barrier, they are physically relevant as coherent spinodals.

The coherent spinodal differs from the chemical spinodal owing to the elastic energy in the unmixed state. This energy is positive, suppressing the phase boundary for unmixing, and lowering the critical temperature of the coherent spinodal below that of the chemical spinodal. The unmixing boundary for nanocrystalline PdH is lower than for bulk PdH, but the elastic energy barrier of hysteresis is smaller in nanocrystalline PdH. This elastic energy barrier for the hysteresis therefore cannot be responsible for the lower critical temperature of nanocrystalline PdH. The reduction in critical temperature for nanocrystalline PdH must originate with either a different type of elastic energy in the material, or more likely in our opinion, with a change in the hydrogen-vacancy interactions.

Cahn predicted that a coherent spinodal could shift for a system in which two phases have different elastic moduli, with the direction of the shift dependent on the phase that is nucleating.[90] For anisotropic cubic materials, the elastic modulus of interest is  $Y(100) = (C_{11} + 2C_{12})(C_{11} - C_{12})/C_{11}$ . [90] This modulus is 277 and 274 GPa for bulk Pd and PdH, respectively.[91] The largest difference in modulus between the two phases is 12% for the  $C_{44}$  shear modulus, however Cahn does not quantify what difference is required for a shift. In Cahn's theory, spinodal boundaries are determined by a common tangent construction, however S-K theory states that the nucleation barrier invalidates this approach.[31, 32, 90] The splitting we observe in the PdH system may be due to a different phenomenon than Cahn predicted.

Accessing chemical spinodal boundaries requires eliminating the nucleation barrier. One method to achieve this would be to increase temperature above the critical temperature, dose with an amount of hydrogen equal to the critical concentration, and slowly cool below the spinodal. Initially, strain will be minimized as there is a small difference in terminal compositions between the  $\alpha$  and  $\beta$  phases. As temperature decreases, hydrogen is desorbed from the  $\alpha$  phase and absorbed from the  $\beta$  phase. Growth of these phases will occur without a nucleation barrier. As a result, we predict that a "strain-free" spinodal boundary will follow the desorption branch (open symbols) at low H concentrations, and the absorption branch for high H concentrations. This boundary is denoted in Figure 2.9 by the dashed black line.

## 2.5 Conclusions

We investigated pressure hysteresis associated with absorption and desorption of hydrogen by bulk and nanocrystalline Pd. Hysteresis energies were found to be comparable to elastic energies associated with lattice mismatch between  $\alpha$  and  $\beta$  phases, and significantly larger than stored energy of dislocations. Size effects are observed in several aspects of the isotherm, including hysteresis, miscibility gap, and terminal compositions of absorption and desorption. Lattice parameters and phase fractions refined from *in situ* XRD data are consistent with changes in terminal compositions. Nanocrystalline Pd has a smaller value of  $da/dc$  than the bulk, and the reduced elastic energy per added hydrogen suggests a mechanism for the increased solubility in the  $\alpha$  phase.

These experimental results indicate the existence of a nucleation barrier caused by elastic coherency strains of the misfitting nuclei. A quantitative comparison was made between the experimental hysteresis and that calculated by Schwarz-Khachaturyan theory. The theory predicted a much larger hysteresis than measured. Likewise, for the measured hysteresis, the associated elastic energy predicted a much smaller misfit strain than measured by XRD. We suggest this is caused by microstructural accommodation of the new phase by forming plate-like precipitates, reducing the coherency energy. A further reduction in elastic energy by a factor of two or more occurs for the hydriding of nanocrystalline Pd. Here, the edge effects play a big role, even for small precipitates of the new phase. The large fraction of atoms at grain boundaries in the nanocrystalline Pd could also offer interstitial site energies that are higher and lower than the bulk, causing both a slope and narrowing of the two-phase plateau of hydriding.

Additionally, the presence of a nucleation barrier splits the coherent spinodal phase boundaries, creating a directionally dependent phase diagram with the absorption boundaries greater in composition than desorption. Further work is warranted in investigating elastic energy effects on the coherent spinodal.

## HIGH CAPACITY V-BASED METAL HYDRIDE ELECTRODES FOR RECHARGEABLE BATTERIES

### 3.1 Chapter Overview

Vanadium-based body-centered (BCC) alloys are an attractive high-capacity alternative to AB<sub>5</sub>-based metal hydrides (MH) for Ni-MH batteries. Implementation of these alloys in commercial systems is hindered by the short cycle life of V-based BCC alloy electrodes due to the corrosion and dissolution of V in aqueous alkaline environments. An in-depth summary of the development of these alloys is provided in Chapter 1. In this Chapter, we investigate the corrosion behavior of V-based Ti<sub>29</sub>V<sub>62-x</sub>Ni<sub>9</sub>Cr<sub>x</sub> BCC alloy electrodes and demonstrate techniques to mitigate the corrosion. Furthermore, the performance of a novel MH-air battery utilizing V-based BCC electrodes is modeled and compared to state-of-the-art Li-ion batteries.

### 3.2 Corrosion of Vanadium in Aqueous Environments

The corrosion behavior of Ti-V-Ni-Cr quaternary alloys may be qualitatively understood by using elemental Pourbaix diagrams and experimental corrosion studies. Of these four transition metals, Ti, Ni, and Cr show passivation behavior in strong alkaline environments by forming a metal oxide or hydroxide on the surface.[92–99] Figure 3.1 shows the Pourbaix diagram of V plotted with corrected data from Post, et al.[92, 100, 101] According to the Pourbaix diagram, V corrodes and dissolves in strong alkaline solution as VO<sub>4</sub><sup>3-</sup> (vanadate) ions, which is the only stable pentavalent V species at a pH above 13.[102] Liu et al. studied the redox behavior of vanadate ions in alkaline solutions with a glassy carbon electrode and observed the reduction process of VO<sub>4</sub><sup>3-</sup> at -1.93 V versus a saturated calomel electrode, which is well outside the operational voltage window for MH electrodes.[103] This shows that corrosion-induced V dissolution is irreversible, but the rate of corrosion may be controlled by adjusting the electrochemical and chemical environment of the V-based alloy electrode. For example, Al-Kharafi et al. investigated the electrochemical behavior of V and found that the corrosion rate decreased upon removing oxygen from the alkaline solutions.[104] It should be noted that the Pourbaix diagram is a thermodynamic prediction with no information on kinetics. Furthermore, the corrosion of an alloy may differ from its elemental constituents. A systematic

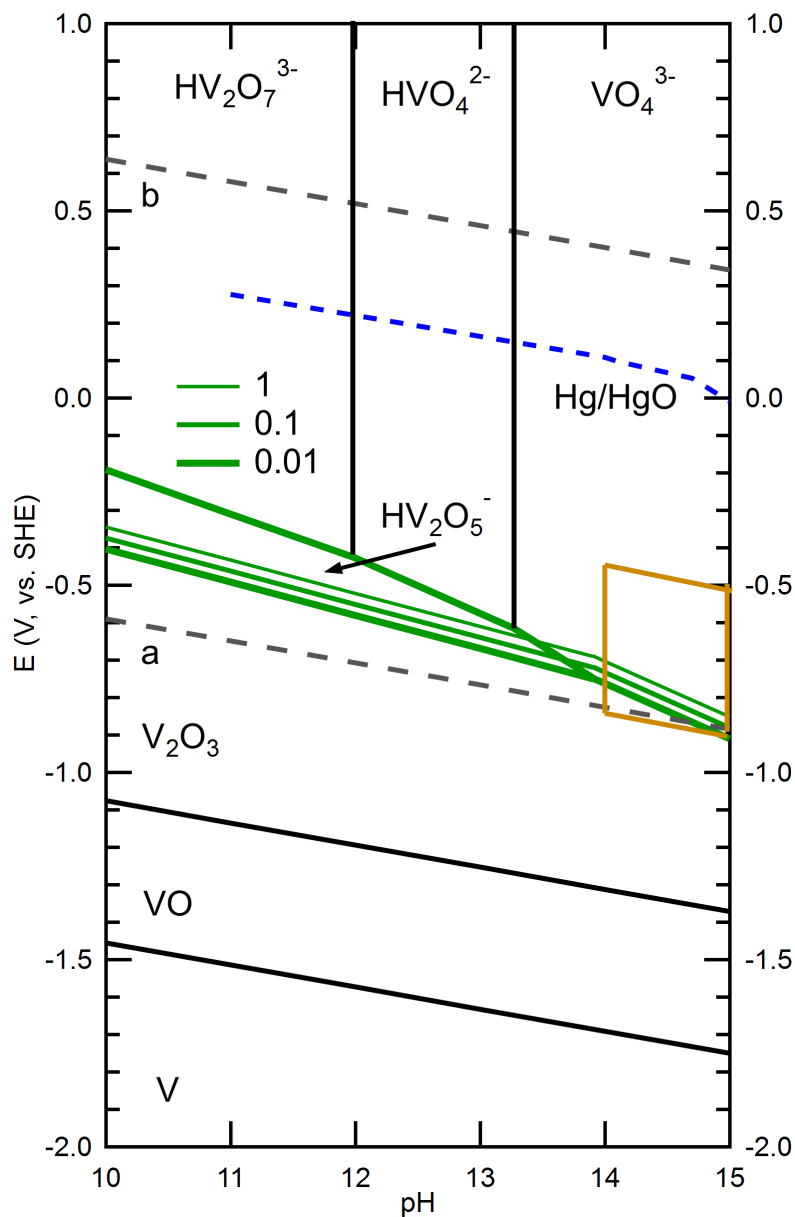


Figure 3.1: Pourbaix diagram of V with the potential of the Hg/HgO reference electrode indicated by the short-dash blue line. The orange box outlines the operational pH and potential ranges for MH batteries, and the green lines indicate how equilibrium shifts with varying concentrations of dissolved V (in units of grams V per kilogram  $\text{H}_2\text{O}$ ). Line a:  $2\text{H}^+ + 2\text{e}^- \rightarrow \text{H}_2$ ; and line b:  $2\text{H}_2\text{O} \rightarrow \text{O}_2 + 4\text{H}^+ + 4\text{e}^-$

investigation of the corrosion behavior of alloy electrodes is still appropriate.

Further improvement of  $\text{Ti}_{29}\text{V}_{62-x}\text{Ni}_9\text{Cr}_x$  alloy electrodes requires a better understanding of the phase transformations and corrosion that occurs during electrochemical hydriding/dehydriding cycles. In this work, we characterize structural changes and address corrosion by exploring the effects of pH, electrode potential, alloy composition, and the oxygen and vanadate ion concentration in the KOH electrolyte. By understanding and accounting for the limitations imposed on these electrodes by corrosion, we were able to develop an MH anode system that reversibly delivers 500 mAh/g capacity for up to 300 cycles.

### **3.3 Experimental Methods**

#### **Ti-V-Ni-Cr alloy preparation**

High purity Ti, V, Ni, and Cr metals were weighed then arc-melted under an argon atmosphere. The ingots were turned over and remelted three times to improve compositional homogeneity. The ingots were then crushed, weighed, and transferred to a Sievert's apparatus for activation. The crushed ingots were first subject to high vacuum at 653 K for several hours before the reactor was pressurized with 30 atm of high-purity hydrogen gas. The reactor was then cooled to room temperature. This process was repeated five times. After gas-phase activation, the ingots were ground in an Ar glovebox and sieved to a fine powder (200 mesh). This alloy powder was used for X-ray diffraction (XRD) analysis and electrode preparation.

#### **Isotherm measurements**

Room temperature hydrogen absorption isotherms were performed on a volumetric Sievert's type apparatus. At least 1 gram of activated alloy powder was loaded into an AISI 316L stainless steel reactor and evacuated (baseline  $10^{-5}$  Pa) at 673 K for 8 hours. The reactor was allowed to cool to room temperature before the absorption measurements were performed. For each hydriding step, equilibration was reached when the pressure in the reactor did not change for a period of 15 minutes. After equilibration, the next quantity of hydrogen was introduced into the reactor.

#### **Electrode preparation**

The alloy electrodes were prepared by pressing a mixture of alloy and Inco 525 Ni powder (1:3 mass ratio) onto an extruded Ni mesh (Dexmet Corporation) or Ni foam (MTI Corporation) current collector. Approximately 100 mg of powder mixture was hydraulically pressed onto a Ni mesh current collector with a surface area of 1.33

cm<sup>2</sup>. This high loading procedure follows those commonly adopted in literature for evaluation of the electrochemical properties of metal hydride electrodes.[105, 106] These electrodes were used to assemble air-saturated beaker cells, which were convenient for post-cycling analysis by methods such as XRD, X-ray photoelectron spectroscopy (XPS), and inductively coupled plasma mass spectrometry (ICP-MS). A smaller electrode was prepared by pressing approximately 5 mg of powder mixture onto Ni foam (0.32 cm<sup>2</sup>). This type of electrode is more suitable for cycle stability tests, because the porous nature of the Ni foam produced an electrode that was more mechanically robust.

### **Cell assembly and testing**

The electrolyte used in this study was an aqueous 30 wt% KOH solution (Alfa Aesar). For the open-air beaker cells, a Ni mesh based MH electrode was sandwiched between two sintered NiO(OH)/Ni(OH)<sub>2</sub> electrodes (4 cm<sup>2</sup> each) with nylon separators. The electrode stack was placed in a three-electrode beaker cell with Hg/HgO reference electrodes. The cell was filled with 24 mL electrolyte and let rest for at least 2 hours before testing. Coin cells were assembled in open air using Ni foam MH electrodes, 200 μL electrolyte, and NiO(OH)/Ni(OH)<sub>2</sub> positive electrodes. (See Figure B.6 and its accompanying description for the design and preparation of coin cells.) Both the beaker cells and coin cells were cycled with an Arbin multichannel potentiostat.

The Ar-purged three-electrode cells consist of a Ni foam MH anode, NiO(OH)/Ni(OH)<sub>2</sub> positive electrode (BASF-Ovonic, Rochester Hills, MI, USA), and a Hg/HgO reference electrode inside a 4-neck flask, with the necks sealed by septums. 24 mL of KOH was added, and Ar was allowed to bubble through for 30 minutes before the electrodes were lowered into the electrolyte. Cycling of the cell under continuous Ar flow was controlled by a Princeton Applied Research Versastat 4 potentiostat. All cells were charged at 100 mA/g. Two discharge protocols were used: (1) single-step discharge at 20 mA/g and (2) three-step sequential discharge at 100, 40, and 20 mA/g with a 5 minute rest period between each step. The charge capacities and cut-off voltages are specified in the text.

### **Characterization**

Polished pieces of the alloy ingot were characterized using backscattered electron imaging (BES) and energy dispersive X-ray spectroscopy (EDS) on a Zeiss 1550VP Field Emission scanning electron microscope (SEM) equipped with an Oxford X-

Max EDS system with a silicon drift detector (SDD). X-ray diffraction analysis of the alloy and electrodes was performed with a PANalytical X'Pert Pro diffractometer utilizing Cu  $K\alpha$  radiation. The alloy powder or electrode powder was ground before XRD measurements. The  $2\theta$  positions of the diffraction peaks from the electrode powders were calibrated by the diffraction peaks of the internal Ni conductive binder. X-ray photoelectron spectroscopy (XPS) was conducted on the Ni mesh electrodes before and after electrochemical experiments with a Kratos Ultra XPS. Chemical analysis of the used electrolyte was determined by an Agilent ICP-MS. The electrolyte samples for ICP-MS were collected from beaker cells and diluted with 3% nitric acid.

### 3.4 Results

#### Microstructure and thermodynamics

The microstructure and composition of three alloys ( $\text{Ti}_{29}\text{V}_{62-x}\text{Ni}_9\text{Cr}_x$ ,  $x = 0, 6,$  and  $12$ ) were characterized by XRD, SEM, and EDS (Figures 3.2 and 3.3). X-ray diffractograms of all three alloy compositions exhibit only the BCC structure (Figure 3.2). The diffraction peaks shift to higher angles with increasing Cr content, corresponding to a smaller lattice parameter for these alloys (Figure B.1). Smaller secondary peaks are also observed in the diffractograms for alloys with low Cr content, consistent with no change in crystal structure during chemical unmixing.

Backscattered electron images of polished  $\text{Ti}_{29}\text{V}_{50}\text{Ni}_9\text{Cr}_{12}$  ingots are provided in Figures 3.3a and 3.3b. These images reveal that the microstructure of the alloy is composed of a minority Ni-rich network (light) dispersed in a majority V-rich matrix (dark). The  $\text{Ti}_{29}\text{V}_{62}\text{Ni}_9$  and  $\text{Ti}_{29}\text{V}_{56}\text{Ni}_9\text{Cr}_6$  alloys show similar a microstructure (Figure B.2). The average composition of the majority and minority regions within the  $\text{Ti}_{29}\text{V}_{62-x}\text{Ni}_9\text{Cr}_x$  ( $x = 0, 6,$  and  $12$ ) alloys are listed in Table 3.1. For all three alloys, the composition of the V-rich region is close to the designed stoichiometric ratio, while the Ni-rich region contains a Ti:Ni ratio of roughly 1:1. The Ni-rich region contains little V and almost no Cr.

The microstructure of the  $\text{Ti}_{29}\text{V}_{62-x}\text{Ni}_9\text{Cr}_x$  alloys is similar to what has been reported previously.[46] The differences in the scale of the microstructure and compositional distribution are expected from the different cooling rates. These BCC alloys tend to unmix during cooling into V-rich and Ni-rich regions. The alloy as a whole is BCC, but the compositional unmixing generates regions with larger (V-rich) and smaller (Ni-rich) lattice parameters. The expected lattice parameters of

Table 3.1: Summary of the compositions of the majority V-rich and minority Ni-rich regions within the alloy ingots. The reported compositions are the average compositions as determined by EDS.

| Alloy  | V-rich region  | Ni-rich region                                      |
|--|--|---|
| $\text{Ti}_{29}\text{V}_{62}\text{Ni}_9$               | $\text{Ti}_{29}\text{V}_{65}\text{Ni}_6$               | $\text{Ti}_{47}\text{V}_8\text{Ni}_{45}$            |
| $\text{Ti}_{29}\text{V}_{56}\text{Ni}_9\text{Cr}_6$    | $\text{Ti}_{28}\text{V}_{59}\text{Ni}_6\text{Cr}_7$    | $\text{Ti}_{49}\text{V}_8\text{Ni}_{42}\text{Cr}_1$ |
| $\text{Ti}_{29}\text{V}_{50}\text{Ni}_9\text{Cr}_{12}$ | $\text{Ti}_{23}\text{V}_{57}\text{Ni}_6\text{Cr}_{14}$ | $\text{Ti}_{46}\text{V}_7\text{Ni}_{47}$            |

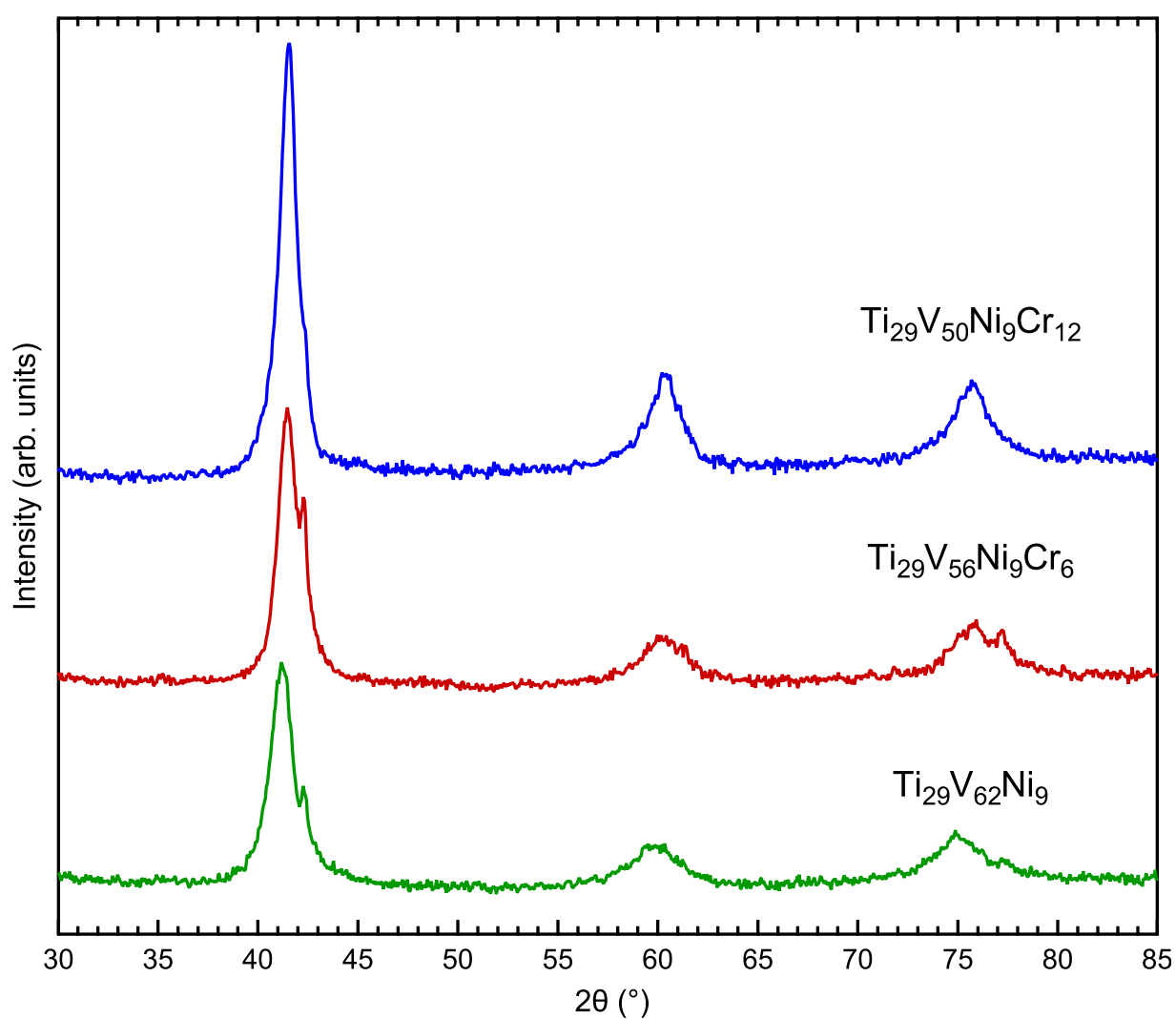


Figure 3.2: X-ray diffractograms of  $\text{Ti}_{29}\text{V}_{62-x}\text{Ni}_9\text{Cr}_x$  ( $x = 0, 6,$  and  $12$ ) alloys after hydrogen activation and pulverization of the arc melted ingots.

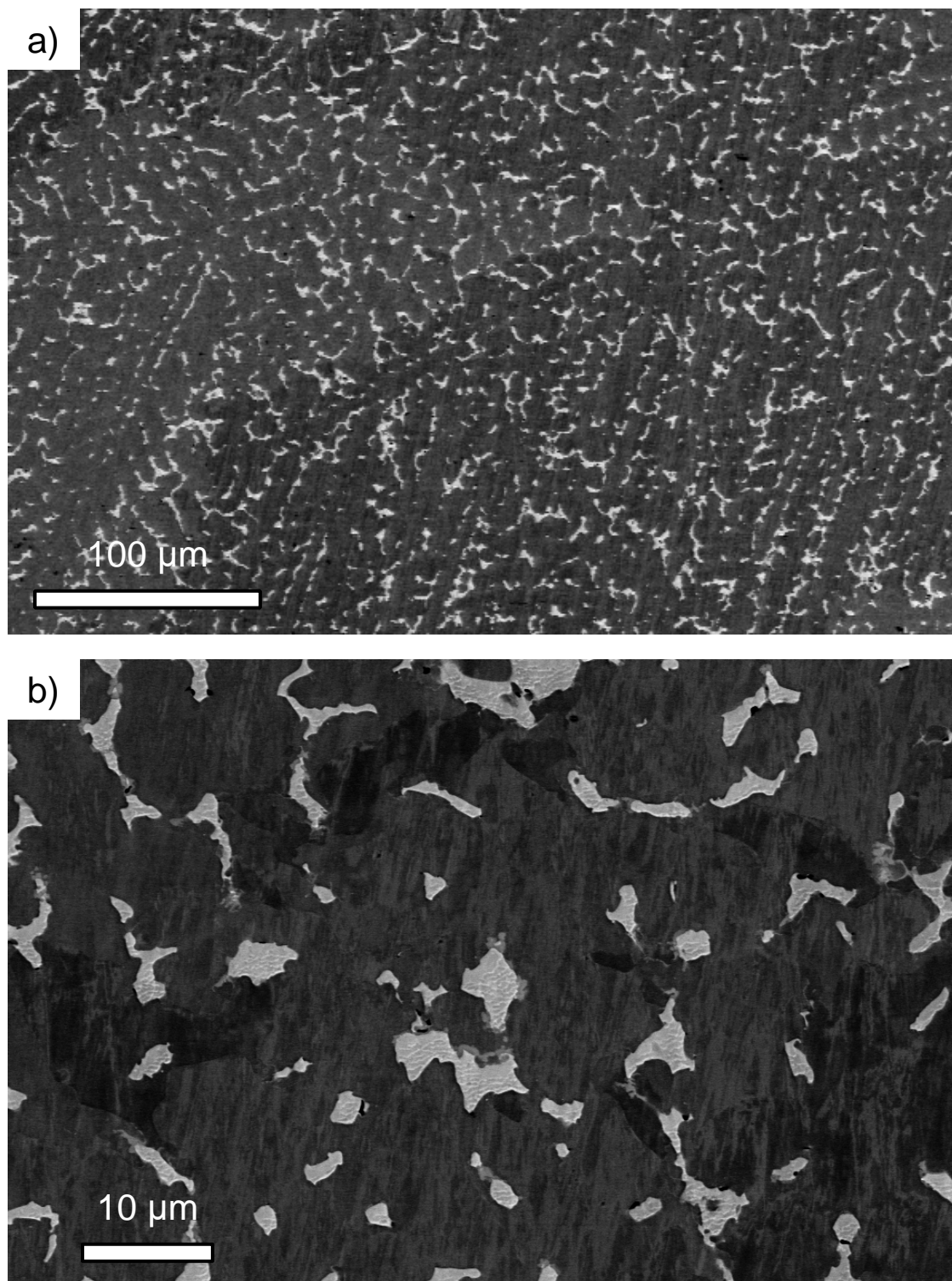


Figure 3.3: Backscattered electron images at (a) low and (b) high magnification of a polished  $\text{Ti}_{29}\text{V}_{50}\text{Ni}_9\text{Cr}_{12}$  ingot.

the two regions can account for the primary and secondary peaks visible in Figure 3.2. The composition of the Ni-rich region is relatively constant with increasing Cr concentration, while the V-rich region is not. As a result, we observe that the lattice parameter of the V-rich region decreases with increasing Cr content, shifting the peak position to the right in Figure 3.2 until it overlaps the peaks associated with the Ni-rich region.

Room temperature hydrogen absorption isotherms of the alloys are provided in Figure 3.4. The maximum hydrogen absorption capacity decreases with increasing Cr content from 3.2 mass% ( $\text{Ti}_{29}\text{V}_{62}\text{Ni}_9$ ) to 2.8 mass% ( $\text{Ti}_{29}\text{V}_{50}\text{Ni}_9\text{Cr}_{12}$ ), which translates to electrochemical capacities of 854 to 748 mAh/g. This hydrogen absorption capacity is lower than that reported by Iwakura et al., which is likely caused by difficulty in completely desorbing hydrogen from the solid solution BCC hydride phase.[47] (Note: The isotherm curves for  $\text{TiV}_{2.1}\text{Ni}_{0.3}$  reported by Iwakura, et al. show a maximum uptake of closer to 1.75 H/M (3.5 mass%), not 1.99 H/M as stated in the text.)[47]

Chromium substitution also increases the plateau pressure. In the  $\text{Ti}_{29}\text{V}_{50}\text{Ni}_9\text{Cr}_{12}$  alloy, a significant amount of hydrogen is absorbed above 1 atm of hydrogen partial pressure, indicating potential difficulties when fully charging the alloy in Ni-MH cells at ambient pressure. The addition of Cr reduces the lattice parameter and therefore the interstitial volume of the alloy, resulting in a destabilization of the hydride. A higher chemical potential is therefore required for hydride formation.

### **Electrochemical properties and characterization**

To understand the phase transformations and corrosion reactions associated with cycling these alloy electrodes, electrode and electrolyte samples at various states of charge were used for XRD, XPS and ICP-MS analysis. All samples were prepared in beaker cells in air. The cells were charged to 1200 mAh/g, or 150% of the maximum capacity estimated from the gas phase isotherm, and then discharged to -0.5 V versus Hg/HgO. The cut-off potential was chosen to include a wide potential window without oxidation of the conductive Ni binder at around -0.4 V (Figure B.3).

The charge/discharge profiles for the first cycle are plotted in Figure 3.5. The potential of the plateau during charge increases with Cr concentration, consistent with the gas phase measurement. The charge capacity approaches 800 and 710 mAh/g for the alloy electrode with 0 and 6 at.% Cr, respectively, before the hy-

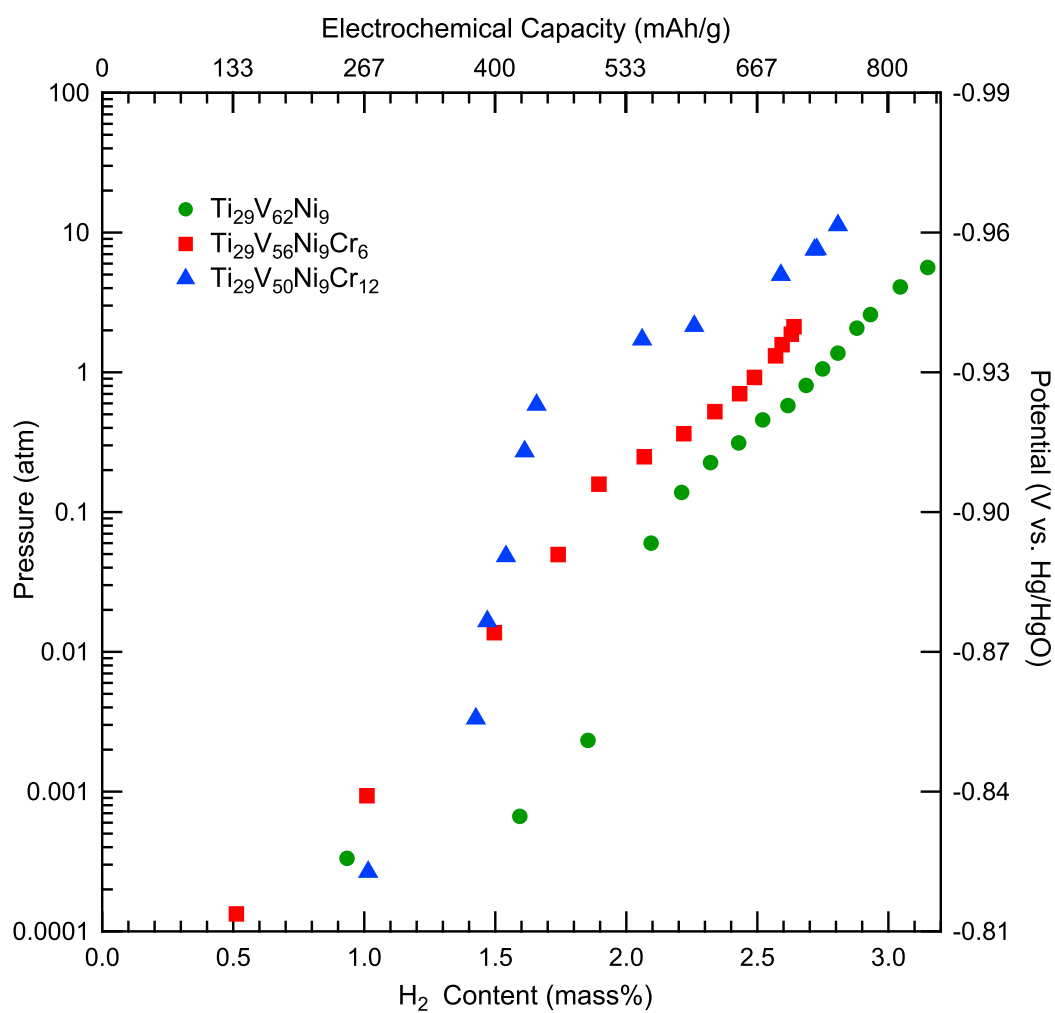


Figure 3.4: Hydrogen absorption isotherms of  $\text{Ti}_{29}\text{V}_{62-x}\text{Ni}_9\text{Cr}_x$  ( $x = 0, 6,$  and  $12$ ) alloys as measured on a Sievert's apparatus at room temperature (298 K).

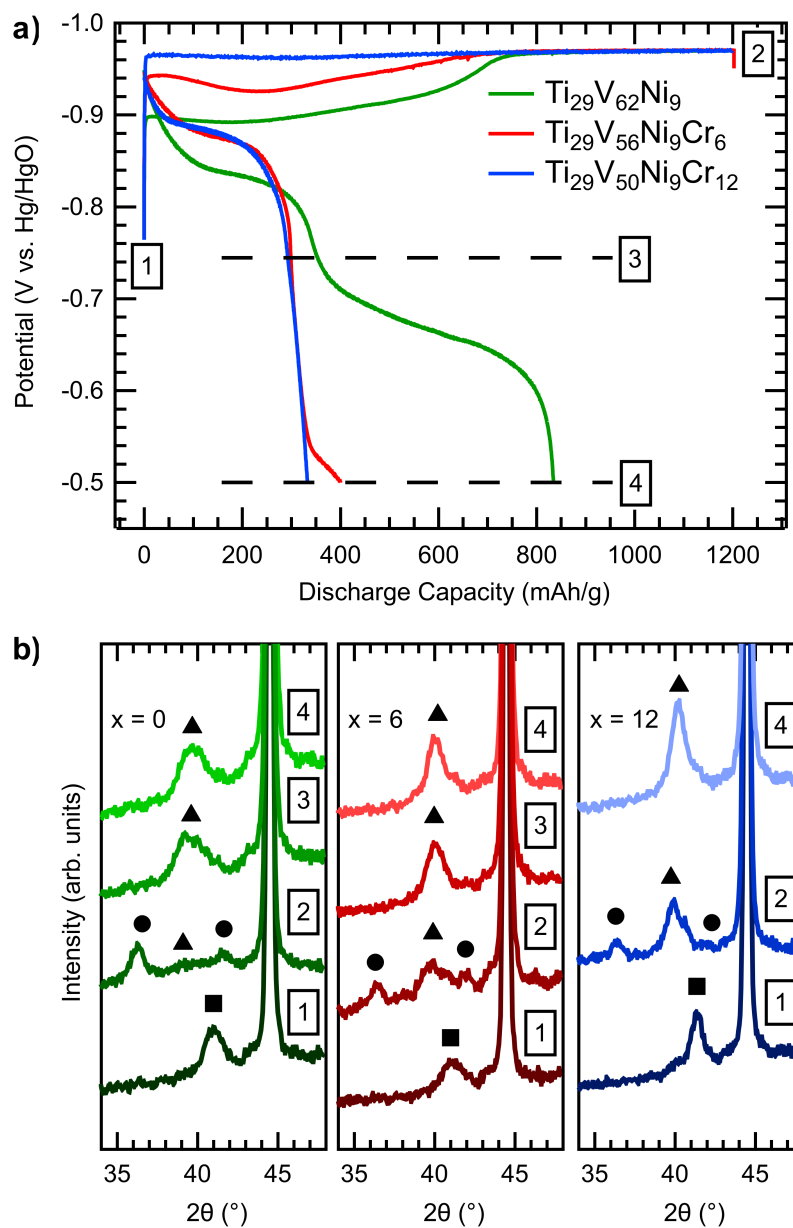


Figure 3.5: Characterization of the three alloy electrodes: (a) First cycle charge/discharge curves for the alloy electrodes in a beaker cell. *Ex situ* experiments were performed at the numbered points on the graph. (b) Diffraction patterns of the three alloy electrodes at corresponding states of charge. Hydride phases are marked with squares (BCC), triangles (BCT), and circles (FCC).

drogen over-charge potential was reached at -0.97 V. The charge potential for the alloy electrode with 12 at.% Cr reaches the over-charge potential immediately after current is applied. On discharge, the midpoint potential for the first plateau (before -0.75V) follows the trend on charge and is observed at -0.83 V for  $\text{Ti}_{29}\text{V}_{62}\text{Ni}_9$ , and -0.88 V for the  $\text{Ti}_{29}\text{V}_{56}\text{Ni}_9\text{Cr}_6$  and  $\text{Ti}_{29}\text{V}_{50}\text{Ni}_9\text{Cr}_{12}$  alloys. A second discharge plateau was observed for the  $\text{Ti}_{29}\text{V}_{62}\text{Ni}_9$  electrode starting at -0.70 V, and for the  $\text{Ti}_{29}\text{V}_{56}\text{Ni}_9\text{Cr}_6$  electrode at -0.55 V. A second discharge plateau was not observed for the  $\text{Ti}_{29}\text{V}_{50}\text{Ni}_9\text{Cr}_{12}$  electrode within the potential window. This observation seems to contradict previous studies ascribing the second discharge plateau to dehydrogenation of the monohydride phase, as Cr-substitution is expected to increase the hydrogen plateau pressure (negative shift on electrochemical scale) of both binary phase regions.[18, 52, 107] A more plausible hypothesis is continuous oxidation/dissolution of V at the second plateau, as indicated by the Pourbaix diagram (Figure 3.1). The reduction of  $\text{VO}_4^{3-}$  is irreversible over this potential range, thus the second plateau is not observed in the charging curve.[103]

Figure 3.5 shows X-ray diffractograms for the alloy electrodes collected at the corresponding states-of-charge (SoC) enumerated on Figure 3.5a. The alloys start in the BCC phase and transform to a mixture of FCC and BCT phases after charging. The FCC phase fraction decreases with increasing Cr content, consistent with less of the dihydride transition occurring below 1 atm hydrogen partial pressure (Figure 3.4). Diffraction patterns taken after the electrodes are discharged past the first potential plateau (-0.75 V for  $\text{Ti}_{29}\text{V}_{62}\text{Ni}_9$ ,  $\text{Ti}_{29}\text{V}_{56}\text{Ni}_9\text{Cr}_6$  and -0.50 V for  $\text{Ti}_{29}\text{V}_{50}\text{Ni}_9\text{Cr}_{12}$ ) contain only peaks from the BCT phase. Interestingly, the peak position of the BCT phase for all three electrodes shifts to higher  $2\theta$  angles, corresponding to a reduced lattice parameter from hydrogen desorption. The contraction of the BCT phase indicates that the discharge capacity includes hydrogen from both the  $\text{FCC} \leftrightarrow \text{BCT}$  transition and the BCT monohydride phase. A further shift of the BCT peaks occurs for the  $\text{Ti}_{29}\text{V}_{62}\text{Ni}_9$  and  $\text{Ti}_{29}\text{V}_{56}\text{Ni}_9\text{Cr}_6$  electrodes after discharge to -0.50 V. This peak shift was suspected to be caused by V dissolution, and prompted elemental analysis of the electrolyte.

Table 3.2 shows the ICP-MS results for the electrolytes collected at the SoC indicated in Figure 3.5. The results are presented as the percentage of each element (by mass) which has dissolved from the pristine alloy electrode into the electrolyte. In the case of Ni, the mass of the binder and current collector are not included in the calculation. The amounts of dissolved Ti, Ni, and Cr (for the Cr containing alloys) are very small

for all samples. The concentration of dissolved V, however, is much greater. A small amount of V dissolution is already observed after the first charge. During charging, a cathodic (reduction) current is applied to the MH electrode, indicating that V actively corrodes even when the electrode potential is the most negative. In fact, V corrodes and dissolves when the cell is in the open circuit condition. Table B.1 shows the ICP-MS results for electrolyte taken from beaker cells that were left standing for 2 days, where 6% of the total V in the  $\text{Ti}_{29}\text{V}_{62}\text{Ni}_9$  electrode has dissolved, compared to 2.47% from the  $\text{Ti}_{29}\text{V}_{50}\text{Ni}_9\text{Cr}_{12}$  electrode. The most significant V dissolution, however, is observed for  $\text{Ti}_{29}\text{V}_{62}\text{Ni}_9$  and  $\text{Ti}_{29}\text{V}_{56}\text{Ni}_9\text{Cr}_6$  alloy electrodes discharged past -0.75 V, confirming our previous hypothesis that the second potential plateau is related to continuous V oxidation into vanadate ions. The total amount of V dissolved from the electrode after one cycle is 17.75%, 5.04%, and 0.95% for the electrodes with 0, 6, and 12 at.% Cr, respectively. After 10 cycles, the Cr free electrode loses 74% of the total V content. These results also demonstrate the ability of Cr substitution to significantly suppress V corrosion and dissolution.

Table 3.2: Results from ICP-MS analysis of KOH electrolyte collected from cells containing  $\text{Ti}_{29}\text{V}_{62-x}\text{Ni}_9\text{Cr}_x$  ( $x = 0, 6, 12$ ) alloy electrodes. Electrolyte was collected from cells fully charged, discharged to -0.75 V, and discharged to -0.50 V, as indicated in Figure 3.5. Data from a cell cycled 10 times are also presented.

| Electrode state     | % Loss from electrode |       |      |      |
|---------------------|-----------------------|-------|------|------|
|                     | Ti                    | V     | Ni   | Cr   |
| $x = 0$ , charged   | 0.33                  | 1.24  | 0.7  | -    |
| $x = 0$ , -0.75 V   | 0.04                  | 2.16  | 0.01 | -    |
| $x = 0$ , -0.50 V   | 0.21                  | 17.75 | 0.09 | -    |
| $x = 6$ , charged   | 0.02                  | 1.34  | 0.18 | 0.38 |
| $x = 6$ , -0.75 V   | 0.05                  | 0.92  | 0.30 | 0.20 |
| $x = 6$ , -0.50 V   | 0.08                  | 5.04  | 0.33 | 0.19 |
| $x = 12$ , charged  | 0.04                  | 0.40  | 0.64 | 0.14 |
| $x = 12$ , -0.50 V  | 0.03                  | 0.95  | 0.15 | 0.19 |
| $x = 0$ , 10 cycles | 0.04                  | 74.03 | 0.24 | -    |

We further characterized the surface of the electrodes by XPS, and the results are presented in Figure B.4. Aside from Ti, the elemental XPS spectra for all three electrodes shift to higher oxidation states associated with oxides or hydroxides. An in-depth analysis to determine the exact oxide species is difficult due to the multicomponent nature of the alloys, as well as the broad peaks in the V and Cr

spectra. The spectra confirm, however, that surface V has oxidized to a higher oxidation state (that will dissolve into solution) as a result of deep discharge.

### **Corrosion suppression and electrochemical performance**

The Pourbaix diagram indicates that V corrosion is affected by four factors that modify the electrochemical and chemical environment of the alloy electrode: (1) electrode potential, (2) pH, (3) vanadate ion concentration, and (4) oxygen concentration near the electrode surface. From our previous analysis (see Table 3.2), it is clear that the  $\text{Ti}_{29}\text{V}_{62}\text{Ni}_9$  alloy electrodes must not be discharged past -0.75 V to avoid catastrophic V dissolution. Figure B.5 further explores controlling factors (2) and (3) in aerated KOH solution and shows no improvement in cycle stability. Compared to these strategies, Cr-substitution within the alloy improves cycle performance in aerated electrolytes, although capacity loss is still high at over 40% for 50 cycles.

Figure 3.6 plots the first three charge/discharge cycles of  $\text{Ti}_{29}\text{V}_{62}\text{Ni}_9$  and  $\text{Ti}_{29}\text{V}_{50}\text{Ni}_9\text{Cr}_{12}$  alloy electrodes in a deaerated, Ar-purged three-electrode beaker cell. The electrodes were charged to 1200 mAh/g and discharged at 20 mA/g to a cutoff potential of -0.75 V. The first charge process for both electrodes differs from that observed in the aerated electrolyte (Figure 3.5a) in that the charge capacity exceeds the estimated gas-phase capacity of 800 mAh/g before the hydrogen over-charge potential is reached. This capacity could be a result of side reactions occurring at the electrode surface, such as an oxide film that can only be reduced in deaerated electrolytes. Future studies of the surface chemistry of the alloy electrodes may provide insight into this question. The voltage profiles of the first discharge processes, however, are consistent with that seen in Figure 3.5a, and the midpoint potentials are again observed at -0.83 and -0.87 V vs. Hg/HgO for the  $\text{Ti}_{29}\text{V}_{62}\text{Ni}_9$  and  $\text{Ti}_{29}\text{V}_{50}\text{Ni}_9\text{Cr}_{12}$  electrodes, respectively. In the following two cycles, the charge and discharge potential profiles are more symmetrical, with charge capacities slightly exceeding discharge (aside from the overcharge region of the charging curve). The  $\text{Ti}_{29}\text{V}_{62}\text{Ni}_9$  electrode initially discharges 594 mAh/g capacity, which fades slightly over the next two cycles. This capacity decay process occurs in conjunction with an increasing potential hysteresis, indicating that corrosion still occurs but at a much slower rate. After an initial activation cycle, the  $\text{Ti}_{29}\text{V}_{50}\text{Ni}_9\text{Cr}_{12}$  electrode reversibly discharges 520 mAh/g, together with stable potential profiles. Compared to a previous study [46] and our preliminary data in air-saturated cells (Figure B.5), our results clearly show that a higher reversible capacity can be attained by suppressing vanadium

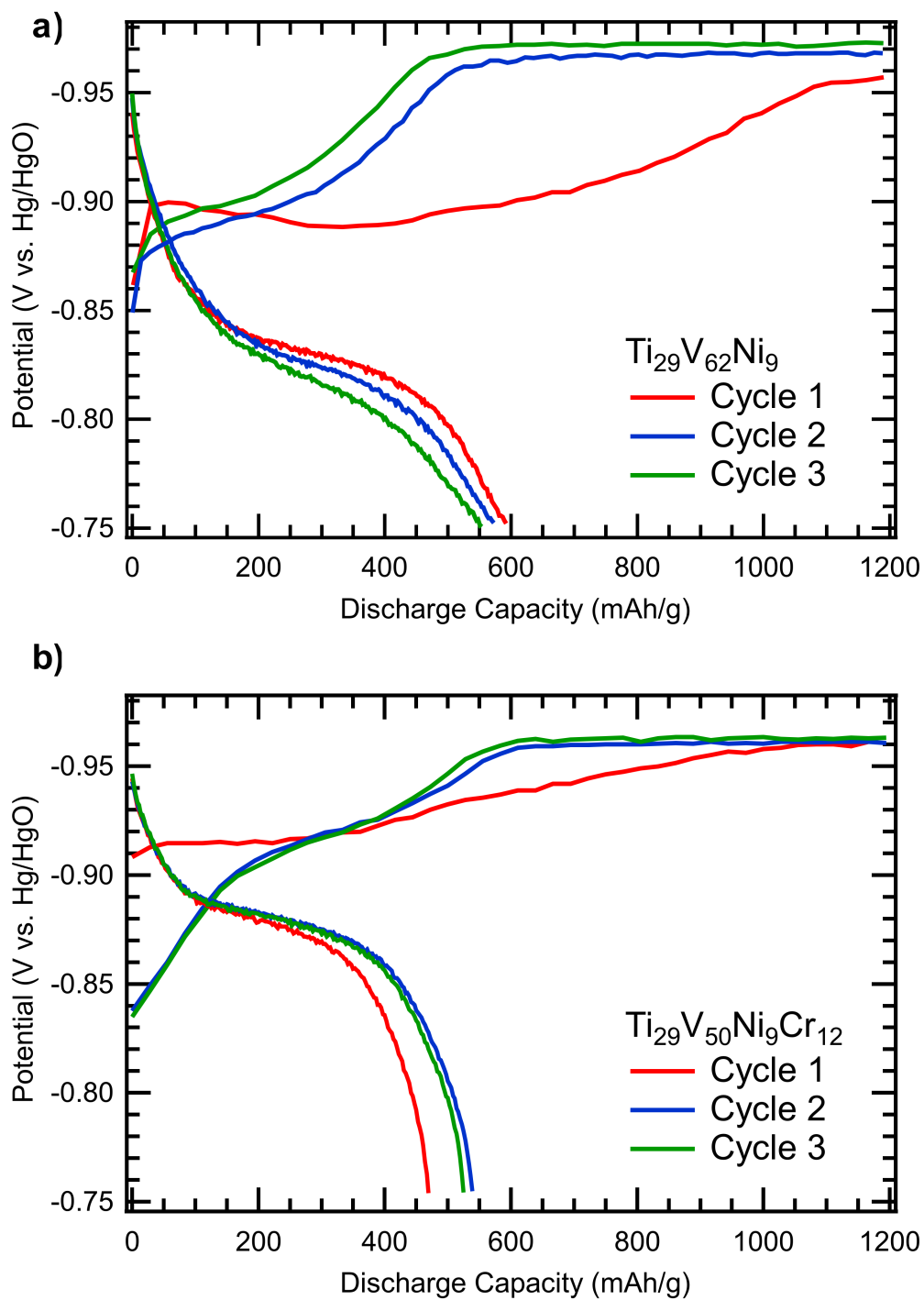


Figure 3.6: The charge/discharge curves for (a)  $\text{Ti}_{29}\text{V}_{62}\text{Ni}_9$  and (b)  $\text{Ti}_{29}\text{V}_{50}\text{Ni}_9\text{Cr}_{12}$  electrodes in an Ar-purged three-electrode cell.

corrosion by using a deaerated electrolyte.

To explore the effects of Cr and vanadate ion addition on the long-term cycling behavior of the  $\text{Ti}_{29}\text{V}_{62-x}\text{Ni}_9\text{Cr}_x$  ( $x = 0, 6, \text{ and } 12$ ) alloy electrodes in deaerated electrolyte, sealed coin cells were prepared with excess cathode material (at least 40 times the MH capacity). The cycling performance of these coin cells is presented in Figure 3.7. An abundance of cathode material is used to prevent oxygen evolution during charging and provide a relatively stable cathode potential to serve both as the counter and reference electrode. The small internal volume of the coin cell limits the amount of oxygen in the cell, even if the cell is sealed in ambient conditions (see more details of coin cell preparation in Figure B.6 and description therein). The coin cells were charged to either 550 or 400 mAh/g and discharged to 1.10 V following the three-step discharge procedure.

The effect of vanadate ion concentration was investigated by preparing KOH electrolyte with 5, 50, and 500 mM of added  $\text{KVO}_3$  for use in coin cells with  $\text{Ti}_{29}\text{V}_{62}\text{Ni}_9$  electrodes (Figure 3.7a). Compounds such as  $\text{LiVO}_3$ ,  $\text{NaVO}_3$ , and  $\text{KVO}_3$  may all be used to prepare electrolytes containing vanadate ions.[103] We selected  $\text{KVO}_3$  to avoid introducing another cation species into the KOH electrolyte. The valence state of V in both solid  $\text{KVO}_3$  and aqueous  $\text{VO}_4^{3-}$  is 5+. The  $\text{VO}_3^-$  ions in an ionic compound are polymerically linked by a single oxygen atom.[108] This ionic compound dissociates into the corresponding cations and  $\text{VO}_4^{3-}$  anions.

These cells were previously activated (not shown) by sequentially cycling 5 times each to charge capacities of 100, 300, and 500 mAh/g. This step-activation process was necessary to prevent early failure of the  $\text{Ti}_{29}\text{V}_{62}\text{Ni}_9$  electrodes (manifesting as unstable capacity in Figures 3.7b, 3.7c). Despite this, the cycle stability of  $\text{Ti}_{29}\text{V}_{62}\text{Ni}_9$  electrodes is rather poor in pure KOH electrolyte, but greatly improves with increasing vanadate ion concentration. The cell with 5 mM  $\text{KVO}_3$  in KOH electrolyte discharged 480 mAh/g maximum capacity, but began to fail after 130 cycles. The cells containing 50 mM  $\text{KVO}_3$  in KOH electrolyte performed best, discharging nearly 500 mAh/g for 200 cycles. With the addition of 500 mM  $\text{KVO}_3$ , the cycle stability is maintained, but at a lower capacity of 400 mAh/g, probably due to slower ion migration in the electrolyte. The capacity fluctuations at later cycles are likely related to the repetitive formation and disruption of the surface oxide layer during charge/discharge cycles.

We compared the proposed strategy of vanadate ion addition to that of Cr substitution in the same coin cell setup. Figure 3.7b compares the cycle stability of the

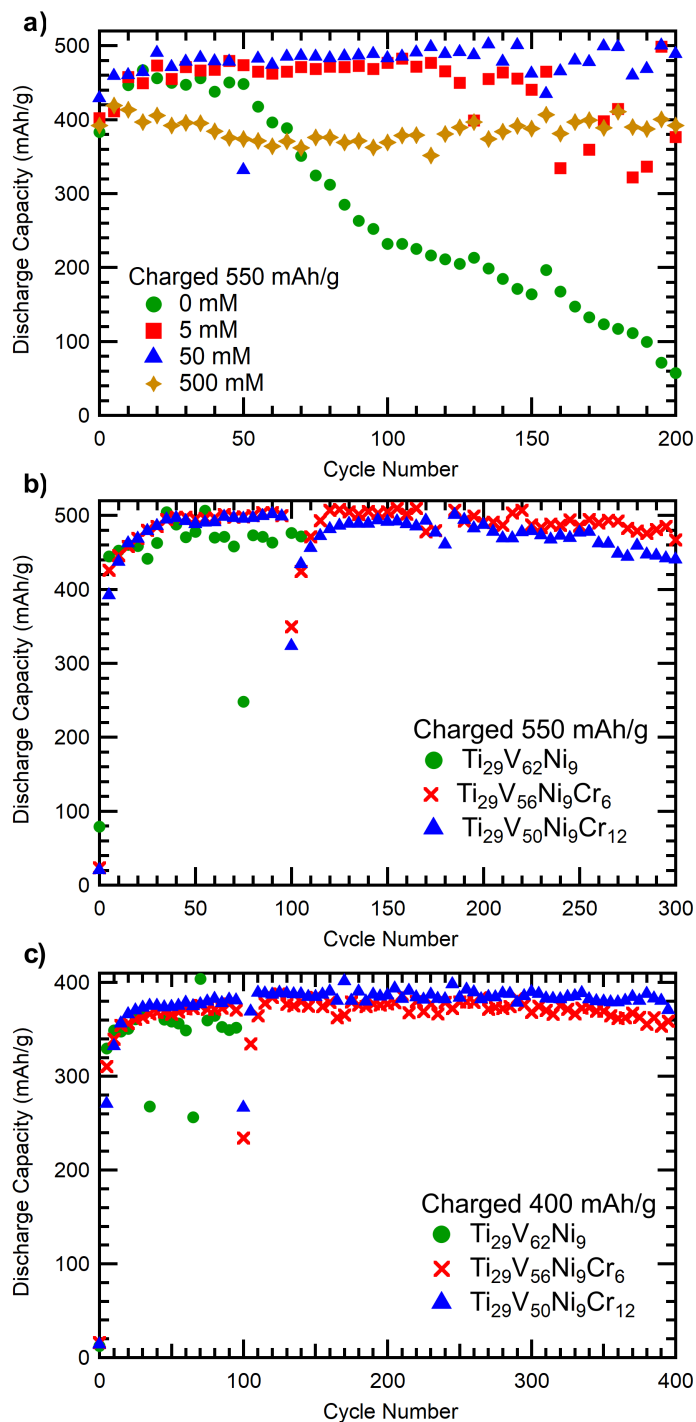


Figure 3.7: Cycling performance of coin cells containing (a)  $\text{Ti}_{29}\text{V}_{62}\text{Ni}_9$  electrodes with  $\text{KVO}_3$  additions to the KOH electrolyte and (b), (c)  $\text{Ti}_{29}\text{V}_{62-x}\text{Ni}_9\text{Cr}_x$  electrodes with KOH electrolyte. The MH electrodes were charged to 550 mAh/g in (a) and (b), and charged to 400 mAh/g in (c). In (a), cycling was interrupted after 110 cycles and restarted after two weeks for the cell containing KOH with 500 mM  $\text{KVO}_3$ . In (b) and (c), cycling was interrupted for two weeks after the 100th cycle for the  $\text{Ti}_{29}\text{V}_{56}\text{Ni}_9\text{Cr}_6$  and  $\text{Ti}_{29}\text{V}_{50}\text{Ni}_9\text{Cr}_{12}$  electrodes.

$\text{Ti}_{29}\text{V}_{62-x}\text{Ni}_9\text{Cr}_x$  ( $x = 0, 6, \text{ and } 12$ ) alloy electrodes in pure KOH electrolyte. It was found that the step-activation process used in Figure 3.7a was not necessary for the Cr-containing electrodes. The  $x = 6$  and  $12$  electrodes exhibit excellent cycle stability, delivering 500 mAh/g of capacity for 300 cycles. In some cases when cells were stopped and restarted due to rearrangement of test channels or instrument power failure during the 9 months of cycling (see Figure 3.7 caption), the capacity was recovered after a few cycles. The capacity of the  $\text{Ti}_{29}\text{V}_{62}\text{Ni}_9$  electrodes was not recovered, potentially indicating the formation of a thick passivation layer on the electrode surface. The excellent cycle stability of  $\text{Ti}_{29}\text{V}_{62-x}\text{Ni}_9\text{Cr}_x$  ( $x = 0, 6, \text{ and } 12$ ) alloy electrodes is also seen in Figure 3.7c, in which the  $x = 6$  and  $12$  electrodes were charged to 400 mAh/g and cycled stably for 400 cycles with around 95% coulombic efficiency after activation. Despite the excellent capacity retention, the voltage hysteresis and rate capability decreases with cycling (Figure B.7), indicating a growing surface oxide film.

### 3.5 Discussion

#### Extent of phase transformations

The  $\text{VH}_x$  isotherm (Figure 1.2) exhibits two distinct two-phase regions (plateaus) separated by 6 orders of magnitude in pressure.[18, 19] In contrast, the phase boundaries of the  $\text{Ti}_{29}\text{V}_{62-x}\text{Ni}_9\text{Cr}_x$  alloys are much less distinct (Figure 3.4). Sloping plateaus are common in solid solution alloys because their heterogeneous local chemistry creates a distribution of interstitial site energies for hydrogen occupancies.[18] The plateau associated with the  $\text{BCT} \leftrightarrow \text{FCC}$  phase transformation is apparent in these alloy isotherms, however it is more sloping and occurs over a smaller range of hydrogen concentration than for pure V. As a result, part of the electrochemical capacity may be accessed from the wide, sloping BCT monohydride phase region before the corresponding electrochemical potential favors oxidation.

#### Mechanisms of vanadium oxidation

To access the high capacity suggested by the gas-phase isotherms, the irreversible dissolution of V must be suppressed. The oxidation/dissolution of V in the alloy electrodes occurs by two distinct pathways, illustrated schematically in Figure 3.8. When the MH electrode is electrochemically discharged past the V dissolution potential, the corresponding cathodic reaction is the reduction of  $\text{NiO}(\text{OH})$  to  $\text{Ni}(\text{OH})_2$ , and the anodic reaction is the oxidation of  $\text{VO}_x$  to  $\text{VO}_4^{3-}$ . This process is mitigated by imposing a discharge cut-off potential more negative than the dissolution poten-

tial. In addition to this “operational oxidation,” local oxidation reactions take place internally within the MH alloy electrode regardless of the presence of a Ni(OH)<sub>2</sub> counter electrode (Figure 3.8b). In this case, the V oxidation is coupled with the following reduction reactions:



or



with Equation (3.1) strongly favored in highly alkaline media.[109] During the VO<sub>x</sub> formation in the left panel of Figure 3.8b, the oxidation state of V is less than +5. The interaction with V and the OH<sup>-</sup> in the electrolyte was proposed by Al-Kharafi, et al.[104] The heterogeneous nature of the alloy electrodes, consisting of the Ni current collector and Ni binder in addition to the Ni-rich and V-rich regions of the MH itself, likely results in a varying electrode potential across the surface. The ICP-MS results of Tables 3.2 and B.1 show that V is the only element undergoing significant corrosion, indicating that the V-rich region of the alloy is the anodic component which donates electrons to other parts of the electrode to facilitate the reduction reactions of Equations (3.1) and (3.2).

### **Corrosion suppression and capacity retention**

A combination of a low oxygen environment and either vanadate ion additions to the electrolyte or Cr substitutions to the alloy are necessary for suppressing V corrosion. Without the removal of oxygen from the electrolyte, the capacity of the electrodes in Figure B.5 begins to fade immediately. The vanadate ion additions have little effect on the cyclability of Ti<sub>29</sub>V<sub>62</sub>Ni<sub>9</sub> electrodes, whereas Cr additions do show limited improvement. Much like its role in stainless steel, Cr has been thought to form a passivating surface oxide layer on the MH which suppresses corrosion.

By itself, reducing the amount of oxygen in the system does not solve the issue of continued V oxidation. An improvement in the cyclability of the Ti<sub>29</sub>V<sub>62</sub>Ni<sub>9</sub> electrode is observed when it is cycled in the Ar purged cell (Figure 3.6) as compared to the beaker cell (Figure B.5). As shown in Figure 3.7, the capacity of coin cells with the Ti<sub>29</sub>V<sub>62</sub>Ni<sub>9</sub> electrode in pure KOH electrolyte begins to fade after 50 cycles. In this case, removing oxygen from the electrolyte forces the cathodic reaction to go from reaction (3.1) to (3.2), which may be kinetically much slower.[104, 109]

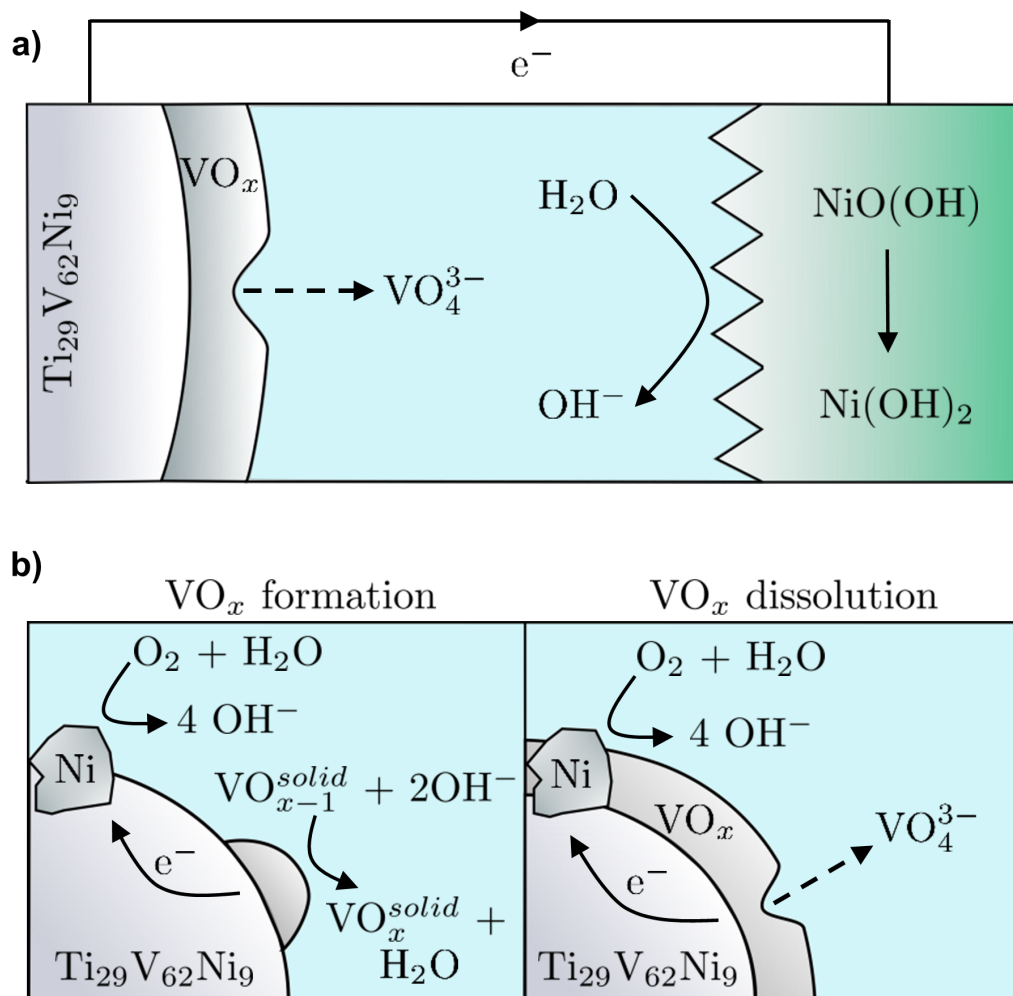


Figure 3.8: Schematics illustrating the (a) operational and (b) local oxidation that occurs for V in the  $Ti_{29}V_{62}Ni_9$  alloy electrodes.

The addition of vanadate ions to the electrolyte or substitution of Cr in the alloy suppresses V corrosion in the low oxygen environment of the coin cells. As seen in Figure 3.7a, the  $\text{Ti}_{29}\text{V}_{62}\text{Ni}_9$  electrode stably cycles at 500 mAh/g for 200 cycles with the addition of 50 mM  $\text{KVO}_3$  to the KOH electrolyte. The improvement can be explained with Le Chatelier's principle: as the concentration of the product ( $\text{VO}_4^{3-}$ ) is increased, the equilibrium shifts towards the reactants ( $\text{VO}_x$ ). The  $\text{Ti}_{29}\text{V}_{56}\text{Ni}_9\text{Cr}_6$  and  $\text{Ti}_{29}\text{V}_{50}\text{Ni}_9\text{Cr}_{12}$  electrodes cycled in coin cells exhibit excellent capacity and cycle stability of 500 mAh/g for 300 cycles (Figure 3.7b) or 400 mAh/g for 400 cycles (Figure 3.7c).

### **Integration into rechargeable batteries**

Commercial Ni-MH batteries rely on the MH electrode to reduce oxygen evolved at the  $\text{Ni}(\text{OH})_2$  positive electrode during cell over-charging. The combination of a porous separator and electrolyte-starved design facilitate this protection mechanism.[110] The optimum Cr concentration for Ti-V-Ni-Cr-based alloys to survive in this environment remains an open question. Increasing the Cr content beyond 12 at% may further improve corrosion resistance, but this will likely reduce the reversible capacity and require tailoring the alloy composition to maintain a suitable equilibrium hydrogen pressure.[67] It may also be prudent to adopt different charging protocols for Ni-MH batteries utilizing the  $\text{Ti}_{29}\text{V}_{62-x}\text{Ni}_9\text{Cr}_x$  alloy electrodes.

Alternatively, the  $\text{Ti}_{29}\text{V}_{62-x}\text{Ni}_9\text{Cr}_x$  alloy electrodes can be incorporated into an MH-air system. In an MH-air cell, an anion exchange membrane (AEM) stable in alkaline media can be used to prevent oxygen crossover.[111] Replacing the heavy  $\text{Ni}(\text{OH})_2$  electrode with an air electrode will greatly improve the energy density. We calculated the cell level energy density of a MH-air system as a function of MH electrode capacity and thickness, and the results are plotted in Figure 3.9. A description of the cell geometry and calculation details are provided in Appendix B. This is an optimistic calculation assuming the BCC electrodes are engineered to the same quality as modern  $\text{AB}_5$  MH electrodes. The shaded regions in the figure correspond to the range of energy densities for 18650 type Li-ion cells.[112, 113] With an anode capacity of 500 mAh/g, the maximum energy densities of 240 Wh/kg and 550 Wh/L are obtained with an anode thickness of 2 - 2.5 mm. The gravimetric energy density is comparable to 18650 type Li-ion cells, whereas the volumetric energy density is approximately 15% less. The discrepancy in volumetric energy density is due to the inclusion of the air channel in the 100 Wh cell volume; we expect a similar loss in volumetric energy density when the volume of cooling

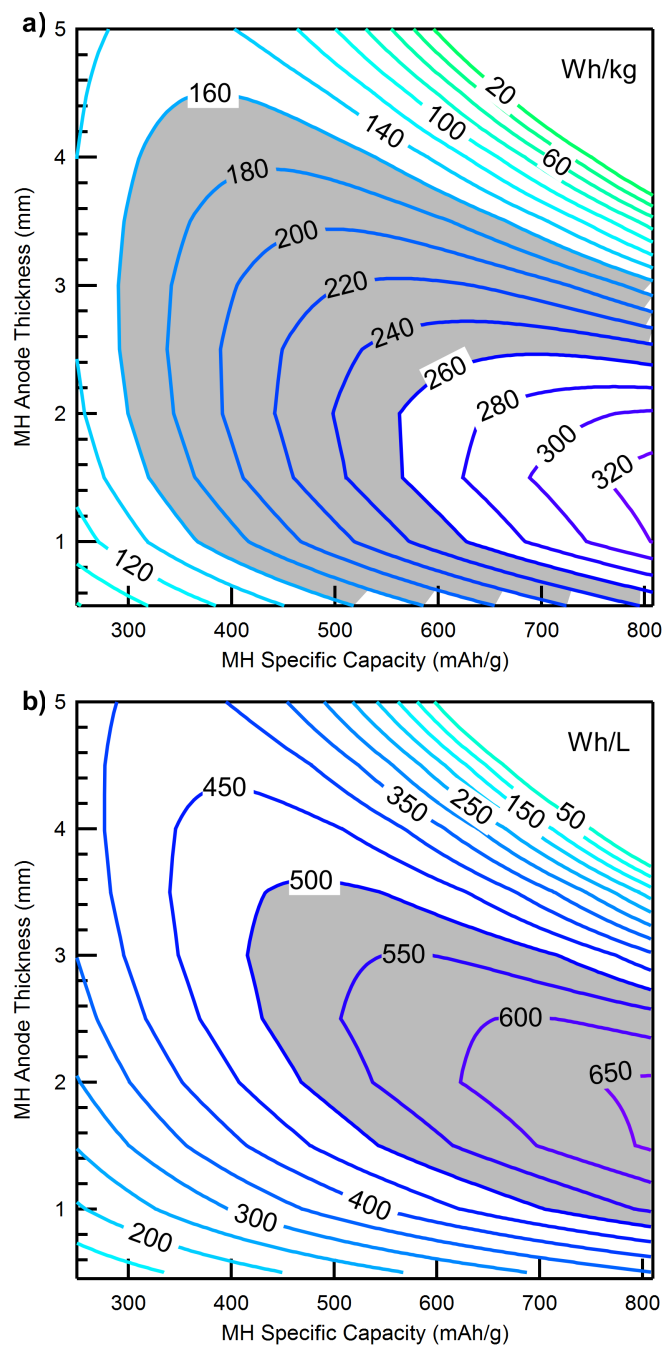


Figure 3.9: Gravimetric and volumetric energy density analysis of a MH air cell as a function of the specific capacity and thickness of the MH electrode. The shaded areas indicate the published energy density ranges for 18650 type Li-ion batteries.

channels between 18650 cells is considered.

### 3.6 Conclusions

The microstructure, hydrogen absorption, and electrochemical properties of  $\text{Ti}_{29}\text{V}_{62-x}\text{Ni}_9\text{Cr}_x$  ( $x = 0, 6$  and  $12$ ) alloy electrodes were investigated. Vanadium dissolution leads to irreversible capacity loss, which can be addressed by a combination of strategies: (1) removing oxygen from the system, (2) increasing vanadate ion concentration in the electrolyte, and (3) increasing Cr content in the alloy. Capacities as high as 594 mAh/g and 520 mAh/g for the  $\text{Ti}_{29}\text{V}_{62}\text{Ni}_9$  and  $\text{Ti}_{29}\text{V}_{50}\text{Ni}_9\text{Cr}_{12}$  alloy electrodes, respectively, were demonstrated with Ar-purged cells. Coin cells containing Cr-substituted alloy electrodes and Cr-free alloy electrodes with a vanadate ion containing electrolyte delivered around 500 mAh/g for up to 300 cycles. These V-based BCC MH electrodes achieve high capacity by accessing the monohydride phase, once V corrosion was sufficiently suppressed. This may open the door for future development of high capacity MH electrodes enabling safe and high energy density aqueous batteries.

*Chapter 4***SUMMARY AND FUTURE WORK**

The work described in this thesis covers only a few small aspects of the broad field of academic research involving metal hydrides (MH). Insights gained into thermodynamics of the hydriding transition and MH stability, however, are important to the entire MH field and beyond.

**4.1 Principles of Metal Hydride Hysteresis**

No theory in the literature completely describes the pressure and solvus hysteresis in MH. However, by comparing hysteresis energy with misfit strain energies, we show that the origin of hysteresis is a nucleation barrier resulting from coherency strain energies associated with nucleating a new phase with a different molar volume. Plastic deformation can occur during the transition, above a critical size, although the energies of dislocation formation fall short of hysteresis energies in Pd. These observations allow us to quantitatively compare experimental hysteresis values to those predicted by Schwarz and Khachaturyan, who developed a model for hysteresis based on coherency strains. Their model significantly overestimates the hysteresis. The large strains associated with hydride nucleation can be accommodated by forming energetically favorable plate-like precipitates, rather than the spherical nuclei assumed in the S-K theory. Furthermore, size effects play a role in mitigating the strain energy, as was demonstrated by a finite Eshelby model. Shifting the location of a nuclei to the edge of a particle further reduces the nucleation barrier and hysteresis in a way not available to bulk materials.

Solvus hysteresis was shown to split the coherent spinodal phase boundaries into distinct boundaries for absorption and desorption. The splitting of the boundaries results in a directional dependence of the phase diagram; phase boundaries are set by whether hydrogen is being absorbed by or desorbed from the metal lattice. Neither spinodal boundary is an "equilibrium" boundary in the sense of quasistatic reversibility, as the effects of the nucleation barrier are present during both hydrogen absorption and desorption. As a result, the split spinodals represent physically relevant phase boundaries that must both be reported when mapping out phase diagrams for MH systems. Minor loop isotherms for bulk Pd show that solvus hysteresis is present even for an incomplete transformation, providing further evidence to the ex-

istence of nucleation barriers. To the best of my knowledge, no minor loop studies have been performed for nanosized Pd. I expect that minor loops in nanocrystalline Pd would exhibit the same behavior as in bulk Pd as the nucleation barrier is still present.

Exploration of the spinodal phase boundaries is an interesting avenue for future work. As mentioned in Section 2.4, a potential method for exploring a "strain-free" spinodal boundary would involve slowly cooling the MH below the critical temperature and comparing *in situ* XRD results to those obtained during simultaneous measurement of pressure composition isotherms. Unfortunately, the critical temperature and pressure for bulk PdH is 566 K and 20 atm, experimental conditions which the *in situ* hydrogen environment chamber is not able to achieve.[21, 114] Replacing bulk Pd with nanoparticles has been demonstrated to reduce the critical temperature and pressure of the coherent spinodal, possibly to values compatible with the current experimental setup. These experiments can also provide a method for determining why the phase diagrams for bulk and nanocrystalline Pd are different. Zabel and Peisl performed *in situ* XRD experiments similar to these for the niobium-hydrogen phase diagram.[115, 116] In these studies, hydrogen was introduced to the system above  $T_c$ , and the sample was subsequently cooled below  $T_c$ . Zabel and Piesl claim that with a fast cooling rate, the sample segregates according to the incoherent spinodal, and an incoherent phase boundary can be traced.[116] Slow cooling of the NbH sample, however, resulted in a smaller miscibility gap that was attributed to the coherent spinodal boundary.[115] No comparison was made, however, to terminal compositions obtained with standard PCT measurements.

## 4.2 New Models for Hysteresis

My PdH work provides strong evidence to validate theories which attribute coherent strain energy as the origin of hysteresis. Incorporating the effect of precipitate size and location should help to make the models more accurate. However, we make no attempt at this because developing a single model which incorporates size effects and accurately predicts hysteresis in all MH systems is extremely difficult. Current theories can be divided into two categories, material-agnostic and material-specific. Material-agnostic theories, such as that proposed by Schwarz and Khachatryan, contain several assumptions or simplifications which generalize any result (see Introduction).[31, 32] In a real MH system, the assumptions will not hold up, and a match to theoretical predictions may just be coincidental. One can either develop a more robust model for a specific system with less assumptions, or various parameters

can be introduced which capture the deviations from assumptions. In either case, the model will lose generalizability.

Developing a material-specific model in conjunction with experimental data also has shortcomings. The mean field approach reported by Griessen et al. included non-linear interactions and a reasonable core-shell model for the structure of the metal hydride particle.[24] Fitting to a few datasets resulted in enthalpy values which reproduced other results not included in the fitting. However, Ulvestad and Narayan demonstrated that the core-shell model is not how the hydriding transition proceeds.[25, 37] It seems that the eccentricities of the system were subsumed into the fitting parameters and produced coincidentally correct results.

In either case, the current theories are developed enough to capture the origins of pressure and solvus hysteresis in MH. Additionally, they also provide clues to ways of mitigating hysteresis effects. The results from the study of hysteresis in PdH demonstrate the continued utility of MH as model systems for materials research.

### **4.3 Metal Hydride Electrodes**

Previous attempts in the literature to extend the cyclability of V-based BCC electrodes involved introducing corrosion-preventing elements into the alloy formulation. Improved cycling was achieved with substantial additions of Cr, however the discharge capacity is significantly reduced.[46, 67] Examining the Pourbaix diagram for V allowed us to develop alternative strategies to mitigate the corrosion that do not sacrifice capacity. Specifically, by combining electrochemical cells designed to minimize dissolved oxygen in the electrolyte with vanadate ion additions to the electrolyte or Cr substitution in the alloy, stable cycling of 500 mAh/g is achieved for up to 300 cycles. The cycle life is an order of magnitude improvement over previous studies.

In addition to strategies for improved cycling, much was learned about other aspects of V-based BCC alloy electrodes. Operational oxidation of the electrode which occurs during deep discharge (less negative than -0.75 V vs. Hg/HgO) can be mistaken for the monohydride to solid solution transition of VH. X-ray diffraction results confirmed that the pristine BCC phase is not recovered after discharge to -0.50 V, even though a voltage plateau was observed at -0.68 V vs. Hg/HgO for  $\text{Ti}_{29}\text{V}_{62}\text{Ni}_9$  electrodes. Unfortunately, this limits the reversible capacity of V-based BCC electrodes to about 500 mAh/g, or half of the theoretical capacity of 1000 mAh/g. The results of this work also demonstrate that, unlike for  $\text{AB}_5$  based Ni-

MH batteries, overcharging can prove detrimental to V-based BCC alloy electrode lifetime. If the system is overcharged in a cathode-starved configuration (i.e. excess MH is added to the anode), the oxygen evolved at the NiO(OH) cathode will corrode the BCC anode.

The corrosion mitigation strategies developed in this work provide a platform for further development of V-based BCC alloys. These alloys segregate into a V-rich hydrogen storage region and electrocatalytic Ni-rich region when cooled from the melt. If the scale of the segregation is reduced, the shortened diffusion length of hydrogen between the two phases will improve charge/discharge kinetics. Furthermore, as the electrode is cycled and the alloy particles decrepitate (break apart), some particles may lose their electrocatalytic regions and no longer contribute reversible capacity. A finer microstructure will prevent this from occurring, so long as the scale of the microstructure is less than the critical size for decrepitation. We have begun to investigate the kinetics of rapidly cooled V-based BCC alloys, which have characteristic lengths of the V-rich and Ni-rich regions reduced by a factor of 4. The rapidly cooled alloys discharge more capacity at higher discharge currents, and this trend continues with cycling.

Another avenue of further research into V-based BCC alloys is the incorporation of Fe into the alloy formulation. Developing an alloy composition with Fe will allow for the use of ferrovandium feedstock, which is much cheaper than pure V precursors.[117] The effect of Fe additions to V-based BCC alloys on gas-phase hydrogen storage has been explored, and while there is some loss in capacity, the alloys are suitable for gas-phase storage applications.[117, 118] By utilizing the strategies developed in this work to mitigate corrosion, the long-term cycling performance of cheaper, Fe-containing V-based BCC alloys can be properly evaluated.

#### **4.4 Outlook**

Although the metal hydride systems presented in this thesis differ in their complexity and applicability, understanding the processes that contribute to their inefficiencies requires an in-depth knowledge of the underlying thermodynamics. Providing experimental confirmation of theoretical models will help future researchers better understand the phenomenon of hysteresis, and the identification of strategies to reduce corrosion in metal hydride battery electrodes will lead to the development of stable, high capacity metal hydride batteries.

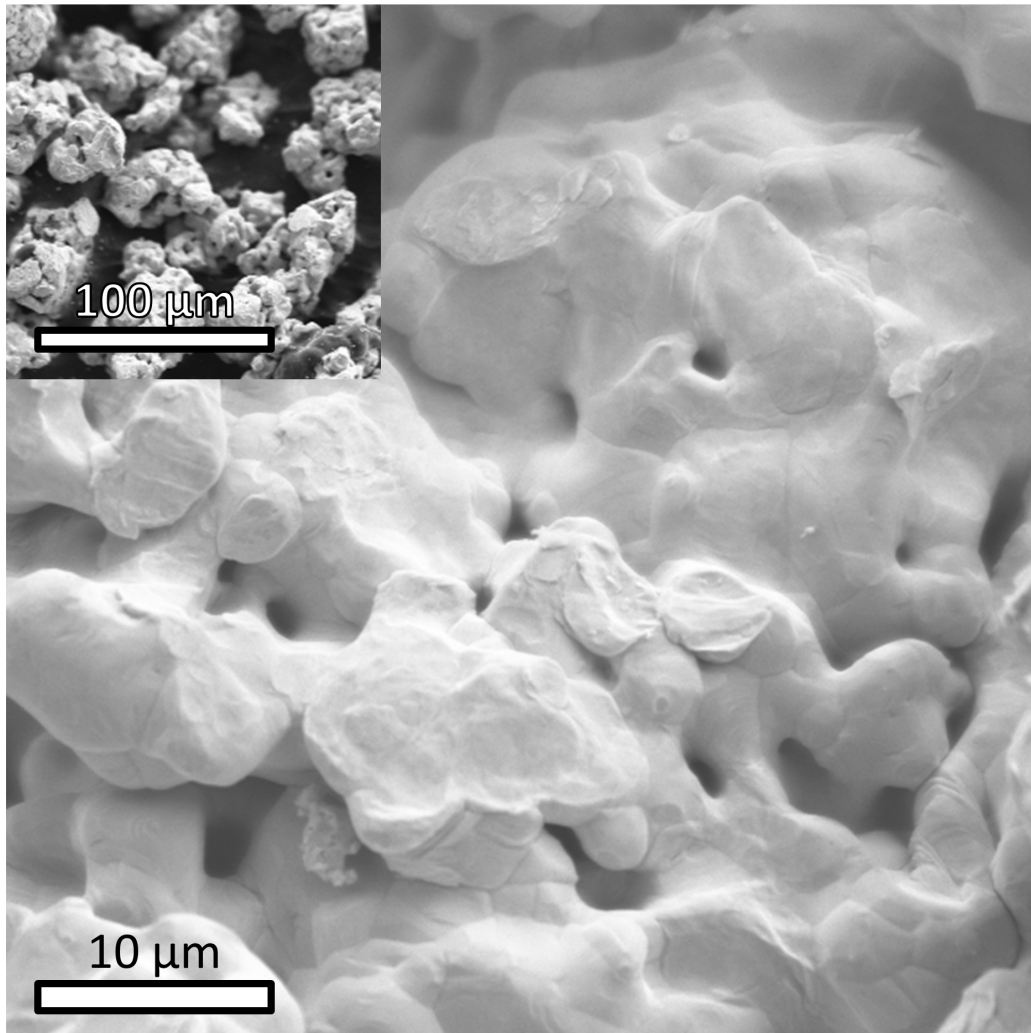
*Appendix A***SUPPLEMENTARY INFORMATION FOR ELASTIC ENERGY  
AND THE HYSTERESIS OF PHASE TRANSFORMATIONS IN  
PALLADIUM HYDRIDE**

Figure A.1: Scanning electron micrograph of a bulk Pd particle consisting of coalesced grains. The inset shows the scale of individual particles.

### **A.1 Pressure composition isotherm measurements in Sievert's apparatus and *in situ* hydrogen environment chamber**

Pressure composition isotherms were measured during the *in situ* x-ray diffraction studies for bulk and nanocrystalline Pd samples. Figure A.2 below compares the *in situ* and Sievert's pressure composition isotherms measured for bulk (a) and nanocrystalline (b) Pd. For both samples, the plateau pressures for absorption and desorption are slightly greater in the *in situ* setup than those measured for with the Sievert's apparatus. Hysteresis values, however, are equivalent between the two measurements. We attribute these differences to temperature differences between the apparatus; the difference in pressure corresponds to a temperature difference of approximately 5° C.

### **A.2 Two-Dimensional finite Eshelby model for an eccentric circular inclusion in a circular domain**

Eshelby solved the problem of a misfitting elastic inclusion in an infinite three-dimensional elastic matrix. It was further demonstrated that stress and strain fields within an elliptic or ellipsoidal inclusion are uniform, providing for an equilibrium inclusion shape. Schwarz and Khachaturyan used the results of the classical Eshelby problem to calculate the coherency stresses associated with nucleation of a hydride (solid solution) phase inside an infinite solid solution (matrix). These stresses were used in developing an expression for pressure hysteresis.[31, 32]

For hysteresis in nanoparticles, the assumption of an infinite matrix is no longer valid. Image forces and edge effects are thought to play a large role in accommodating coherency stresses associated with a phase transformation. As such, stresses and strains in both the inclusion and matrix should vary with position of the inclusion for a finite matrix.

To test this hypothesis, we adapted the results of Zou et al., which solve the problem (in two-dimensions) of an eccentrically placed circular inclusion in a circular matrix.[88, 89] Working in two dimensions ( $x, y$ ) allows for use of the complex variable ( $z = x + iy$ ) method with arbitrary analytic Kolosov-Muskhelishvili potentials  $\gamma$  and  $\psi$ . These potentials (and their derivatives with respect to  $z$ ) can be used to express displacement, stress, and strain energy densities associated with an inclusion in a matrix.

We assume the matrix and inclusion are both homogeneous and isotropic. A uniform isotropic eigenstrain  $\epsilon_{ij} = 0.5\epsilon\delta_{ij}$  is applied to the inclusion. The displacements  $u_i$

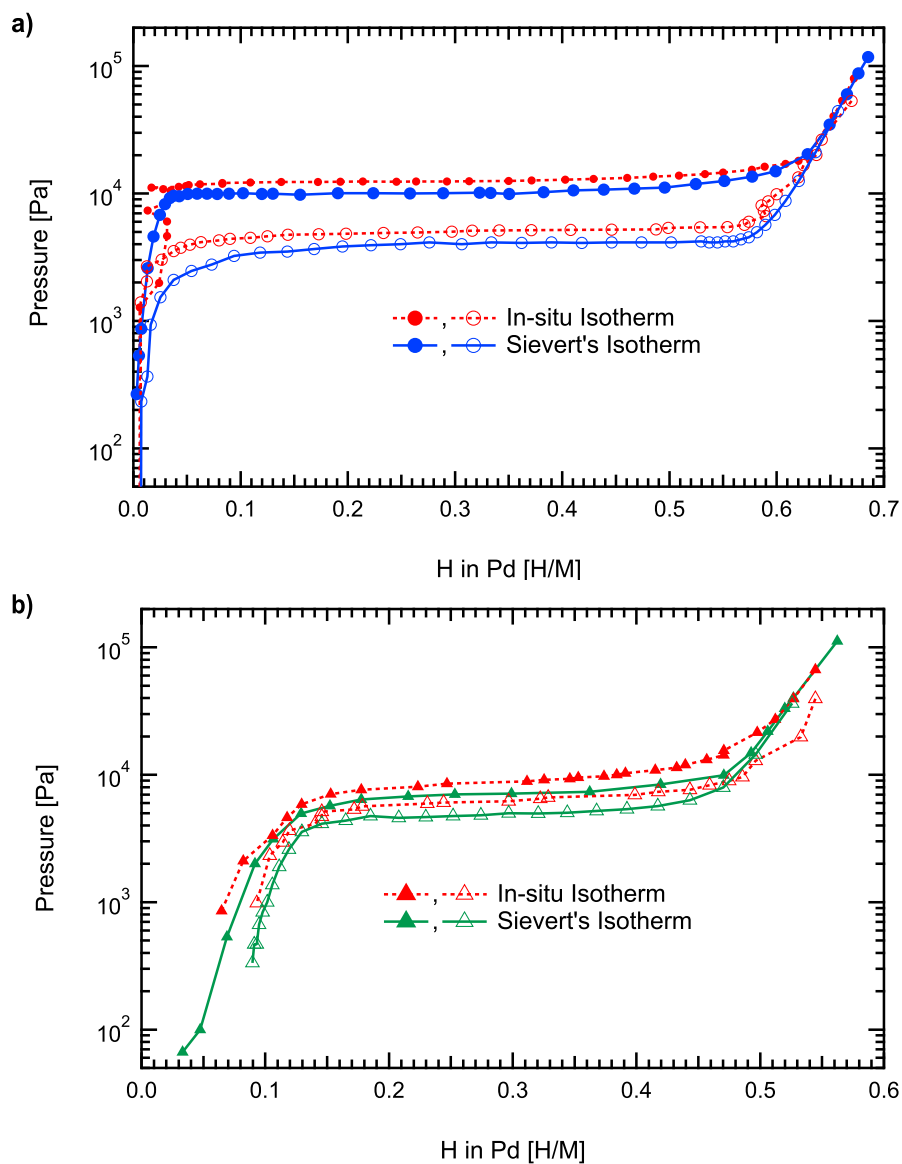


Figure A.2: Comparison of pressure composition isotherms measured in a Sievert's apparatus and *in situ* hydrogen environment chamber. Isotherms for bulk Pd are plotted in a) and for nanocrystalline Pd in b), both at 333K.

and stresses  $\sigma_{ij}$  are evaluated with Equations (65) – (67) in Reference [88], and the strain energy density is adapted from Equation (A.8) in Reference [89]. They are reproduced here:

$$\begin{aligned} \frac{u_1 + iu_2}{4r\epsilon^*/(\kappa + 1)} &= \frac{r}{4(\bar{z} - \bar{h})} - \frac{1}{8} \left[ \frac{(\kappa - 1)z - 2h}{r} + \frac{2r}{\bar{z} - \bar{h}} \right] \chi^\omega \\ &+ \frac{R^2rz + rh(h\bar{z} - 2R^2)}{4\eta(R^2 - h\bar{z})^2} - \frac{\kappa rz}{4\eta(R^2 - h\bar{z})} \\ &- \frac{(\kappa - 1)rz}{4\eta(\eta - 1)R^2} + \frac{rh}{2\eta R^2} \end{aligned} \quad (\text{A.1})$$

$$\frac{\sigma_{11} + \sigma_{22}}{8\mu\epsilon^*/(\kappa + 1)} = -\frac{1}{2}\chi^\omega - \frac{R^2r^2}{\eta} \text{Re} \left[ \frac{1}{(R^2 - h\bar{z})^2} \right] - \frac{r^2}{\eta(\eta - 1)R^2} \quad (\text{A.2})$$

$$\frac{\sigma_{22} - \sigma_{11} + 2i\sigma_{12}}{8\mu\epsilon^*/(\kappa + 1)} = \frac{r^2(1 - \chi^\omega)}{2(z - h)^2} + \frac{r^2\bar{h}3R^2\bar{h} - 2R^2\bar{z} - \bar{h}^2z}{2\eta(R^2 - h\bar{z})^3} \quad (\text{A.3})$$

$$\frac{\nu\epsilon}{4\mu\epsilon^*/(\kappa + 1)^2} = \left[ (\kappa - 1)(\text{A.2})^2 + 2(\text{A.3})(\overline{\text{A.3}}) \right] \quad (\text{A.4})$$

For these equations,  $R$  is the domain radius,  $r$  the inclusion radius,  $h$  the complex coordinates  $x + iy$  of the inclusion center,  $\mu$  the shear modulus, and  $\chi^\omega$  is either 1 or 0 if a point  $z = x + iy$  is interior or exterior to the inclusion, respectively. The case of plane stress or plane strain is set by  $\kappa = \kappa(\nu)$ , with Poisson's ratio  $\nu$ , and  $\eta$  defines the boundary conditions. For  $\eta = \kappa$ , we have the displacement-free Dirichlet case, and for  $\eta = -1$  the traction-free Neumann case. Solutions for individual displacement or stress components are obtained by linear combination of real and imaginary components of the above equations.

All four equations are incorporated into a custom MATLAB code to solve for displacement, stress, and strain energy density given Poisson's ratio and inclusion radius and origin as inputs. The MATLAB code was evaluated for correctness by reproducing results from Zou, et al., (see below) who solved for an inclusion with  $\nu = 0.3$ ,  $r = 0.3R$ , and  $h = 0.5R$ . A traction-free boundary condition  $\eta = -1$  was imposed and the plane strain case  $\kappa = 3 - 4\nu$  considered.

The MATLAB procedure was then used to evaluate the variation of strain energy with inclusion position for a finite matrix. In this case, the Poisson ratio is set to 0.39, the value reported for Pd. As before, a traction-free boundary condition  $\eta = -1$

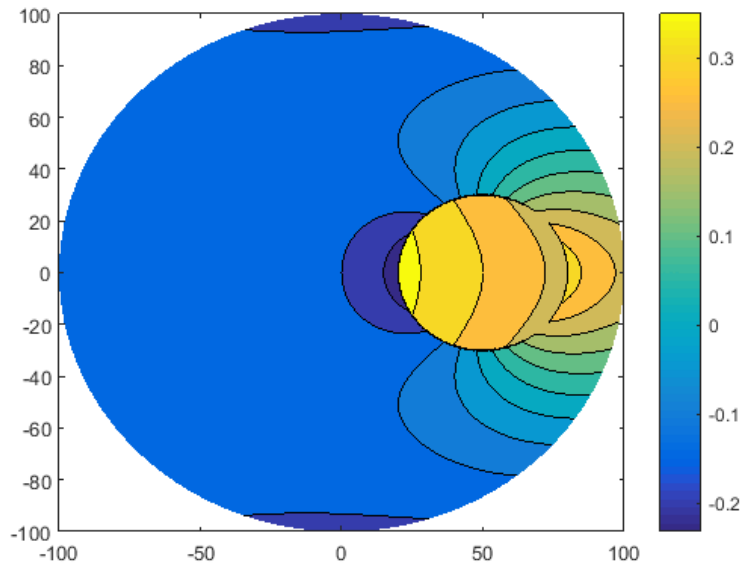


Figure A.3: Displacement field  $u_1$  for the case published by Zou. Displacement is normalized by  $(1 - \nu)/r\epsilon^*$  to be unitless.

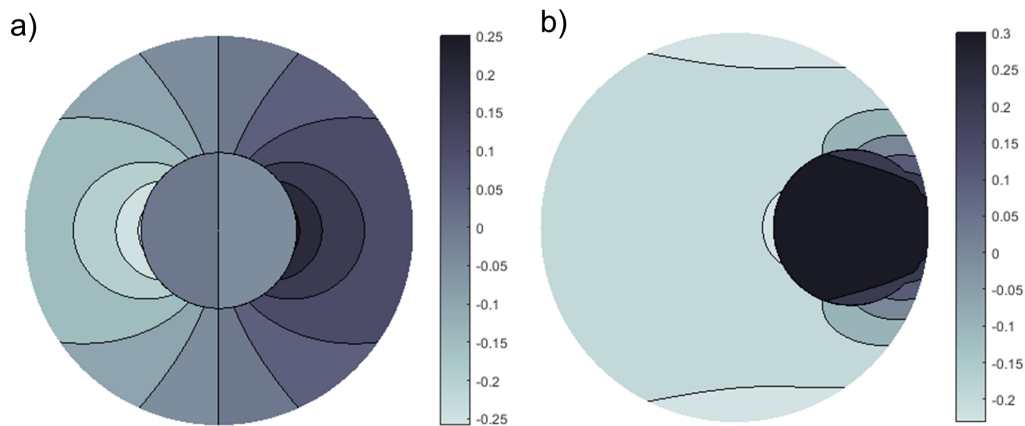


Figure A.4: Displacement fields  $u_1$  for  $0.4r$  inclusions located a) at the center and b) displaced to the edge of the domain. Displacement is normalized by  $(4r\epsilon^*)/(\kappa + 1)$  to be unitless.

was imposed to allow for surface relaxation and the plane strain case  $\kappa = 3 - 4\nu$  considered. The position of an  $0.4R$  diameter inclusion was varied from the center to the edge in 13 steps spaced  $0.05R$  apart along the x-axis, and the total strain energy was calculated at each position. These results are summarized in Figure 2.8. Displacement and stress components were also computed and are included here for the case of the centered and edge inclusions.

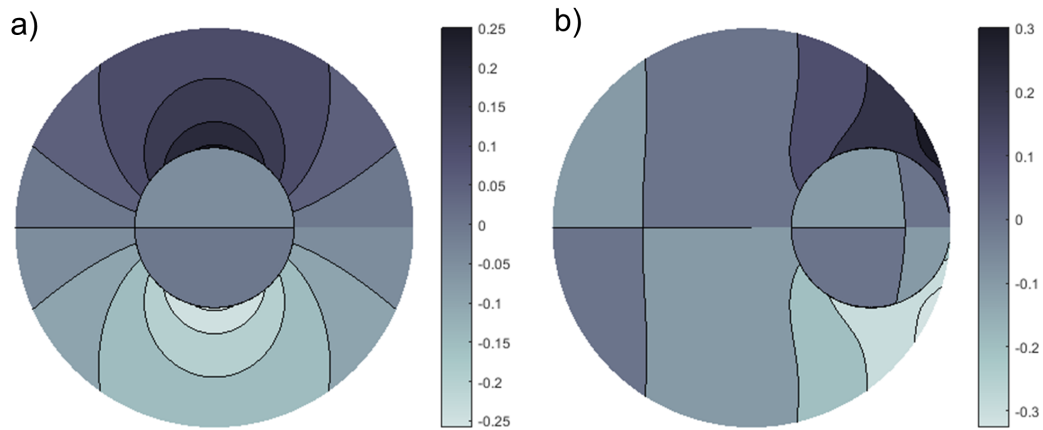


Figure A.5: Displacement fields  $u_2$  for  $0.4r$  inclusions located a) at the center and b) displaced to the edge of the domain. Displacement is normalized by  $(4r\epsilon^*)/(\kappa + 1)$  to be unitless.

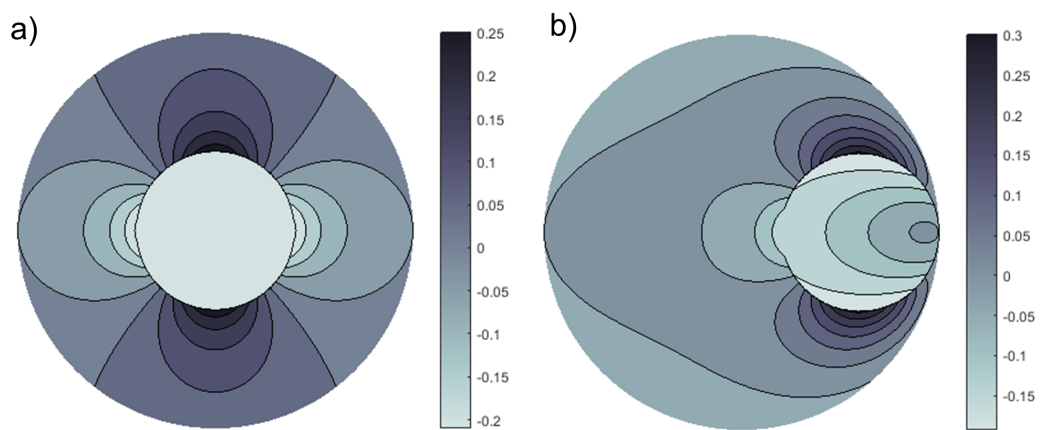


Figure A.6: Stress fields  $\sigma_{11}$  for  $0.4r$  inclusions located a) at the center and b) displaced to the edge of the domain. Stresses are normalized by  $(4\mu\epsilon^*)/(\kappa + 1)^2$  to be unitless.

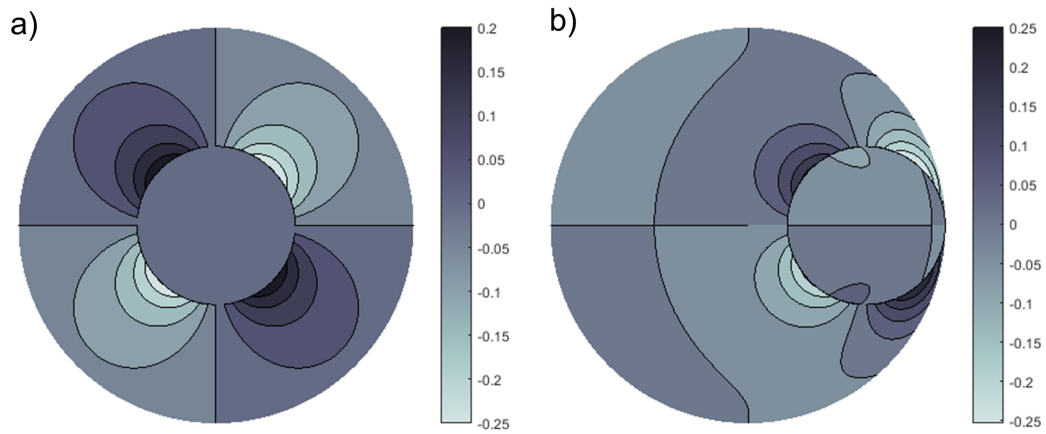


Figure A.7: Stress fields  $\sigma_{12}$  for  $0.4r$  inclusions located a) at the center and b) displaced to the edge of the domain. Stresses are normalized by  $(4\mu\epsilon^*)/(\kappa + 1)^2$  to be unitless.

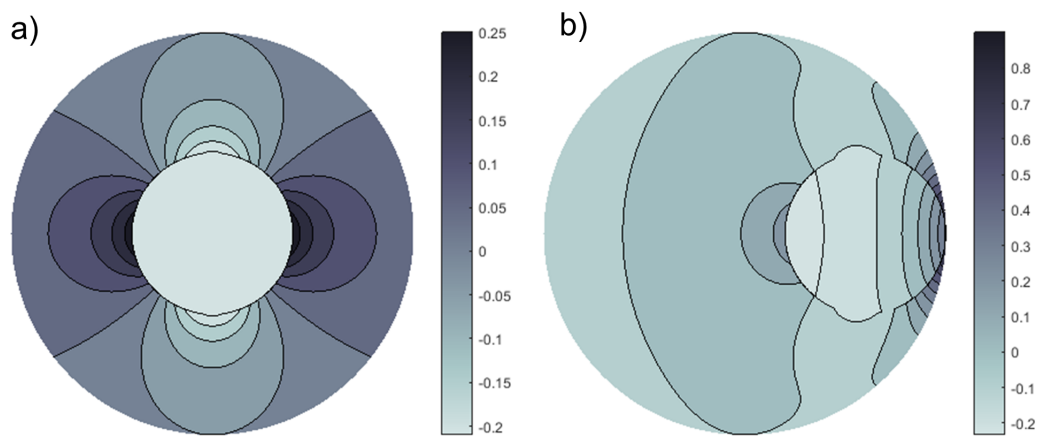


Figure A.8: Stress fields  $\sigma_{22}$  for  $0.4r$  inclusions located a) at the center and b) displaced to the edge of the domain. Stresses are normalized by  $(4\mu\epsilon^*)/(\kappa + 1)^2$  to be unitless.

*Appendix B*

SUPPLEMENTARY INFORMATION FOR HIGH CAPACITY  
V-BASED METAL HYDRIDE ELECTRODES FOR  
RECHARGEABLE BATTERIES

**B.1 Alloy and Electrode Characterization**

The microstructure of  $\text{Ti}_{29}\text{V}_{62-x}\text{Ni}_9\text{Cr}_x$  ( $x = 0, 6, \text{ and } 12$ ) alloys was characterized by X-ray diffraction (XRD), scanning electron microscopy (SEM) with backscattered electron imaging (BES), and energy dispersive x-ray spectroscopy (EDS). Alloy samples characterized by XRD were pulverized to a fine powder via the procedures outlined in the main text. For SEM and EDS, the samples were mounted in graphite and polished to a mirror finish.

Measuring the lattice parameter is challenging because of the broad, overlapping peaks from regions of the BCC phase with different chemical compositions. The lattice parameter,  $a$ , of the majority V-rich region clearly decreases with higher

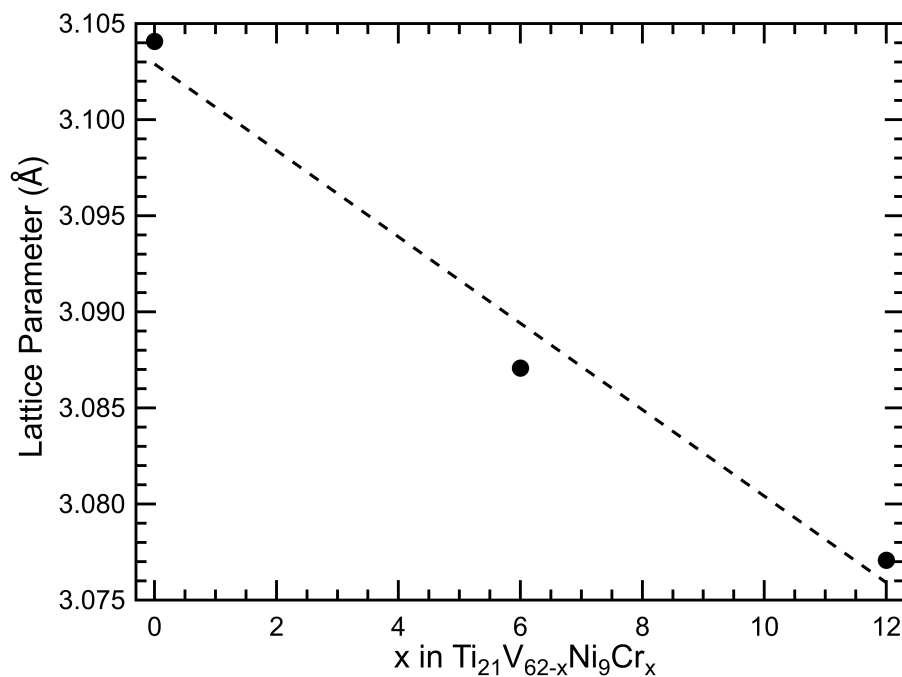


Figure B.1: Lattice parameters of dehydrated  $\text{Ti}_{29}\text{V}_{62-x}\text{Ni}_9\text{Cr}_x$  ( $x = 0, 6, \text{ and } 12$ ) alloys.

Cr content, however. From our analysis of the backscattered electron images, we estimate the fraction of the Ni-rich region to be about 9 vol%. The small amount of the Ni-rich region, the small number of reflections in the measured  $2\theta$  range, and the broad, overlapping peaks make analysis of the lattice parameter of this region difficult. Given that the second peak has nearly disappeared in the  $x = 12$  sample, we estimate that the lattice parameter of the Ni-rich region is slightly smaller, on the order of 0.3065 – 0.307 nm.

Electrochemical cells were assembled using electrodes containing  $\text{Ti}_{29}\text{V}_{62-x}\text{Ni}_9\text{Cr}_x$  ( $x = 0, 6,$  and  $12$ ) alloys. Three types of cells were used: (1) 3-electrode beaker cells assembled in air, (2) a 3-electrode Ar purged cell, and (3) coin cells assembled in air. In addition to electrochemical cycling, elemental analysis of the electrolyte was performed with inductively coupled plasma mass spectrometry (ICP-MS), and the surface oxidation states of the cycled electrodes were characterized by X-ray photoelectron spectroscopy (XPS).

Figure B.3 shows the discharge curves of  $\text{Ti}_{29}\text{V}_{62}\text{Ni}_9$  electrodes in pristine 1 M KOH, 6.9 M KOH, and 6.9 M KOH with 500 mM  $\text{KVO}_3$ . All three electrodes were assembled in air in three-electrode beaker cells. The Hg/HgO reference electrodes were prepared with the corresponding KOH solutions. The experiments were performed by discharging at a small current of 10 mA/g based on the loading of the alloy powder. These cells were discharged without prior charging, so the capacity is a result of metal oxidation rather than oxidation of absorbed hydrogen. According to the Pourbaix diagram, V oxidation to vanadate ions is expected at around -0.9 V vs. Hg/HgO (pH = 15) for a pure V electrode. The corresponding dissolution potential for the alloy is approximately -0.7 V in 6.9 M KOH solution, consistent with that reported in the main text (Figure 3.5a). Increasing the vanadate ion concentration in the electrolyte or reducing the pH both shift the dissolution potential to a more positive value, as predicted by the Pourbaix diagram. Slower kinetics may also contribute to the shift in dissolution potential, however.

Table B.1: ICP-MS analysis of KOH electrolytes in which  $\text{Ti}_{29}\text{V}_{62-x}\text{Ni}_9\text{Cr}_x$  ( $x = 0$  and  $12$ ) alloy electrodes were stored for 10 days.

| Alloy composition                                      | % Loss from electrode |      |      |      |
|--|-----------------------|------|------|------|
|  | Ti                    | V    | Ni   | Cr   |
| $\text{Ti}_{29}\text{V}_{62}\text{Ni}_9$               | 0.04                  | 6.77 | 0.11 | -    |
| $\text{Ti}_{29}\text{V}_{50}\text{Ni}_9\text{Cr}_{12}$ | 0.09                  | 2.47 | 0.07 | 0.15 |

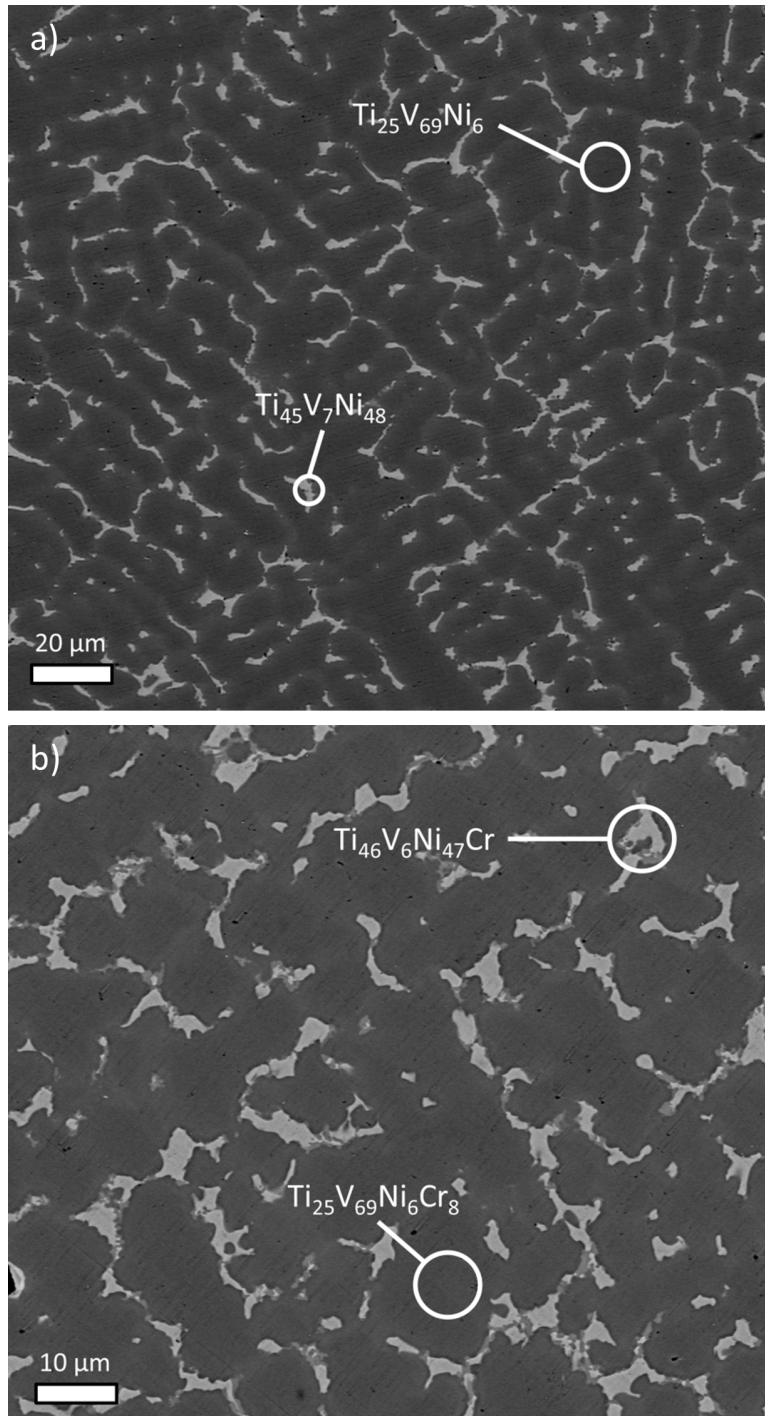


Figure B.2: Backscattered electron images of (a)  $\text{Ti}_{29}\text{V}_{62}\text{Ni}_9$  and (b)  $\text{Ti}_{29}\text{V}_{56}\text{Ni}_9\text{Cr}_6$  alloy ingots. Compositions superimposed on the image indicate average compositions of the V-rich (dark) and Ni-rich (light) regions as determined by EDS.

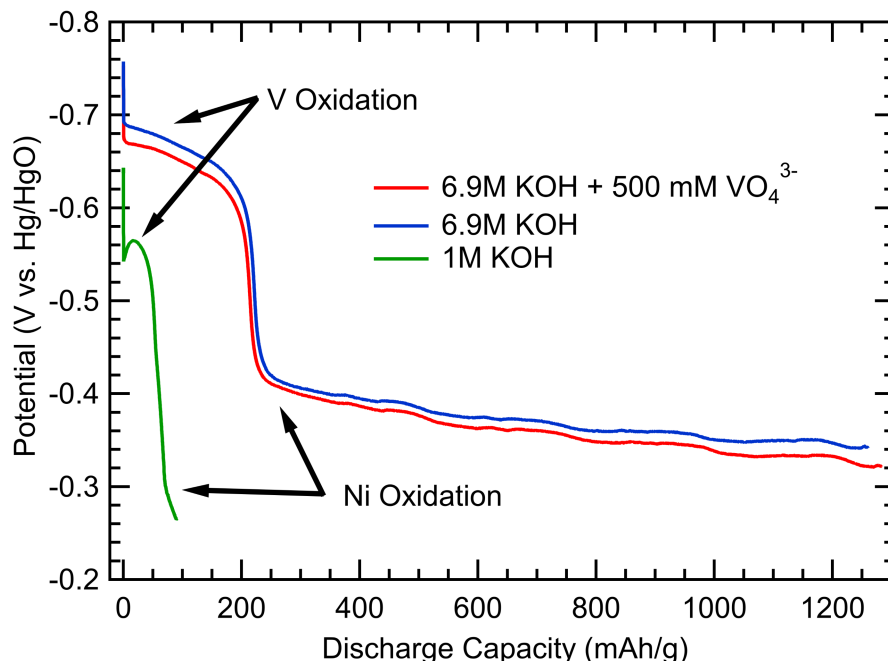


Figure B.3: Discharge curve of  $\text{Ti}_{29}\text{V}_{62}\text{Ni}_9$  electrode in various KOH electrolytes. Plateaus associated with V and Ni oxidation are indicated with arrows.

The XPS spectra for the  $\text{Ti}_{29}\text{V}_{62-x}\text{Ni}_9\text{Cr}_x$  ( $x = 0, 6, 12$ ) electrodes before cycling (spectra [1]) and after charging and discharging to  $-0.50$  V (spectra [4]) are presented in Figure B.4. The V  $2p_{3/2}$  metallic peaks disappear for the  $\text{Ti}_{29}\text{V}_{62}\text{Ni}_9$  and  $\text{Ti}_{29}\text{V}_{56}\text{Ni}_9\text{Cr}_6$  electrodes, and the oxide  $2p_{3/2}$  peaks shift to a higher binding energy. This shift corresponds to an increase in the oxidation state of the V. The surface oxide is likely a mixed oxide and manifests as a broad peak. There are no shifts in the Ti  $2p_{3/2}$  or  $2p_{1/2}$  peaks; the native oxide layer appears to be stable in the electrolyte environment. The XPS spectra for Ni show a disappearance of the metallic  $2p_{3/2}$  and  $2p_{1/2}$  peaks and emergence of the corresponding  $\text{Ni}(\text{OH})_2$  peaks. The  $\text{NiO}$   $2p_{3/2}$  and  $2p_{1/2}$  peaks persist during cycling. The broad Cr  $2p_{3/2}$  and  $2p_{1/2}$  peaks have a small shift to higher energy and an increase in amplitude, indicating that a  $\text{CrO}_x$  layer has formed on the surface. Similar to V, the  $\text{CrO}_x$  layer is likely a mixed oxide.

The design of the coin cells considered the following factors: (1) with a small internal volume, the cells can be sealed in air with a negligible amount of oxygen trapped inside the cells (2) the MH electrode is paired with a much larger  $\text{Ni}(\text{OH})_2$  positive electrode, so that the positive electrode does not evolve oxygen during cell overcharge and the potential remains relatively stable as a reference electrode. This

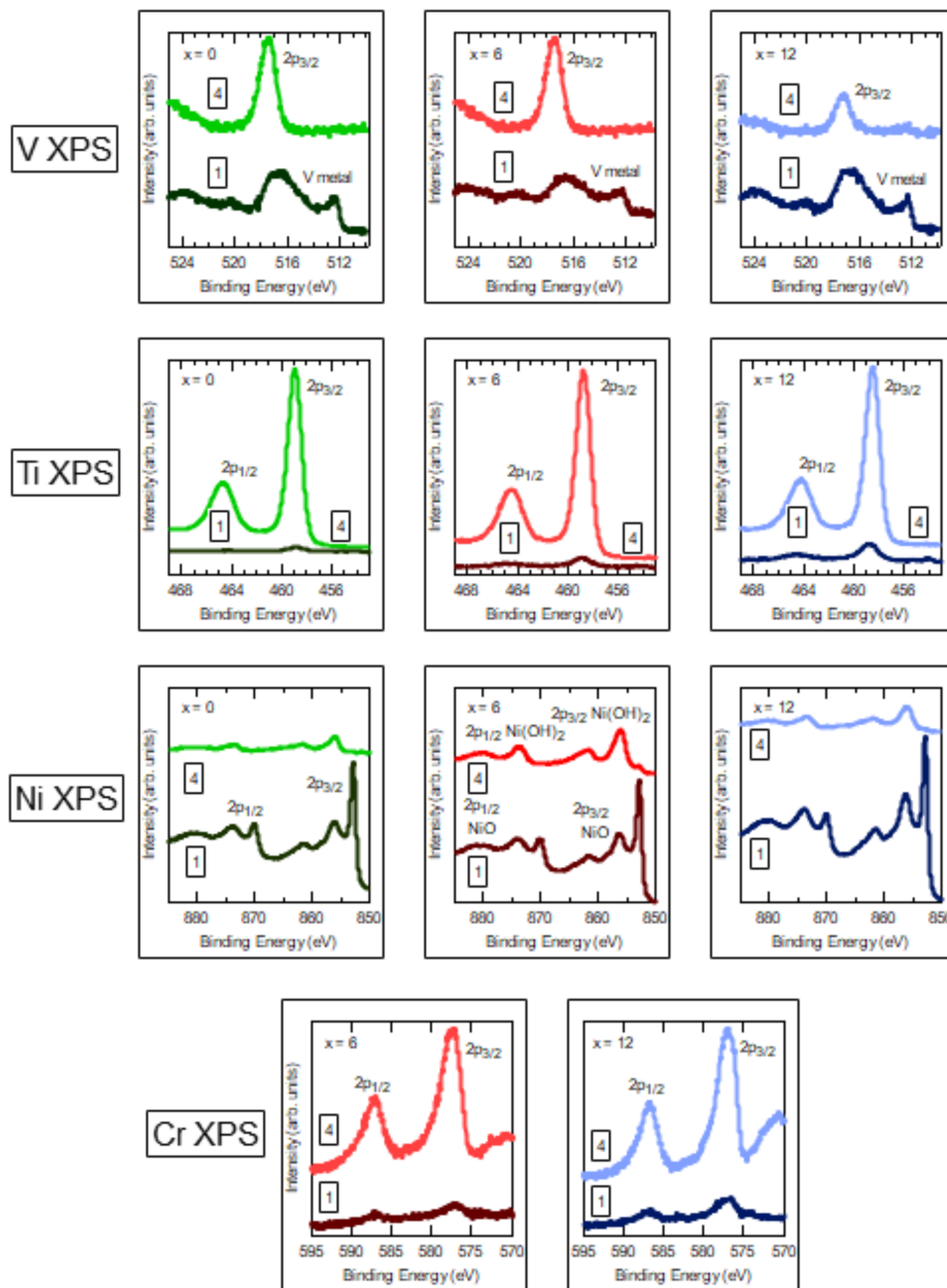


Figure B.4: XPS spectra of V, Cr, Ni, and Ti prior to charge [1] and after full discharge [4] of  $\text{Ti}_{29}\text{V}_{62-x}\text{Ni}_9\text{Cr}_x$  ( $x = 0, 6, \text{ and } 12$ ) alloy electrodes. Boxed numbers correspond to the state of charge indicated in 3.5a.

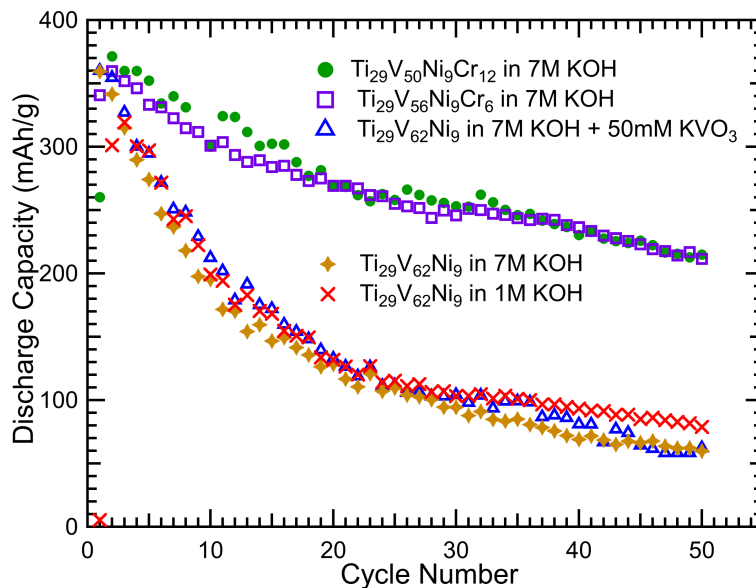


Figure B.5: Cycle performance of  $\text{Ti}_{29}\text{V}_{62-x}\text{Ni}_9\text{Cr}_x$  ( $x = 0, 6,$  and  $12$ ) alloy electrodes in various electrolytes. All tests were performed in air-saturated beaker cells. Cells were charged to  $800 \text{ mAh/g}$ , then discharged following the three-step discharge procedure up to  $-0.75\text{V}$  vs.  $\text{Hg/HgO}$ .

configuration is also more sensitive to capacity degradation of the MH electrode. Figure B.6 shows the operation potential of the  $\text{Ni}(\text{OH})_2/\text{NiOOH}$  electrode used in this study. These electrodes were obtained from BASF (BASF-Ovonic, Rochester Hills, MI, USA) and punched into disks with a  $1.27 \text{ cm}$  diameter. The capacity of each electrode is about  $24 \text{ mAh}$ . The results shown in Figure B.6 were obtained by first charging a  $\text{Ni}(\text{OH})_2$  electrode to  $12 \text{ mAh}$ , converting part of the  $\text{Ni}(\text{OH})_2$  to  $\text{NiO}(\text{OH})$ . The  $\text{Ni}(\text{OH})_2/\text{NiO}(\text{OH})$  electrode was then charged at the specific current density shown in Figure B.6 for  $7200 \text{ s}$ , rested for  $1200 \text{ s}$ , and discharged at the same current density for  $7200 \text{ s}$ . The charge ( $E_a$ ) and discharge ( $E_c$ ) plateau potentials were recorded and plotted in Figure B.6. The smallest current for the discharge of the coin cells was  $20 \text{ mA/g}$ , and the V dissolution potential for Cr-free alloy is at about  $-0.7 \text{ V}$  versus  $\text{Hg/HgO}$  (Figure B.3 and Figure 3.5). For these reasons, and to allow a voltage window as large as possible, the cut-off voltage for all coin cells was set at  $1.10 \text{ V}$ . All coin cells were assembled with the half-charged cathodes.

The  $\text{Ti}_{29}\text{V}_{50}\text{Ni}_9\text{Cr}_{12}$  electrodes in Figure 3.7 were charged for  $550 \text{ mAh/g}$ , which is higher than their maximum discharge capacity as measured in Figure 3.6. The Coulombic efficiency of these coin cells are also less than  $100\%$ . As a result, a small amount of hydrogen is evolved during charging, which may be consumed on

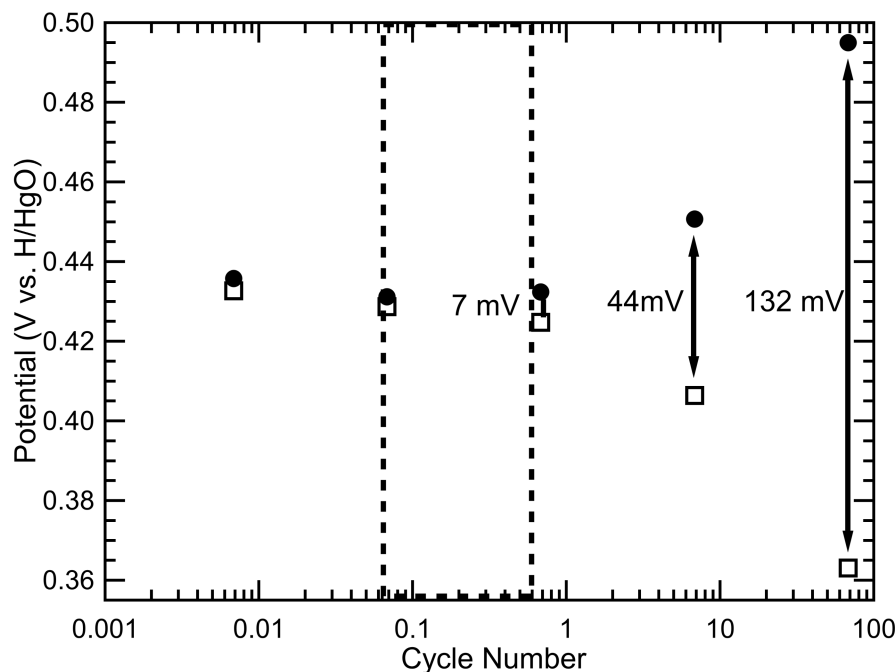


Figure B.6: Operation potential for the  $\text{Ni(OH)}_2/\text{NiO(OH)}$  electrode used in coin cells. Current density is based on the mass loading of the  $\text{Ni(OH)}_2$  electrode powder mixture. Closed and open symbols correspond to the plateau potentials for charge and discharge, respectively. The boxed region indicates the current density range associated with the MH electrode (10 to 100 mA/g for a  $3 \text{ mg/cm}^2$  loading).

the positive electrode by reducing  $\text{NiO(OH)}$  to  $\text{Ni(OH)}_2$ . [119]

## B.2 Energy density calculations of a MH-Air battery cell

Energy density calculations of the MH-air batteries are based on a prismatic cell design. This MH-air cell has three electrodes: oxygen-reduction-reaction (ORR) electrode, oxygen-evolution-reaction (OER) electrode, and an MH anode. The ORR electrode is a commercial alkaline fuel cell air electrode from Electric Fuel (Electric Fuel Limited, Bet Shemesh, Israel) with the catalytic  $\text{MnO}_2$  on a substrate film of PTFE. [120] The OER electrode is made from Monel mesh. The MH anode is made by pressing MH alloy powder onto a nickel mesh substrate. Figure B.8 shows the layout of the two-sided prismatic cell. The cell consists of two ORR-MH-OER stacks with the OER electrodes facing the interior of the cell. The OER electrodes are separated by a channel through which electrolyte flows. Flowing electrolyte is utilized to compensate for local changes in electrolyte concentration and pH due to water loss or generation as the cell charges or discharges.

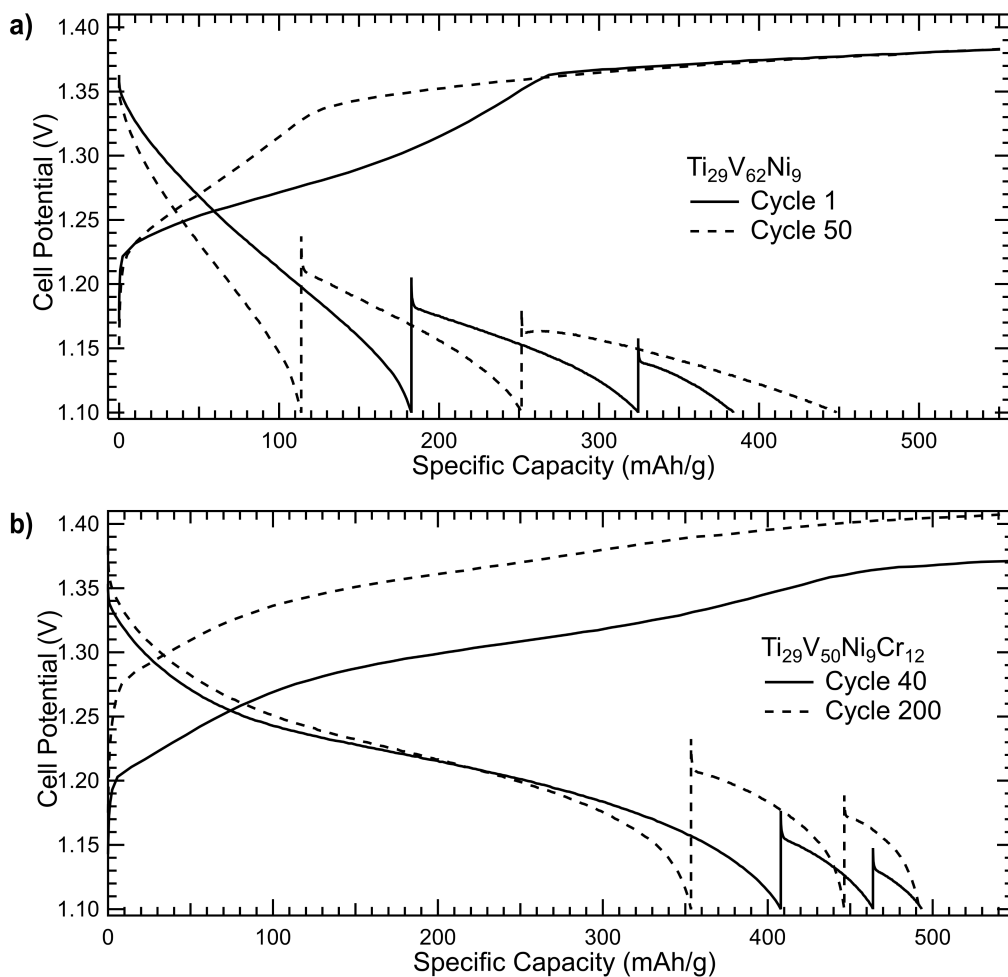


Figure B.7: Charge/discharge curves of a).  $\text{Ti}_{29}\text{V}_{62}\text{Ni}_9$  and b).  $\text{Ti}_{29}\text{V}_{50}\text{Ni}_9\text{Cr}_{12}$  electrodes in the coin cell configuration. The cells were charged for 550 mAh/g and three-step discharged at 100, 40, and 20 mA/g to 1.10V. The decrease of discharge capacity at the high current step shows that the rate capability of the MH electrode decreases with cycling, despite excellent capacity retention.

The cell was designed to achieve 100 Wh with an overall dimension of 20.2 cm x 10.2 cm x 1.13 cm. The cell discharge potential is determined from the ORR overpotential data as a function of cell current density, provided by the vendor of ORR electrode, and our cycling data for the MH anode. The air electrode potential is presented in Figure B.9. The current density needed from the ORR electrode is chosen to match the specifications of the MH anode for a given discharge rate. The total weight of the cell also includes those of passive components of electrode substrates, separators, frame, and seal materials. Key input parameters of this model are the MH anode thickness and MH anode specific discharge capacity. Other input parameters including dimension of the prismatic cell, dimensions of the two air electrodes, and the cell discharge C-rate, are preset based on project targets and some of the preliminary lab testing results.

Based on the preliminary experimental results of the cell similar to this design, the MH anode specific discharge capacity is in a range of 150 – 550 mAh/g, and the practical thickness of the anode is above 300 microns. The model varies the MH anode capacity from 0 – 800 mAh/g, and thickness from 0.3 – 5 mm. Varying these two parameters leads to a 2D contour plot of cell level gravimetric and volumetric energy density as shown in Figure 3.9. The colored lines are regions of constant energy density in Wh/kg or Wh/L. MH anodes containing  $\text{Ti}_{29}\text{V}_{62-x}\text{Ni}_9\text{Cr}_x$  ( $x = 0, 6, 12$ ) were demonstrated in Chapter 3 to have a specific capacity of more than 400 mAh/g, making it possible to achieve 200 Wh/kg. From the sensitivity analysis of Figure 3.9, there is also an optimized range of the MH anode thickness in this prismatic model, based on the targeted energy density. For example, with a target of 200 Wh/kg, the MH anode thickness is optimally 2 – 2.5 mm. The inputs and results from an individual calculation for the contour plots of Figure 3.9 are provided in Table B.2 below. The input values in the Example Case column are based on the specifications determined by Figure B.9 and our MH cycling data. For this example, an anode capacity of 400 mAh/g and thickness of 2.2 mm are chosen. The nominal cathode current is set to match the specifications of the MH anode with a discharge rate of C/3. The model then returns a specific energy density of 207 Wh/kg and a volumetric energy density of 427 Wh/L.



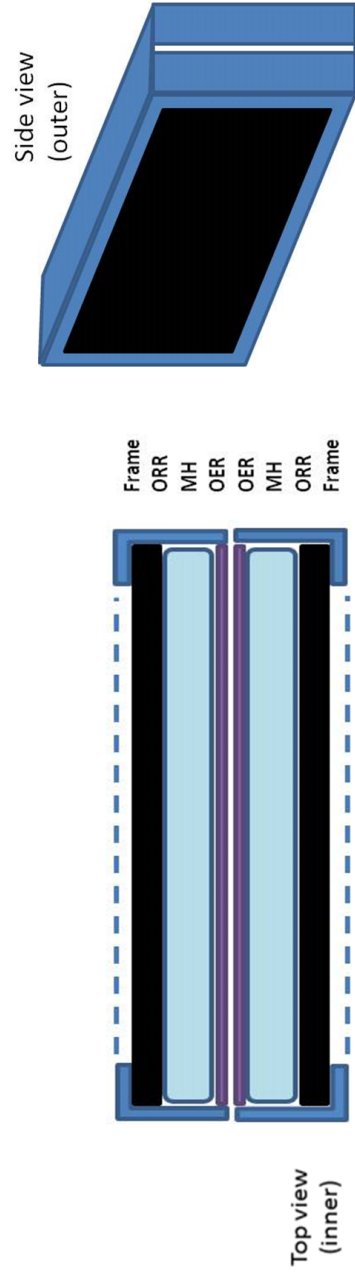


Figure B.8: Top view (left) and 3D side view (right) drawings of the 100-W Wh MH-air cell. Dimensions not to scale.

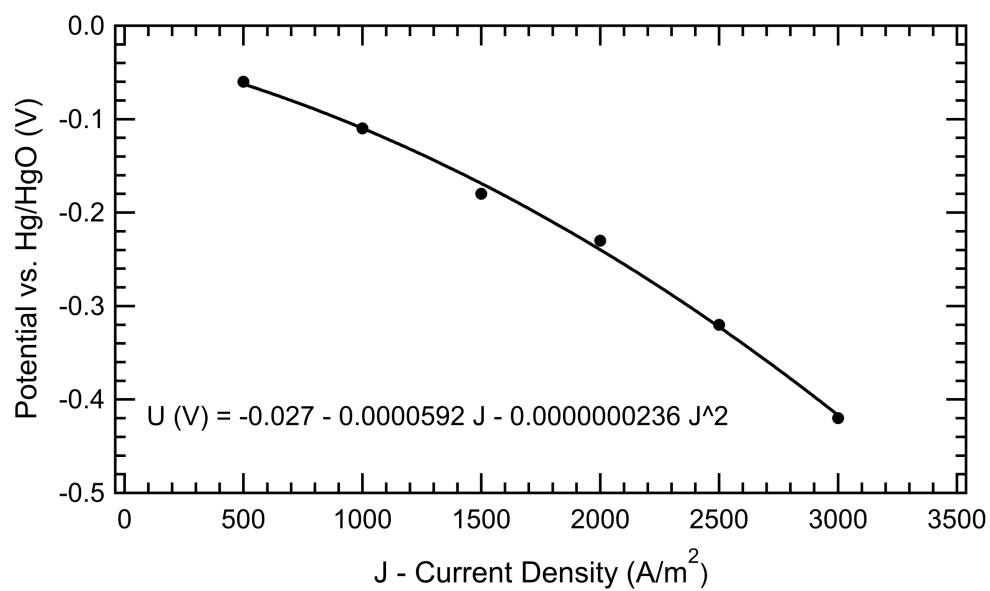


Figure B.9: Plot of electrode potential versus current density for the air electrode manufactured by Electric Fuel.[120]

*Appendix C*

## SHOULDER REMOVAL FROM X-RAY DIFFRACTION DATA

**C.1 Inel CPS120 Detector**

X-ray diffraction (XRD) patterns of the hydriding transition in palladium hydride (see Chapter 2) were acquired using an Inel Curved Position Sensitive (CPS) 120 powder diffractometer detector utilizing Mo  $K\alpha$  radiation. The use of a curved detector allows for the simultaneous collection of X-rays diffracted up to  $120^\circ 2\theta$ , enabling faster measurement times. The Inel CPS120 detector is based on the device reported by Ballon et al., which improved upon wire-based chamber detectors by replacing the anode wire with a metal blade.[121] This change allowed for these detectors to be curved; ideal for X-ray crystallography experiments.

The detector chamber consists of the knife-edge anode, a set of evenly spaced cathode readout strips, and a delay line. A pressurized mixture of argon and ethane flow through the detector. X-ray photons ionize the argon atoms, and the ejected electrons are accelerated by the electric field to the cathode. The cathode is connected to a delay line, which generates a pulse that is output to additional electronics. Each cathode strip is referred to as a channel, with 4096 channels total. The pulse is amplified, and the time delay is converted to position in order to determine the exact  $2\theta$  position of the pulse.

**Detector Calibration**

A flat Si  $\langle 110 \rangle$  single crystal oriented in the  $\langle 220 \rangle$  direction ( $\theta_{\text{Bragg}} = 10.644^\circ$ ) is used as a non-focusing incident beam monochromator. A set of Pb slits are used to select a beam profile of  $6.0 \times 0.5$  mm perpendicular to the beam direction. Diffuse background scattering was limited with the incorporation of a Pb slit 2.0 mm wide immediately following the monochromator crystal.

The CPS 120 detector rotates around a goniometer circle to operate in either transmission or reflection diffraction geometries. As a result, the channel number to  $2\theta$  relationship must be calibrated whenever the detector is moved. Additional alignment of the X-ray beam (by adjusting the tube tower) is required to ensure that the beam intersects the sample at the center of the goniometer circle. Sample stage alignment and two theta calibration of the detector was performed using a NIST

Standard Reference Material (SRM) 660a (LaB<sub>6</sub>) powder dispersed in Formvar on a glass slide. The diffractometer geometry is configured in a flat-plate asymmetric reflection geometry, which is subtly but distinctly different than traditional Bragg-Brentano geometries.[122, 123] In asymmetric reflection geometry, X-rays are incident on the sample with a fixed angle  $\omega$  from parallel. Peak shifts  $\delta$  due to displacements perpendicular to the sample stage are given by:

$$\delta = \frac{s_1 \sin 2\theta}{R_s \sin \omega} \frac{180}{\pi} \quad (\text{C.1})$$

with  $s_1$  the displacement distance and  $R_s$  the detector radius (250 mm in this case).

Alignment of the incident X-ray beam with the center of the goniometer circle was performed iteratively. First, the beam position is shifted by small translations of the X-ray tube tower. Then, diffraction patterns of the LaB<sub>6</sub> standard are acquired at high and low incidence angles  $\omega$ . If there is no shift in peak positions  $\delta$  between the two diffraction patterns, the stage and beam are considered to be aligned (according to Equation C.1) and the channel number to  $2\theta$  calibration can be performed. To do this, peaks are fit to the raw detector data to obtain the centroid of each diffraction peak in terms of channel number. These are matched to the expected  $2\theta$  diffraction angles of SRM 660a (LaB<sub>6</sub>), calculated from Bragg's Law:

$$n\lambda = 2d \sin \theta \quad (\text{C.2})$$

The lattice parameter of SRM 660a as reported by NIST is  $4.1569162 \pm 0.0000097 \text{ \AA}$  at  $22.5^\circ \text{ C}$ . The Mo  $K\alpha_1$  wavelength is  $0.7093 \text{ \AA}$ . Two theta values are plotted as a function of channel number, and a polynomial fit is used as the calibration formula.

## C.2 Anomalous Peak Shoulders

During  $2\theta$  calibration of the CPS120 detector, secondary peaks were observed to the right of each Bragg peak of the SRM. The secondary peaks were initially assumed to be due to  $K\alpha_2$  radiation. By Bragg's Law, the spacing between the two peaks should increase with  $2\theta$ , however, they are nearly constant as a function of channel number and therefore cannot be due to the  $K\alpha_2$  radiation. Figure C.1 plots the measured raw signal from NIST SRM 640b (Si) acquired with Mo- $K\alpha$  radiation. The tick marks below each peak indicate the expected position of the Bragg reflections for  $K\alpha_1$  (red) and  $K\alpha_2$  (blue) radiation.

It was expected that the shoulder may be caused by failing electronics as the equipment is nearly 30 years old. To confirm that secondary peaks are not due to stray

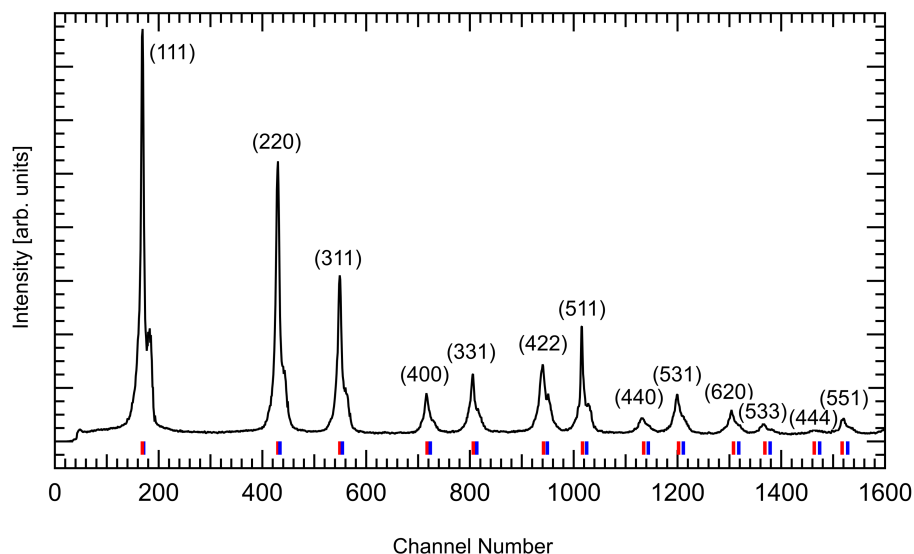


Figure C.1: Raw diffraction data from the NIST Standard Reference Material 640b (powdered Si) collected with the Inel CPS 120 Detector. Tick marks indicate expected peak positions from Mo  $K\alpha_1$  (red) and  $K\alpha_2$  x-ray wavelengths.

reflections in the XRD setup, the outputs from the detector to the processing electronics were flipped. This has the effect of flipping the diffraction pattern; lower index peaks will now be “seen” at higher channel numbers. If the shoulder is due to stray reflections, it should flip as well. Figure C.2 plots a flipped diffractogram of a Si standard. Reflections from the  $K\alpha_2$  are visible to the left of the  $K\alpha_1$  peaks as expected. The peak shoulder, however, remains to the right of the main peaks, confirming detector electronics are to blame for the shoulder.

Initially, shoulders were removed from raw  $\text{LaB}_6$  data using a machine learning algorithm.[124] The processed data was then fit to pseudo-Voigt functions using the Wavemetrics Igor Pro analysis software. Calculated  $\text{MoK}\alpha$   $2\theta$  angles of  $\text{LaB}_6$  were plotted against the channel number  $x$  of the corresponding peak centers, and a fourth-order polynomial was fit to the data:

$$2\theta = 4.6536 \pm 0.0504 + (0.031104 \pm 0.00019)x - ((3.97 \pm 2.07) * 10^{-7})x^2 + ((2.02 \pm 0.67) * 10^{-10})x^3 \quad (\text{C.3})$$

### C.3 Shoulder Removal with Deconvolution

#### Determination of Instrument Function

A detector instrument function was determined and incorporated into a deconvolution procedure to obtain corrected diffraction profiles. To measure the instrument

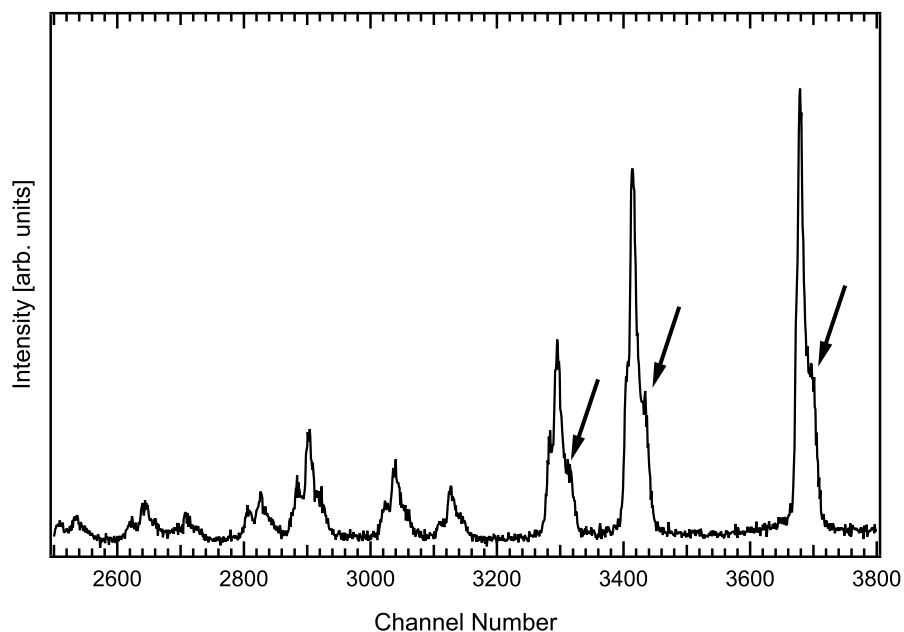


Figure C.2: Diffraction pattern of the NIST SRM 640b (Si) obtained on the Inel CPS 120 detector with output lines switched. The anomalous shoulder peaks are still observed to the right of the main peak, as indicated by the black arrows.

function, a sample of amorphous  $\text{GeO}_2$  was placed in the diffractometer sample holder to give a broad signal across the detector. The detector was covered entirely in Pb aside from a small slit which allowed for a very small (10) number of channels to be illuminated. The slit was placed at random intervals between channel numbers 200 and 2000 (corresponding to a  $2\theta$  range of  $10$  to  $64^\circ$ ) to characterize any changes in the shoulder as a function of channel number. An example of the signal obtained through the Pb slits is provided in Figure C.3. Also plotted is a peak from the Si standard (rescaled) to demonstrate that the width of the signal passing through the Pb slits is less than that of a Bragg reflection. Similar results were observed when compared to Bragg reflections from the  $\text{LaB}_6$  SRM. This consideration will make for a more accurate determination of the instrument function.

All diffractograms collected from the  $\text{GeO}_2$  and Pb slit setup were fit to two Lorentzian functions, one for the primary peak and one for the shoulder. These fits were obtained with the MATLAB code `lorentzfit`. Figures C.4, C.5, and C.6 plot peak separation, relative peak magnitude and shoulder peak half-width at half maximum (HWHM), respectively, as a function of channel number. The separation between primary and shoulder peaks is relatively constant with respect to channel number, whereas magnitude and HWHM increase with channel number

until leveling off past channel 1000.

A custom MATLAB code (`FitConvFunc`) was used to determine instrument functions by taking as inputs raw Pb slit/GeO<sub>2</sub> data and a Lorentzian fit to the primary peak (the true signal). On a plot of the raw data, the user is asked to select a peak corresponding to the true signal and at least one peak resulting from an instrument function. A new instrument function is created which consists of Gaussians centered at each selection. This instrument function is convolved with the true signal and fit to the raw data with a non-linear least squares fitting procedure, `lsqnonlin`. Each iteration refines the magnitude, center, and width of Gaussian peaks in the instrument function until the fit converges. A graphical example of the fitting procedure is provided in Figure C.7, which plots raw Pb slit/GeO<sub>2</sub> data, a Lorentzian fit of the primary peak, and the simulated measured signal generated by convolving the Lorentzian fit with the instrument function.

Individual instrument functions were evaluated for all 18 Pb slit/GeO<sub>2</sub> datasets; two are plotted in Figure C.8. Peak shoulders in raw data were accurately accounted for with only two Gaussians in the instrument function: a delta function at zero shift and a broad Gaussian some distance away. Characteristics of the second peak, including magnitude, width, and separation from the central delta function vary in a manner similar to the shoulder peak of the Pb slit/GeO<sub>2</sub> data.

### **Deconvolution of Raw Data**

Peak shoulders in raw X-ray diffractograms make Rietveld refinement of a multi-phase system difficult, as GSAS-II attributes peak shoulders to their own phase. Oftentimes the shoulders overlap with true peaks, and can distort lattice parameter, peak width, and phase fraction refinement. Instrument functions evaluated from the Pb slit/GeO<sub>2</sub> data were used to remove shoulders from raw XRD data using a convolution procedure similar to `FitConvFunc`. The deconvolution function, `FitConv`, takes as input the raw data file and an instrument function. A test function (initialized as a copy of the raw data) is generated, convolved with the instrument function, and subsequently fit to the raw data file. The range for deconvolution is fixed to be between channels 50 and 4000; a large range is necessary to accurately capture the background signal. The intensity at each channel number is set as a free parameter to be fit so there is no loss or artificial smoothing of the raw data. Each dataset requires several minutes to process as a result of this large number of fitting parameters.

To account for the variation in shoulder characteristics evident in Figures C.4, C.5, and C.6, different sections of raw diffraction data were deconvoluted with different instrument functions. These functions represent average values of the range of corresponding channel numbers. It was found later that peak-shoulder separation increased between the time of GeO<sub>2</sub> data collection and *in situ* PdH measurements, requiring manual adjustment of peak-shoulder separation values of the instrument functions. For example, the initial separation values of 30 channels had to be increased to 45 for better shoulder removal in the nanocrystalline Pd data.

Figure C.9 plots raw data, deconvoluted data, and the difference for a single bulk PdH scan. Obvious peak shoulders have been nearly eliminated (with the exception of noise), and primary peak shape is well preserved with only a minimal loss in intensity. Three separate instrument functions were used to fit channels 50 to 750, 751 to 1150, and 1151 to 1800. Differences between the three functions were primarily in shoulder magnitude and width rather than peak-shoulder separation.

Deconvolution of the nanocrystalline PdH data was ultimately performed using a single instrument function that represented average values for peak-shoulder separation and shoulder magnitude and width. No obvious differences existed for data processed with a single function when compared to data processed with the same three functions used to process bulk PdH data. A comparison of raw and deconvoluted data nanocrystalline PdH is provided in Figure C.10.

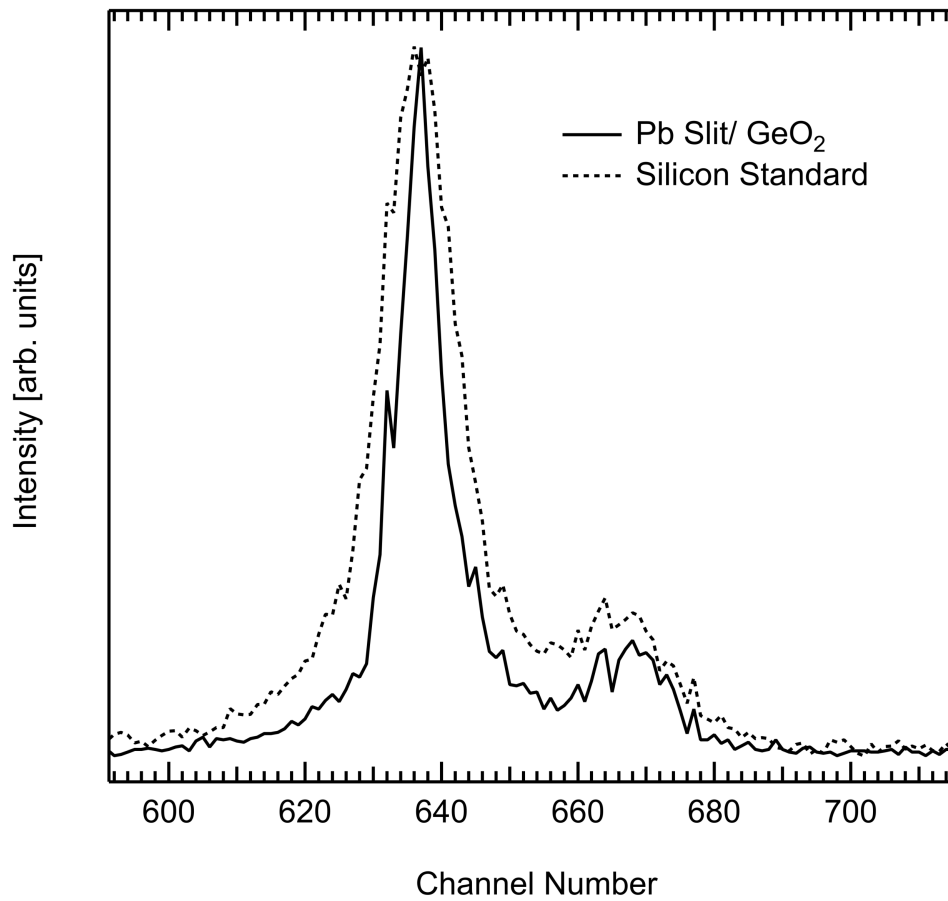


Figure C.3: Comparison of peak shape of signal obtained through Pb slits to Bragg reflection of a Si standard. The Si Bragg peak is approximately twice as wide as the signal passed through the Pb slits.

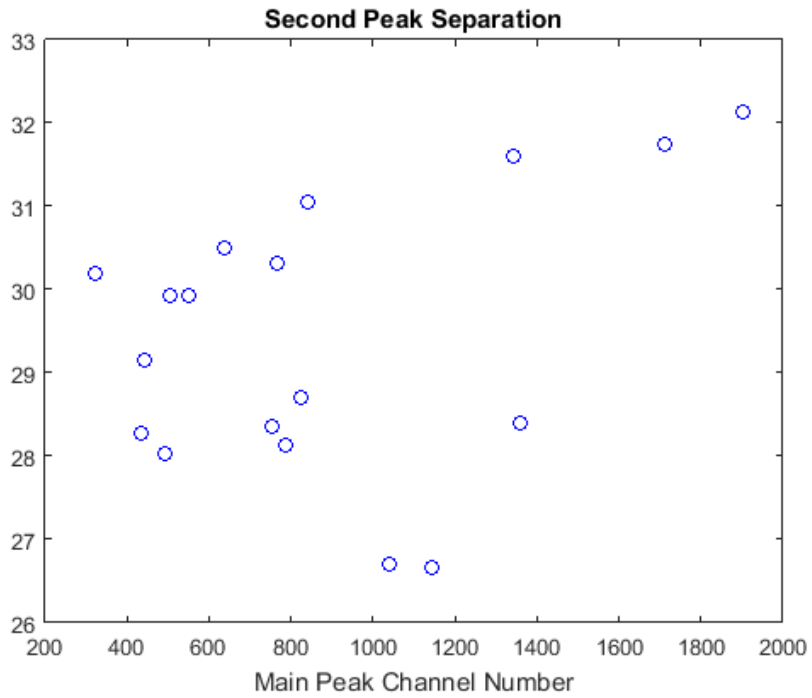


Figure C.4: Primary and shoulder peak separation (in channel numbers) as a function of channel number of the primary peak. Both peaks are fit with a separate Lorentzian function.

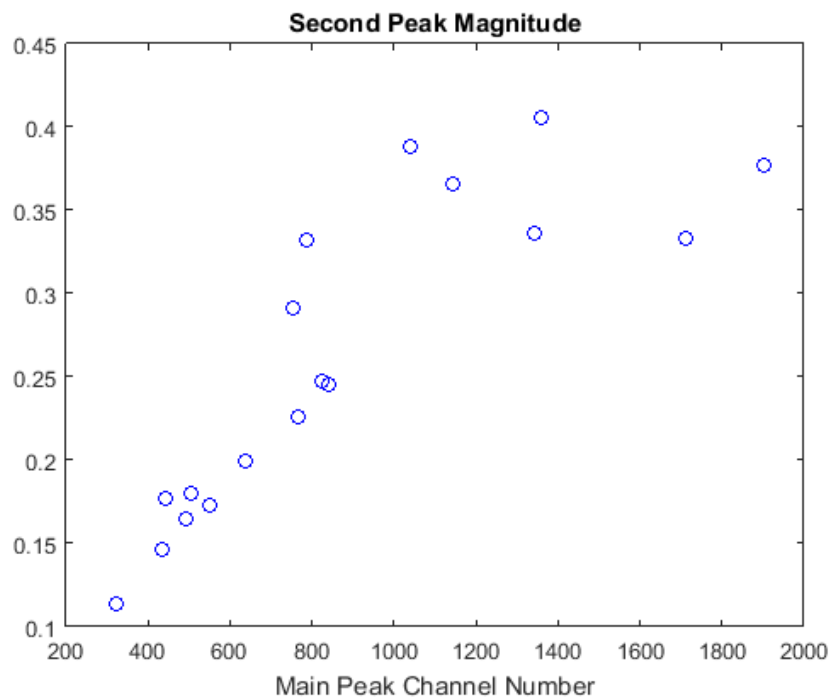


Figure C.5: Relative magnitude of the shoulder peak as a function of channel number.

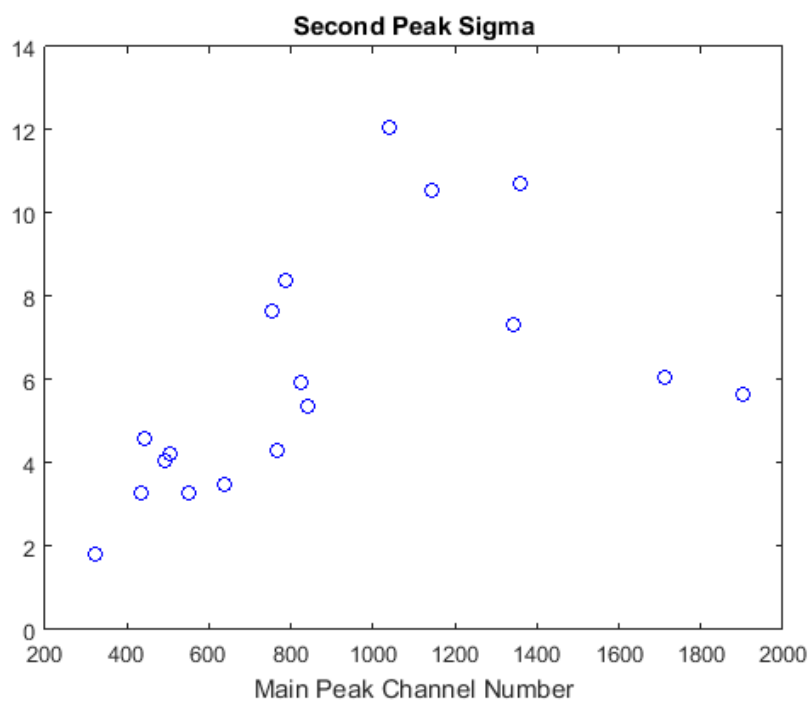


Figure C.6: Half-width at half maximum of the shoulder peaks as a function of channel number.

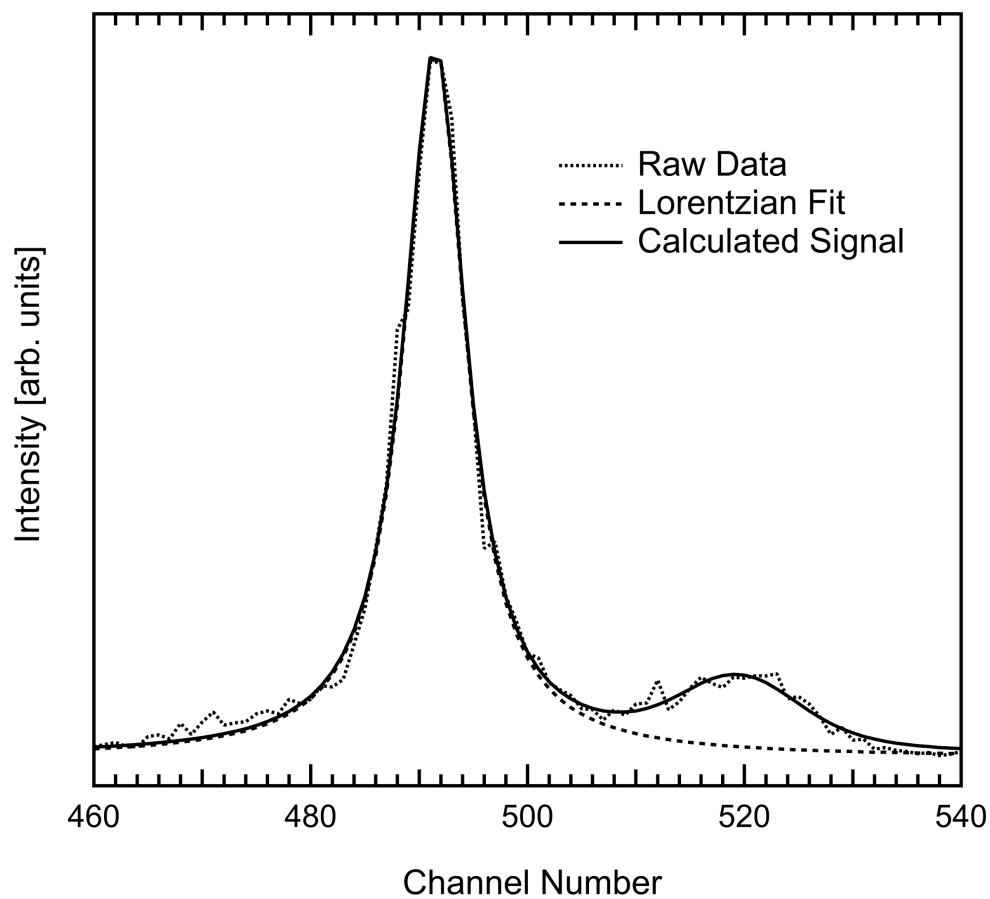


Figure C.7: Plot illustrating the instrument function determination. The dotted line is raw data obtained from the Pb slit/GeO<sub>2</sub> setup, the dashed line is a Lorentzian fit to the main peak, and the solid line plots the result of convolving the instrument function with the Lorentzian peak. Examples of the instrument function are provided in Figure C.8.

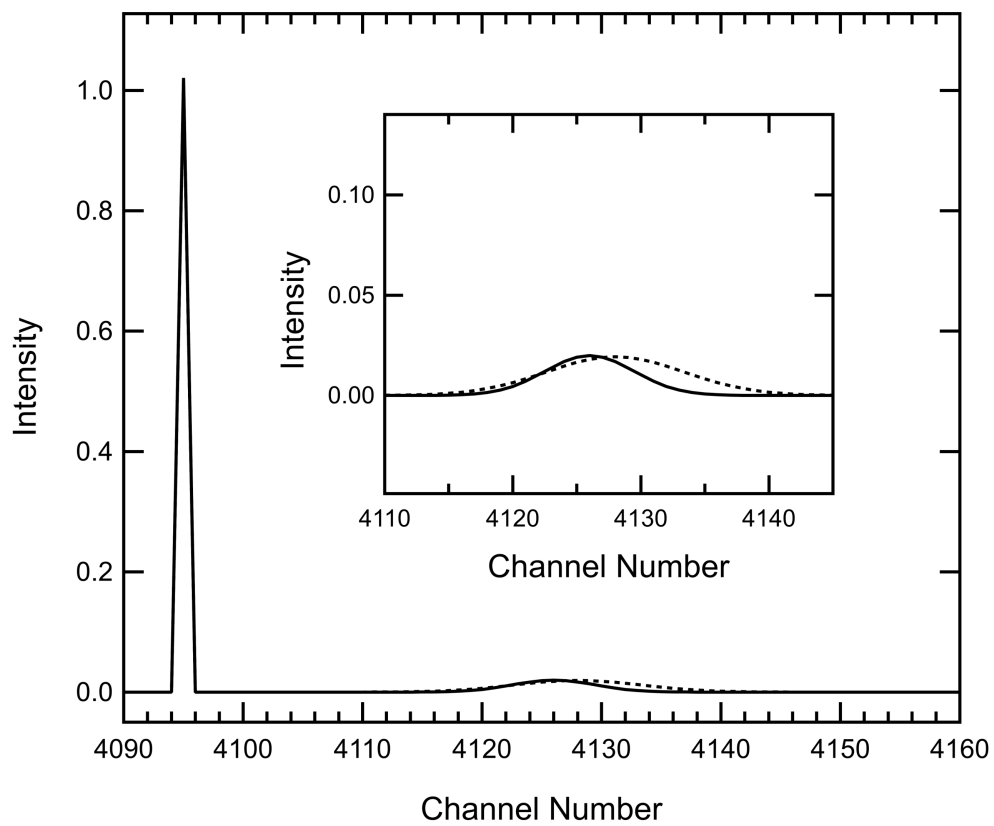


Figure C.8: Two (solid and dashed lines) of 18 instrument functions describing shoulder behavior of the Inel CPS120 detector. The functions consist of a delta function at 4096 and a small peak resulting in a shoulder in the raw diffraction data.

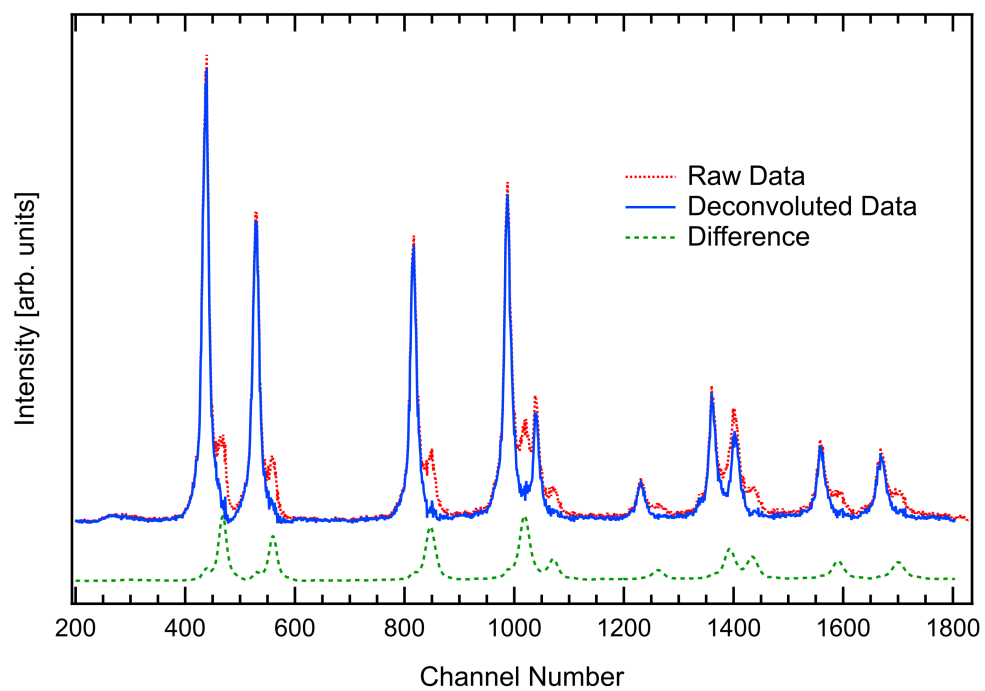


Figure C.9: Raw (dotted red line) and deconvoluted (solid blue line) bulk Pd diffraction patterns acquired with the CPS 120 detector. Primary peak shapes are well preserved.

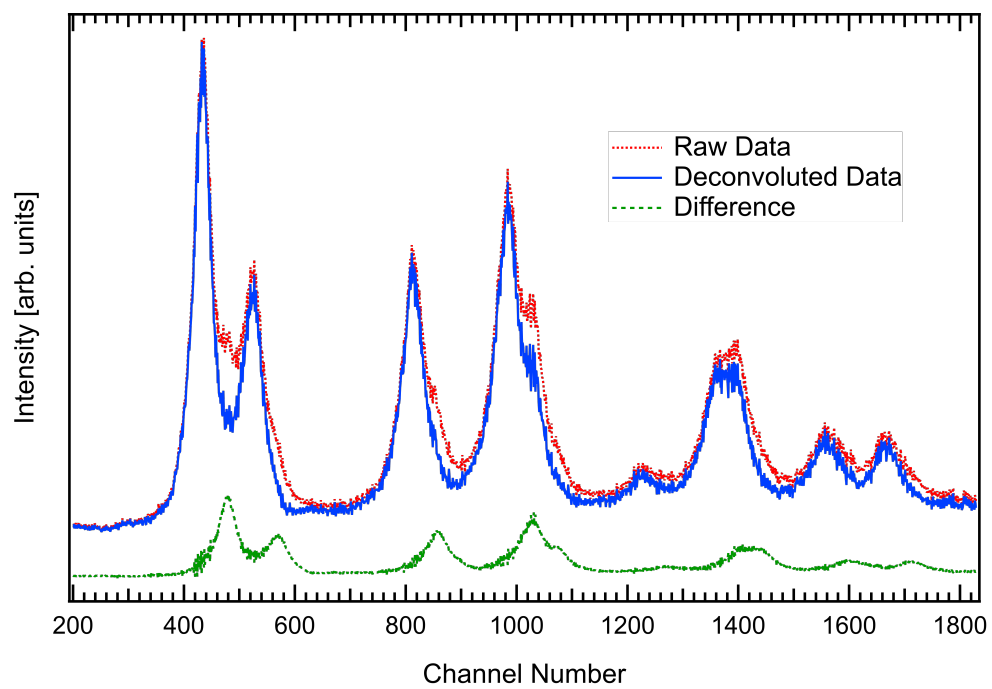


Figure C.10: Raw (dotted red line) and deconvoluted (solid blue line) nanocrystalline Pd diffraction patterns acquired with the CPS 120 detector. Primary peak shapes are well preserved.

## BIBLIOGRAPHY

- (1) Graham, T. *Proceedings of the Royal Society of London* **1868**, *16*, 422–427.
- (2) Farber, E. *Chymia* **1962**, *8*, 165–180.
- (3) Turner, J. A. *Science* **2004**, *305*, 972–974.
- (4) Dürr, S.; Müller, M.; Jorschick, H.; Helmin, M.; Bösmann, A.; Palkovits, R.; Wasserscheid, P. *ChemSusChem* **2017**, *10*, 42–47.
- (5) Coradia iLint - the world's 1st hydrogen powered train., Alstom, (accessed 10/12/2018).
- (6) Vetrano, J. B. *Nuclear Engineering and Design* **1971**, *14*, 390–412.
- (7) Kleperis, J.; Wójcik, G.; Czerwinski, A.; Skowronski, J.; Kopczyk, M.; Beltowska-Brzezinska, M. *Journal of Solid State Electrochemistry* **2001**, *5*, 229–249.
- (8) Bowman, R. C.; Fultz, B. *MRS Bulletin* **2002**, *27*, 688–693.
- (9) Huiberts, J. N.; Griessen, R.; Rector, J. H.; Wijngaarden, R. J.; Dekker, J. P.; de Groot, D. G.; Koeman, N. J. *Nature* **1996**, *380*, 231–234.
- (10) Rönnebro, E. C. E.; Majzoub, E. H. *MRS Bulletin* **2013**, *38*, 452–458.
- (11) Lototsky, M. V.; Yartys, V. A.; Pollet, B. G.; Bowman Jr., R. C. *International Journal of Hydrogen Energy* **2014**, *39*, 5818–5851.
- (12) Mohtadi, R.; Orimo, S.-i. *Nature Reviews Materials* **2017**, *2*, 16091.
- (13) Syed, H. M.; Webb, C. J.; Gray, E. M. *Progress in Solid State Chemistry* **2016**, *44*, 20–34.
- (14) Liu, H.; Naumov, I. I.; Geballe, Z. M.; Somayazulu, M.; Tse, J. S.; Hemley, R. J. *Physical Review B* **2018**, *98*, 100102.
- (15) Somayazulu, M.; Ahart, M.; Mishra, A. K.; Geballe, Z. M.; Baldini, M.; Meng, Y.; Struzhkin, V. V.; Hemley, R. J. *arXiv:1808.07695 [cond-mat]* **2018**.
- (16) Sandrock, G. *Journal of Alloys and Compounds* **1999**, *293–295*, 877–888.
- (17) *Hydrogen in Metals I: Basic Properties*; Alefeld, G., Völkl, J., Eds.; Topics in Applied Physics; Springer-Verlag: Berlin Heidelberg, 1978.
- (18) Yukawa, H.; Yamashita, D.; Ito, S.; Morinaga, M.; Yamaguchi, S. *Materials Transactions* **2002**, *43*, 2757–2762.
- (19) Reilly, J. J.; Wiswall, R. H. *Inorganic Chemistry* **1970**, *9*, 1678–1682.
- (20) Lacher, J. R. *Proc. R. Soc. Lond. A* **1937**, *161*, 525–545.

- (21) Frieske, H.; Wicke, E. *Berichte der Bunsengesellschaft für physikalische Chemie* **1973**, *77*, 48–52.
- (22) Lässer, R.; Klatt, K.-H. *Physical Review B* **1983**, *28*, 748–758.
- (23) Gillespie, L. J.; Galstaun, L. S. *Journal of the American Chemical Society* **1936**, *58*, 2565–2573.
- (24) Griessen, R.; Strohfeltdt, N.; Giessen, H. *Nature Materials* **2016**, *15*, 311–317.
- (25) Ulvestad, A.; Welland, M. J.; Cha, W.; Liu, Y.; Kim, J. W.; Harder, R.; Maxey, E.; Clark, J. N.; Highland, M. J.; You, H.; Zapol, P.; Hruszkewycz, S. O.; Stephenson, G. B. *Nature Materials* **2017**, *16*, 565–571.
- (26) Everett, D. H.; Nordon, P. *Proc. R. Soc. Lond. A* **1960**, *259*, 341–360.
- (27) Lynch, J. F.; Clewley, J. D.; Curran, T.; Flanagan, T. B. *Journal of the Less Common Metals* **1977**, *55*, 153–163.
- (28) Flanagan, T. B.; Lynch, J. F.; Clewley, J. D.; von Turkovich, B. *Scripta Metallurgica* **1975**, *9*, 1063–1068.
- (29) Flanagan, T. B.; Clewley, J. D. *Journal of the Less Common Metals* **1982**, *83*, 127–141.
- (30) Wicke, E.; Blaurock, J. *Journal of the Less Common Metals* **1987**, *130*, 351–363.
- (31) Schwarz, R. B.; Khachaturyan, A. G. *Physical Review Letters* **1995**, *74*, 2523–2526.
- (32) Schwarz, R. B.; Khachaturyan, A. G. *Acta Materialia* **2006**, *54*, 313–323.
- (33) Bitter, F. *Physical Review* **1931**, *37*, 1527–1547.
- (34) Nabarro Frank Reginald Nunes; Mott Nevill Francis *Proceedings of the Royal Society of London. Series A. Mathematical and Physical Sciences* **1940**, *175*, 519–538.
- (35) Cahn, J. W.; Larché, F. *Acta Metallurgica* **1984**, *32*, 1915–1923.
- (36) Qian, S.; Northwood, D. O. *International Journal of Hydrogen Energy* **1990**, *15*, 649–654.
- (37) Narayan, T. C.; Hayee, F.; Baldi, A.; Koh, A. L.; Sinclair, R.; Dionne, J. A. *Nature Communications* **2017**, *8*, 14020.
- (38) Pundt, A.; Sachs, C.; Winter, M.; Reetz, M. T.; Fritsch, D.; Kirchheim, R. *Journal of Alloys and Compounds* **1999**, *293*, 480–483.
- (39) Sachs, C.; Pundt, A.; Kirchheim, R.; Winter, M.; Reetz, M. T.; Fritsch, D. *Physical Review B* **2001**, *64*, 075408.

- (40) Qian, S.; Northwood, D. O. *International Journal of Hydrogen Energy* **1988**, *13*, 25–35.
- (41) Wang, D.; Flanagan, T. B.; Kuji, T. *Physical Chemistry Chemical Physics* **2002**, *4*, 4244–4254.
- (42) Balasubramanian, B.; Barbir, F.; Neutzler, J. In *Proceedings of the 218th ACS National Meeting*, New Orleans, LA, USA, 1999; Vol. 44, pp 977–981.
- (43) Luo, S.; Luo, W.; Clewley, J. D.; Flanagan, T. B.; Wade, L. A. *Journal of Alloys and Compounds* **1995**, *231*, 467–472.
- (44) Witham, C. K. The effects of alloy chemistry on the electrochemical and hydriding properties of Ni-substituted LaNi<sub>5</sub>, Ph.D. California Institute of Technology, 1999.
- (45) Sakamoto, Y.; Yuwasa, K.; Hirayama, K. *Journal of the Less Common Metals* **1982**, *88*, 115–124.
- (46) Inoue, H.; Koyama, S.; Higuchi, E. *Electrochimica Acta* **2012**, *59*, 23–31.
- (47) Iwakura, C.; Choi, W.-K.; Miyauchi, R.; Inoue, H. *Journal of The Electrochemical Society* **2000**, *147*, 2503–2506.
- (48) Young, K.-h.; Nei, J. *Materials* **2013**, *6*, 4574–4608.
- (49) Van Vucht, J. H. N.; Kuijpers, F. A.; Bruning, H. C. A. M. *Philips Res. Rept.* **1970**, *25*, 133–140.
- (50) Sakai, T.; Yoshinaga, H.; Miyamura, H.; Kuriyama, N.; Ishikawa, H. *Journal of Alloys and Compounds* **1992**, *180*, 37–54.
- (51) Sakai, T.; Miyamura, H.; Kuriyama, N.; Uehara, I.; Muta, M.; Takagi, A.; Kajiyama, U.; Kinoshita, K.; Isogai, F. *Journal of Alloys and Compounds* **1993**, *192*, 158–160.
- (52) Tsukahara, M.; Takahashi, K.; Mishima, T.; Sakai, T.; Miyamura, H.; Kuriyama, N.; Uehara, I. *Journal of Alloys and Compounds* **1995**, *224*, 162–167.
- (53) Tsukahara, M.; Takahashi, K.; Mishima, T.; Sakai, T.; Miyamura, H.; Kuriyama, N.; Uehara, I. *Journal of Alloys and Compounds* **1995**, *226*, 203–207.
- (54) Tsukahara, M.; Takahashi, K.; Mishima, T.; Miyamura, H.; Sakai, T.; Kuriyama, N.; Uehara, I. *Journal of Alloys and Compounds* **1995**, *231*, 616–620.
- (55) Inoue, H.; Arai, S.; Iwakura, C. *Electrochimica Acta* **1996**, *41*, 937–939.
- (56) Maeland, A. J.; Gibb, T. R. P.; Schumacher, D. P. *Journal of the American Chemical Society* **1961**, *83*, 3728–3729.
- (57) Ono, S.; Nomura, K.; Ikeda, Y. *Journal of the Less Common Metals* **1980**, *72*, 159–165.
- (58) Hagi, T.; Sato, Y.; Yasuda, M.; Tanaka, K. *Transactions of the Japan Institute of Metals* **1987**, *28*, 198–204.

- (59) Libowitz, G.; Maeland, A. *Materials Science Forum* **1988**, *31*, 177–196.
- (60) Kagawa, A.; Ono, E.; Kusakabe, T.; Sakamoto, Y. *Journal of the Less Common Metals* **1991**, *172*, 64–70.
- (61) Tsukahara, M.; Takahashi, K.; Mishima, T.; Isomura, A.; Sakai, T. *Journal of Alloys and Compounds* **1996**, *243*, 133–138.
- (62) Tsukahara, M.; Takahashi, K.; Isomura, A.; Sakai, T. *Journal of Alloys and Compounds* **1999**, *287*, 215–220.
- (63) Guo, R.; Chen, L.-X.; Lei, Y.-Q.; Liao, B.; Ying, T.; Wang, Q.-D. *International Journal of Hydrogen Energy* **2003**, *28*, 803–808.
- (64) Inoue, H.; Miyauchi, R.; Shin-ya, R.; Choi, W.-K.; Iwakura, C. *Journal of Alloys and Compounds* **2002**, *330*, 597–600.
- (65) Sun, L.; Lin, J.; Cao, Z.; Liang, F.; Wang, L. *Journal of Alloys and Compounds* **2015**, *650*, 15–21.
- (66) Burch, R.; Mason, N. B. *Journal of the Chemical Society, Faraday Transactions 1: Physical Chemistry in Condensed Phases* **1979**, *75*, 561–577.
- (67) Inoue, H.; Kotani, N.; Chiku, M.; Higuchi, E. *Journal of Alloys and Compounds* **2015**, *645*, S136–S139.
- (68) King, H. W.; Manchester, F. D. *Journal of Physics F: Metal Physics* **1978**, *8*, 15.
- (69) Eastman, J. A.; Thompson, L. J.; Kestel, B. J. *Physical Review B* **1993**, *48*, 84–92.
- (70) Suleiman, M.; Jisrawi, N. M.; Dankert, O.; Reetz, M. T.; Bähz, C.; Kirchheim, R.; Pundt, A. *Journal of Alloys and Compounds* **2003**, *356-357*, 644–648.
- (71) Ingham, B.; Toney, M. F.; Hendy, S. C.; Cox, T.; Fong, D. D.; Eastman, J. A.; Fuoss, P. H.; Stevens, K. J.; Lassesson, A.; Brown, S. A.; Ryan, M. P. *Physical Review B* **2008**, *78*, 245408.
- (72) Narehood, D. G.; Kishore, S.; Goto, H.; Adair, J. H.; Nelson, J. A.; Gutiérrez, H. R.; Eklund, P. C. *International Journal of Hydrogen Energy* **2009**, *34*, 952–960.
- (73) Yamauchi, M.; Ikeda, R.; Kitagawa, H.; Takata, M. *The Journal of Physical Chemistry C* **2008**, *112*, 3294–3299.
- (74) Bardhan, R.; Hedges, L. O.; Pint, C. L.; Javey, A.; Whitelam, S.; Urban, J. J. *Nature Materials* **2013**, *12*, 905–912.
- (75) Syrenova, S.; Wadell, C.; Nugroho, F. A. A.; Gschneidner, T. A.; Diaz Fernandez, Y. A.; Nalin, G.; Świtlik, D.; Westerlund, F.; Antosiewicz, T. J.; Zhdanov, V. P.; Moth-Poulsen, K.; Langhammer, C. *Nature Materials* **2015**, *14*, 1236–1244.

- (76) Hayee, F.; Narayan, T. C.; Nadkarni, N.; Baldi, A.; Koh, A. L.; Bazant, M. Z.; Sinclair, R.; Dionne, J. A. *Nature Communications* **2018**, *9*, 1775.
- (77) Vogel, W.; He, W.; Huang, Q.-H.; Zou, Z.; Zhang, X.-G.; Yang, H. *International Journal of Hydrogen Energy* **2010**, *35*, 8609–8620.
- (78) Baldi, A.; Narayan, T. C.; Koh, A. L.; Dionne, J. A. *Nature Materials* **2014**, *13*, 1143–1148.
- (79) Lemmon, E. W.; Bell, I.; Huber, M. L.; McLinden, M. O. NIST Standard Reference Database 23: Reference Fluid Thermodynamic and Transport Properties-REFPROP, Version 10.0, National Institute of Standards and Technology., 2018.
- (80) Leachman, J. W.; Jacobsen, R. T.; Penoncello, S. G.; Lemmon, E. W. *Journal of Physical and Chemical Reference Data* **2009**, *38*, 721–748.
- (81) Toby, B. H.; Von Dreele, R. B. *Journal of Applied Crystallography* **2013**, *46*, 544–549.
- (82) Mütschele, T.; Kirchheim, R. *Scripta Metallurgica* **1987**, *21*, 1101–1104.
- (83) In *Smithells Metals Reference Book (Seventh Edition)*, Brandes, E. A., Brook, G. B., Eds.; Butterworth-Heinemann: Oxford, 1992, pp 15–1.
- (84) Weller, M.; Diehl, J.; Schaefer, H. E. *Philosophical Magazine A* **1991**, *63*, 527–533.
- (85) Nabarro, F. R. N. *Proceedings of the Physical Society* **1940**, *52*, 90.
- (86) Ho, E.; Goldberg, H. A.; Weatherly, G. C.; Manchester, F. D. *Acta Metallurgica* **1979**, *27*, 841–853.
- (87) Bever, M. B.; Holt, D. L.; Titchener, A. L. *Progress in Materials Science* **1973**, *17*, 5–177.
- (88) Zou, W.-N.; He, Q.-C.; Zheng, Q.-S. *International Journal of Solids and Structures* **2012**, *49*, 1627–1636.
- (89) Lee, Y.-G.; Zou, W.-N.; Ren, H.-H. *International Journal of Solids and Structures* **2016**, *81*, 399–410.
- (90) Cahn, J. W. *Acta Metallurgica* **1962**, *10*, 907–913.
- (91) Hsu, D. K.; Leisure, R. G. *Physical Review B* **1979**, *20*, 1339–1344.
- (92) Pourbaix, M., *Atlas of electrochemical equilibria in aqueous solutions*; National Association of Corrosion Engineers: 1974.
- (93) Beverskog, B.; Puigdomenech, I. *Corrosion Science* **1997**, *39*, 43–57.
- (94) Beverskog, B.; Puigdomenech, I. *Corrosion Science* **1997**, *39*, 969–980.
- (95) Wilhelmsen, W.; Hurlen, T. *Electrochimica Acta* **1987**, *32*, 85–89.

- (96) Schrebler Guzmán, R. S.; Vilche, J. R.; Arvía, A. J. *Corrosion Science* **1978**, *18*, 765–778.
- (97) Wang, L.; Zhang, J.; Gao, Y.; Xue, Q.; Hu, L.; Xu, T. *Scripta Materialia* **2006**, *55*, 657–660.
- (98) Mentus, S.; Pjescic, J.; Blagojevic, N. *Materials and Corrosion* **2002**, *53*, 44–50.
- (99) Kim, J.-H.; Lee, H.; Lee, P. S.; Seo, C.-Y.; Lee, J.-Y. *Journal of Alloys and Compounds* **2003**, *348*, 293–300.
- (100) Post, K.; Robins, R. G. *Electrochimica Acta* **1976**, *21*, 401–405.
- (101) Inzelt, G.; Lewenstam, A.; Scholz, F., *Handbook of Reference Electrodes*; Springer: Dordrecht, 2013.
- (102) Hepler, L. G.; Hill, J. O.; Worsley, I. G. *Chemical Reviews* **1971**, *71*, 127–137.
- (103) Liu, B.; Zheng, S.; Wang, S.; Zhang, Y.; Ortega, A.; Kim, N. S.; Han, K.; Du, H. *Electrochimica Acta* **2012**, *76*, 262–269.
- (104) Al-Kharafi, F. M.; Badawy, W. A. *Electrochimica Acta* **1997**, *42*, 579–586.
- (105) Yang, H.; Chen, Y.; Tao, M.; Wu, C.; Shao, J.; Deng, G. *Electrochimica Acta* **2010**, *55*, 648–655.
- (106) Liu, Y.; Pan, H.; Gao, M.; Li, R.; Wang, Q. *The Journal of Physical Chemistry C* **2008**, *112*, 16682–16690.
- (107) Yu, X. B.; Wu, Z.; Xia, B. J.; Xu, N. X. *The Journal of Chemical Physics* **2004**, *121*, 987–990.
- (108) Evans, H. T. *Zeitschrift für Kristallographie - Crystalline Materials* **1960**, *114*, 257–277.
- (109) McCafferty, E., *Introduction to Corrosion Science*; Springer New York: New York, 2010.
- (110) Reddy, T. B.; Linden, D., *Linden's handbook of batteries*, 4th; McGraw-Hill: New York, 2011.
- (111) Noonan, K. J. T.; Hugar, K. M.; Kostalik, H. A.; Lobkovsky, E. B.; Abruña, H. D.; Coates, G. W. *Journal of the American Chemical Society* **2012**, *134*, 18161–18164.
- (112) Choi, J. W.; Aurbach, D. *Nature Reviews Materials* **2016**, *1*, 16013.
- (113) Howard, W. F.; Spotnitz, R. M. *Journal of Power Sources* **2007**, *165*, 887–891.
- (114) Manchester, F., *Phase diagrams of binary hydrogen alloys*; Monograph series on alloy phase diagrams; ASM International: 2000.

- (115) Zabel, H.; Peisl, H. *Acta Metallurgica* **1980**, *28*, 589–599.
- (116) Zabel, H.; Peisl, J. *Journal of Physics F: Metal Physics* **1979**, *9*, 1461.
- (117) Dou, T.; Wu, Z.; Mao, J.; Xu, N. *Materials Science and Engineering: A* **2008**, *476*, 34–38.
- (118) Yu, X. B.; Yang, Z. X.; Feng, S. L.; Wu, Z.; Xu, N. X. *International Journal of Hydrogen Energy* **2006**, *31*, 1176–1181.
- (119) Purushothaman, B. K.; Wainright, J. S. *Journal of Power Sources* **2012**, *206*, 421–428.
- (120) Electric Fuel Air Electrodes., <http://electric-fuel.com/rd/zinc-air/air-electrode/>.
- (121) Ballon, J.; Comparat, V.; Pouxé, J. *Nuclear Instruments and Methods in Physics Research* **1983**, *217*, 213–216.
- (122) Rowles, M. R.; Madsen, I. C. *Journal of Applied Crystallography* **2010**, *43*, 632–634.
- (123) Rowles, M. R.; Buckley, C. E. *Journal of Applied Crystallography* **2017**, *50*, 240–251.
- (124) Moorthy, A. Theoretical and Experimental Study of Pressure Hysteresis in the Palladium Hydride Phase Transformation., Senior Thesis, California Institute of Technology, 2018.